Georg-August-Universität Göttingen

Faculty of Physics

Max Planck Institute for Dynamics and Self-Organization

Master thesis

Cell-Substrate Adhesion and Contact Guidance of *Dictyostelium discoideum* on Surfaces of Varying Curvatures

---

Marcel Schröder

June 22, 2018

First referee: Dr. Marco Tarantola
Second referee: Prof. Dr. Stefan Klumpp

Contents

1 Introduction

Directed cellular migration and differential adhesion are crucial for many biological processes in life such as embryogenesis, wound healing or cancer cell metastasis. In order to get a structured and biologically functional organism, embryonal cells which divided from the fertilized oocyte have to sort and spatially reorganize leading to a symmetry breaking of the initially spherical organized cells. In consequence, sorting on the molecular scale introduces defined cellular principal axis and causes anisotropic mechanical and chemical gradients triggering the directional cellular motion. This underlies the formation of organs and tissues.

If tissues or organs, e.g. the skin, are damaged, cells will release chemical signals triggering wound healing. This leads to clotting of red blood cells (RBC) and the activation of fibrin forming a mesh which glues the RBC together. After the wound is cleaned through phagocytosis by white blood cells, growth factors are released into the wound. Subsequently, epithelial and endothelial cells as well as myofibroblasts and fibroblasts move to the wound and divide. The latter ones excrete collagen and fibronectin building up new extracellular matrix. Epithelial cells crawl to the top of the wound and cover it. Myofibroblasts are responsible for wound contraction.

Directional cellular motion plays a crucial role in cancer cell metastasis, too. Cancer cells do not obey regulatory processes of an organism anymore wherefore they are able to grow persistently. Additionally, they are able to disseminate from the original tumor, move within the organism and start metastasis in another location including a directionality in motion as well. The underlying mechanisms driving cellular motion in mammalian cells are similar to those of amoebae as they often do not rely on integrins.

The social amoeba *Dictyostelium discoideum* (*D.d.*) is often used as a model organism in research to investigate cell adhesion and motility, chemotaxis and signal transduction and they are easy to culture. They are not only growing at room temperature and at atmospheric CO_2 concentration but they are haploid, too. Hence, mutants are created by knocking out only one gene which has a direct impact on the phenotype. *D.d.* cells are frequently used to study chemotaxis. After six hours of starvation, *D.d.* cells migrate along the gradient of the concentration of 3'-5'-cyclic Adenosine-Mono-Phosphate (cAMP). Remarkably, the migratory amoebae lack the protein superfamily of integrins and actin stress fibers which is why their motility is mainly affected by actin depolymerization and

polymerization. Therefore, they are attractive model organisms for the investigation of cell migration.

Cellular motion can be guided by mechanical, chemical, magnetic, electrical, thermal or rheological stimuli. In this work, we will mainly focus on mechanical stimuli defined by the topography of the surface that cells migrate on.

Until now, many studies are performed on two-dimensional planar surfaces due to experimental challenges. But in nature, *D.d.* as well as mammalian cells are living in an geometrically complex environment. *D.d.* cells are hunting for bacteria in porous and fluid-filled soil. Thus, they face an anisotropic and heterogeneous environment where they also crawl over curved surfaces. We therefore try to investigate the amoeboid cell migration under more realistic experimental conditions. The aim of this Master thesis is, in the first place, to characterize contact guidance, the directionality of cellular motion in response to surface topography, of *D.d.* on micro-topographical sinusoidal curved substrates. In the second place, we want to elucidate how cell-substrate adhesion is influenced by curved surfaces.

The scope of this work is to fabricate those surfaces including the technical design and 3D printing of negatives of these structures. Subsequently, the autofluorescent negative surfaces are coated with polydimethylsiloxane (PDMS). Then, we observe and quantify the cell migration of *D.d.* cells on the sinusoidal wave structure imprints with a spinning disc confocal laser scanning microscope (sdCLSM). Furthermore, we address the influence of curved surfaces on cell-substrate adhesion with single cell force spectroscopy (SCFS). In this work, it is noteworthy that *D.d.* cells face a surface topography whose curvature varies permanently. It provides regions of convex as well as concave curvatures. For this reason, we look for further detailed inside into contact mediated guidance of cellular motion depending on local and global surface topography.

Chapter 1 introduces the field of research, presents the organism of interest and explains the main ideas behind this work. In chapter 2, the biophysical background is explained including some notes on *D.d.* as well as general actin dynamics in the cellular cortex, cell-substrate adhesion, cell migration and contact guidance. In chapter 3, the experimental setups and methods are presented. The most important technologies are spinning disc confocal laser scanning microscopy, atomic force microscopy and the 3D printer. Chapter 4 sums up results of surface scans acquired from printed substrates and the 3D cell tracks over time. Furthermore, chapter 4 contains the analysis of data from the retrace curve acquired by single cell force spectroscopy. The results are discussed in chapter 5. Possible future projects to answer follow-up questions are proposed as well. We hope that a deeper insight in the directional cell motility will progress medical treatments of wounds.

2 Background

2.1 *Dictyostelium discoideum*

Dictyostelium discoideum (*D.d.*) is a cellular slime mold living in the soil and is frequently used as a model system for chemotaxis, signal transduction and cell motility in research. The social life cycle is displayed in Fig. 2.1. In their so-called vegetative stage, they live in the soil as single cells and hunt for bacteria. In this stage, *D.d.* cells reproduce by binary fission. If the food supply is exhausted, *D.d.* cells enter the following stages within the life cycle. After $\approx 6\,\mathrm{h}$ of starvation, *D.d.* cells begin to release waves of the chemical cAMP with a period of $\approx 6\,\mathrm{min}$ [1]. As *D.d.* cells increase the expression of membrane receptors binding to cAMP (e.g. cAR1) [2], they are able to sense the chemical signals. An occupied receptor cAR1 activates a G protein that transfers the external stimulus to the interior of a *D.d.* cell stimulating pathways for (localized) actin polymerization. Thus, they crawl towards the source of cAMP which is one example for a process known as chemotaxis. More precisely, *D.d.* cells begin to polarize in parallel to the gradient of cAMP and move into the direction of the cAMP source for $\approx 1\,\mathrm{min}$. Then, their shape becomes rounded or rather randomly shaped and they perform random motion for $\approx 5\,\mathrm{min}$ ("cringing"). During this time, cAMP in the vicinity of the cell is removed by an extracellular membrane-associated phosphodiesterase so that the cell is sensitive to the next cAMP wave [3]. The aggregation centers are randomly distributed over the culture and determined by the first cells secreting the chemoattractant cAMP [4]. The chemical signal is relayed by the surrounding cells that begin to secrete cAMP as well. Additionally, genes encoding proteins which are included in cell-substrate and cell-cell adhesion and therefore important for the multicellularity are deactivated or activated, respectively. Together, this leads to a series of radial streaming arms before the aggregation of cells ends up in a multicellular structure composed by 10^5 cells, the so-called mound [3].

Within this mound, cells differentiate into several classes of prespore and prestalk cells that form the mature spore and stalk cells from later stages in the lifecycle. Afterwards, sorting leads to spatial reorganisation which is guided by both chemotaxis and different strength of adhesion forces among all present cell types. In more detail, prestalk cells move to a center of secretion of cAMP being located at the tip of the mount. After growth

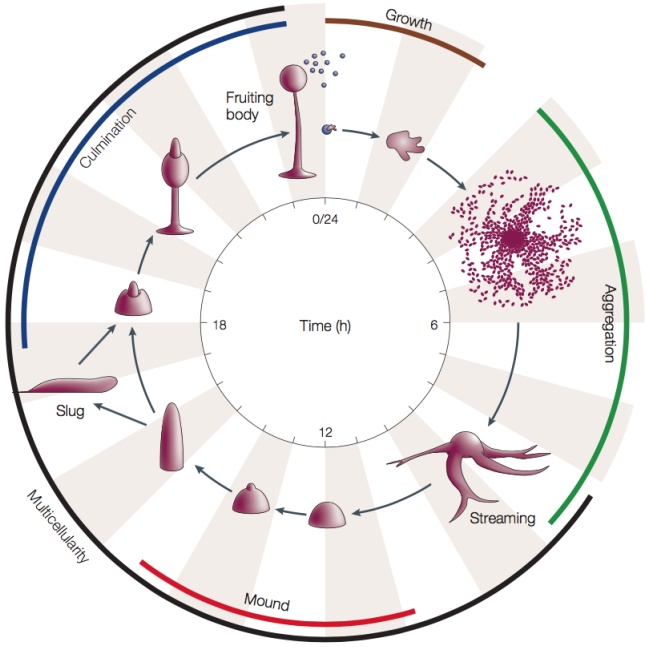

Figure 2.1: Social lifecycle of the social amoebae *Dictyostelium discoideum* (D. d.) starting from single, vegetative cells. The transition from single cells to the mound is mediated by chemotaxis of cells towards cAMP which leads the cells to stream towards aggregation centers. In the mound, cells differentiate into prestalk and prespore cells, sort, and form a tipped aggregate. During further development, the anterior-posterior axis are maintained through a slug stage and early culminate stages. In culmination, a mature fruiting body is build up completing morphogenesis. The fruiting body contains spores which can be germinated if the environmental conditions are suitable. The entire process takes 24 h. From [3].

of the tip and formation of a tipped aggregate cells sort along the anterior-posterior axis. The slug which is formed due to additional elongation of the aggregate is composed of about 25% prestalk cells at the front and 70% prespore cells at the rear of the slug. During the formation of the fruiting body - the stage of culmination - pst cells differentiate into the stalk and the basal disc whereas prespore cells rise to the top [3].

In this thesis, single *D.d.* cells in the stage of early starvation showing high motility are used to acquire tracks in 3D over time.

2.2 Actin Dynamics in the Cellular Cortex

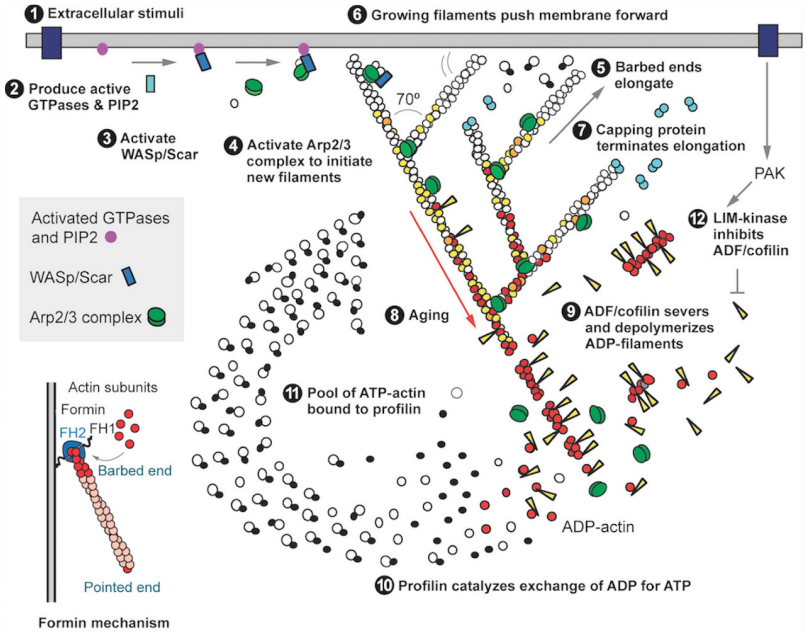

(a) Major processes in the dendritic actin network of the cellular cortex. From [5].

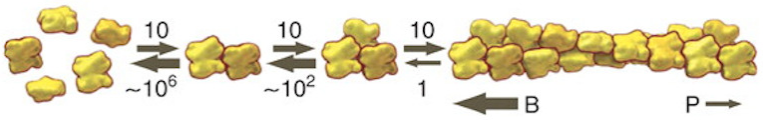

(b) Assembly of monomeric actin to filaments. From [6].

Figure 2.2: Actin dynamics in the cellular cortex and dynamics of single actin monomers assembling to single filaments and vice versa. **(a)** Promoted by WASp/Scar, Arp2/3 binding to a mother filament as well as an actin monomer trigger the nucleation of another filament. The elongation of filaments is blocked by capping proteins. The actin filaments age by hydrolysis of ATP to ADP enabling ADF/cofilin to disassemble the actin filaments into ADP-actin. Binding to Profilin and transforming to ATP-actin, the monomers can nucleate to new growing filaments. **(b)** Spontaneous nucleation and elongation of actin filaments. They grow faster at the barbed end (B) than at the pointed end (P). Dimers and trimers are unstable compared to longer filaments. The numbers in **(b)** represent rate constants in $\mu M^{-1}\,s^{-1}$ for assembly and s^{-1} for disassembly [7].

In *D.d.* cells lacking stress fibers, the actin cortex adjacent to the cell membrane plays a crucial role for cell shape, cell-substrate adhesion and cell migration. The actin cortex is build up by a 100 nm − 200 nm thin layer of actin and is a crosslinked network of actin filaments oriented parallelly to the cellular membrane. This structure is dynamic on time scales of ≈ 1 s determining mechanical properties of the cell and the membrane.

The formation of protrusions is based on localized polymerization orthogonal to the cell membrane. Related dynamics of actin and major components of the dendritic actin network are shown in Fig. 2.2 where globular monomeric G-actin bound to adenosine triphosphate (ATP) polymerizes to actin filaments (Fig. 2.2a). Notably, actin filaments are polar as the ATP molecule is compounded to the barbed end and the monomers in a filament are all bound in the same direction. The polymerization is much faster in the direction of the so-called "barbed" end pointing to the cell membrane than in the opposite direction. Initially, the growth of actin filaments is slow since actin dimers and trimers are quite unstable (as shown in Fig. 2.2b) under physiological conditions without actin-binding proteins. Elongation and nucleation of actin filaments are interrupted by capping proteins [6]. Formins bind to the barbed end of the actin filament. They are able to anchor the filament and prevent capping [5].

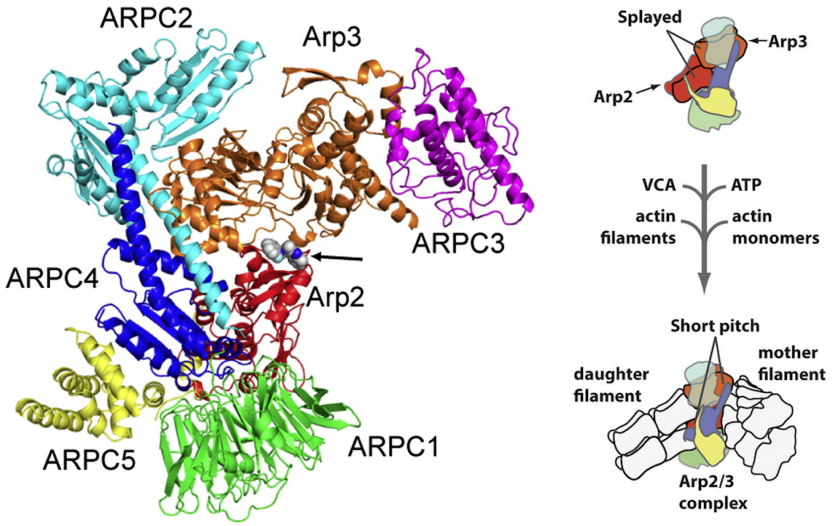

(a) Binding mode of CK666 to the Arp2/3 complex indicated by the arrow.

(b) Branching nucleation reaction.

Figure 2.3: Branching nucleation reaction and activation of Arp2/3 due to conformational change from inactive "splayed" to active "short pitch" configuration. **(a)** Indicated by the black arrow, CK666 binds to the side between Arp2 and Arp3, two of seven subunits forming the entire Arp2/3 complex. The Arp2/3 inhibitor CK666 used in this work binds to the subunit Arpc4. From [8].

The actin filaments disassembly is initiated by hydrolysis of ATP to ADP. Then, slight conformational changes enable actin depolymerizing factors to bind to the F-actin and subsequently F-actin disassembles into globular ADP-actin. If the rates of depolymerization and polymerization are approximately equal, the actin filament transitions into a steady state being known as treadmilling [1] whereby the length of the actin filament remains approximately constant. This type of actin filaments forms loose actin networks in the cortex or in filopodia. But actin filaments are not only elongated by nucleating G-actin. New actin branches can also grow from existing branches initiated by the active Arp2/3 complex [4] where the angle between two branches amounts to $\approx 70°$. The latter type of network is gel-like and predominantly located in membrane protrusions such as pseudopodia.

The actin polymerization dynamics comprise also the nucleation promoting factors SCAR and WASp. They regulate actin branching in changing the spatial conformation of the Arp2/3 complex from "splayed" to "short pitch" that is crucial for its activation (Fig. 2.3b). In doing so, they bind to an actin monomer as well as the Arp2/3 complex and, subsequently, to an actin filament completing the activation. Then, a new actin branch assembles at the barbed end of the actin molecule compound to the Arp2/3 complex [6, 5]. Furthermore, actin filament bending modulates the activity of Arp2/3. Preferentially, Arp2/3 branches new actin filaments at the convex side of the mother filament [9]. During chemotactic cell migration, active patches of RasG, an downstream actin polymerization stimulating protein, F-actin and membrane curvature coincide well [10]. Hecht *et al.* formulate a reaction-diffusion model to describe the dynamics of RasG patches. Coupling the RasG patches to a force field, amoeboid cell motility can be simulated reasonably [11].

2.3 Cell-Substrate Adhesion

Cell-substrate adhesion plays a key role in cellular motility. Without exerting and transmitting forces to their environment, cells would not be able to move actively. Generally, the cells interact with the extracellular space through many important proteins incorporated in the oscillating membrane [12].

In mammalian cells, the interaction with the environment is guaranteed through integrin proteins that can bind to the extracellular matrix. Within the cell, the integrin proteins are connected to actin network with the help of actin-binding proteins like talin, α-actinin, filamin, paxillin or vinculin. Often, the integrin proteins assemble in patches at

the cell membrane leading to so-called focal adhesions (Fig. 2.4a) as the actin filaments point orthogonally to the integrin patches. Importantly, focal adhesions are stable as they keep the cell attached to the surface, e.g. extracellular matrix consisting of collagen, fibronectin, laminin or vitronectin [13] until the cell moves forward.

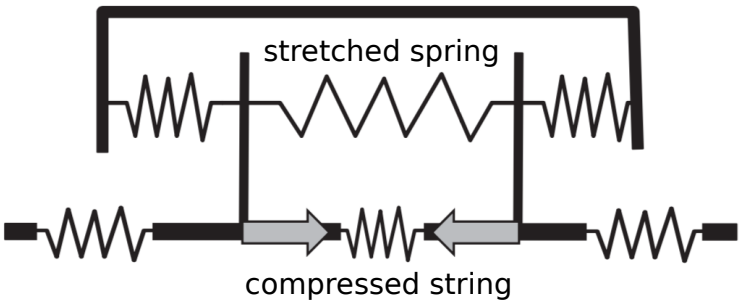

(a) Force dipole model of an adherent cell.

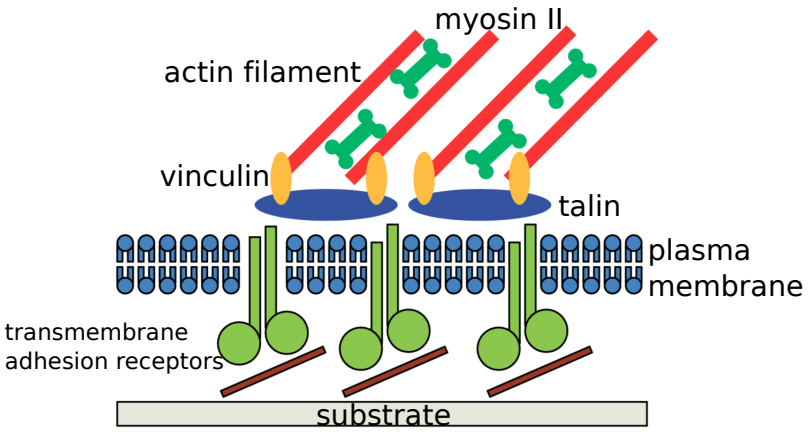

(b) Important components of a focal adhesion.

Figure 2.4: Forces related to the actin cytoskeleton for adherent cells **(a)** and focal adhesion complex **(b)**. In **(a)**, compressed springs represent lamellipodia (pseudopodia for *D.d.* cells) as they exert a pushing force outward on the cell membrane as well as inward on the focal adhesions. Stress fibers pull inward on the adhesion sites due to myosin-mediated contractility, among others, which is why they are drawn as a stretched spring. **(b)** Focal adhesion. Activated transmembrane adhesion receptors can bind to a substrate, e.g. extracellular matrix. Within the cell, talin and vinculin can bind to both the transmembrane adhesion proteins and actin filaments. This leads to stabilization of the adhesion site. Modified from [14].

Despite that *D.d.* cells lack integrins, they are able to crawl on pure glass substrates.

The adhesion is sufficiently strong to resist external applied fluid flow ($< 6.5\,\mathrm{Pa}$) expected to be strong enough to wash away secreted material. The underlying force is not only determined by hydrogen bonds or covalent, ionic interactions. Instead, their adhesion is mainly based on van der Waals forces which appear due to the glycoproteins on the cell surface interacting with the substratum [15]. Moreover, the adhesion strength decreases over time by regulating down the expression of SadA and SibA wherefore the motility of *D.d.* increased due to starvation. Since actin cortex is essential for the cell shape and taking into account that the strength of attractive van der Waals interaction is a function of distance, the strength of adhesion depends on actin dynamics [13]. For further information on the role of SadA, the reader is referred to [16].

From a mechanical point of view, an adherent, stationary as well as polarized cell resembles a contractile force dipole in mechanical equilibrium such as shown in Fig. 2.4a. Pushing forces originate from actin polymerization within a lamellipodium or pseudopodium for *D.d.* cells and pushes the cell membrane outward. Simultaneously, the adhesion sites are pushed inward. Additionally, there are pulling forces towards the cell interior being related to myosinII-induced contractility in the actin cytoskeleton. In total, both pushing as well as pulling forces are directed inward which creates a tension on the substrate. The system is bounded by the cell membrane [14].

2.4 Cellular Motion

Generally, biological cells are systems at low Reynolds numbers in fluid environments. Therefore, they encounter high frictional forces while inertia is negligible. In consequence, they have to exert forces to their physical environment in order to move [17]. Cellular motility is a result of an interplay between myosinII contractility, pushing forces due to actin polymerization and cell-substrate adhesion providing force transmission [1]. These forces are the product of many molecular and dynamic processes within the cortex and cytoskeleton of the cell (see section 2.2).

On the one hand, actin polymerization and actin branching lead to pseudopod formation which subsequently adheres to the substrate. Myosin II is incorporated at the sides of cell protrusions and in regions where the membrane surface curvature is low, stabilizing the direction protrusion formation[18]. Additionally, Blum *et al.* observed that myosinII is located between two splitting pseudopods and initially at the position of *de novo* pseudopod formation, too [10]. Therefore, an interplay between contraction related to myosinII and pushing forces due to actin polymerization and branching results in a pushing

force and an increased tension over the entire cell body. On the other hand, myosinII-induced contractility at the cell rear, together with increased tension, is responsible for retraction of the tail. Furthermore, this contractility inhibits formation of protrusions such as pseudopodia at the cell rear. On a molecular scale, myosinII motors are binding to actin branches. Hydrolyzation of ATP provides the energy for the myosinII motor to slight along the actin branch inducing the contractile force. As the actin cortex is connected to adhesion sites, the sum of all contractile forces on a molecular scale leads to breakage of adhesion sites [19].

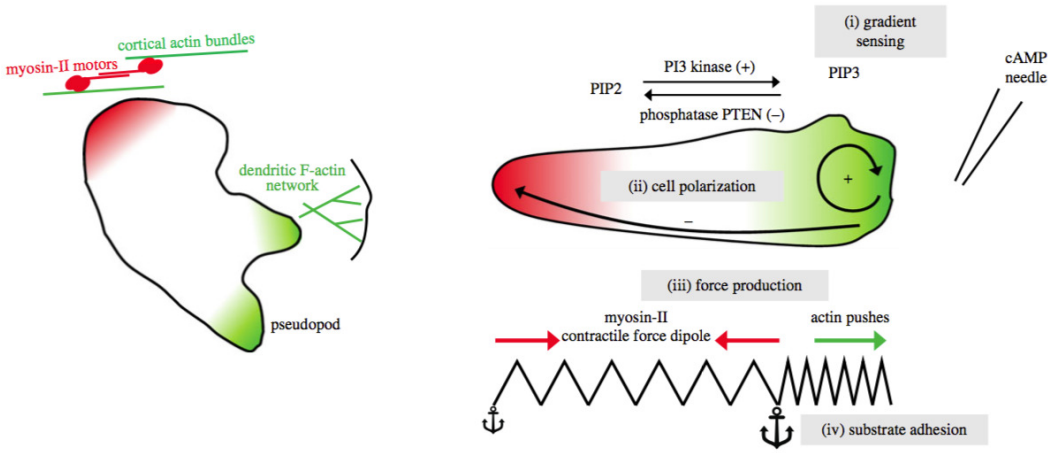

Figure 2.5: Random (left) and directed (right) motility due to chemotaxis. In random motility, pseudopodia form spontaneously based on pushing forces generated by actin polymerization. myosinII-mediated contractility at the uropod leads to retraction of the tail and inhibits the formation of membrane protrusions. Chemotactic cells reveal a polarized cell shape. An external cAMP stimulus activates Ras that breaks the symmetry of PIP2/PIP3 distribution within the cell downstream the signal cascade. PIP3 enhances the actin polymerization at the leading edge whereas PTEN, located at the uropod and both sides of the cell, inhibits the PI3K pathway, thus actin polymerization. Together with the myosinII contractility, this yields a force dipole retraction of the tail. Cell adhesion is needed to transmit forces to the substrate. From [1].

Beside blebbing [20], *D.d.* cells basically show two different kinds of cellular motion depending on their developmental stage. Under favorable environmental conditions, they exhibit random motion whereas they show directed motion and high polarization if they are starved and exposed to a gradient of cAMP [3]. When cAMP molecules bind to a cAMP receptor (cAR1) at the front of the *D.d.*, actin polymerization at the leading edge is amplified building up membrane protrusions known as pseudopodia. cAMP binding to cAR1 triggers a signal cascade. After disassembly into the subunits Gα and

G$\beta\gamma$, the G protein subunits initiate activation of Ras resulting in activation of PI3K phosphorylating PIP2 to PIP3. Downstream the signal cascade, this creates symmetry break of PIP2/PIP3 at the cell front and phosphatase PTEN at the sides as well as at the uropod [21] as shown schematically in Fig. 2.5. The assembly of actin to a network is even accelerated by the Arp2/3 complex [1]. Likewise, actin is also polymerized at the rear of the cell and assembles with myosinII.

2.5 Contact Guidance

In nature, *D.d.* cells live in the soil and face a geometrically complex environment. But the majority of experiments on cellular migration are performed on planar surfaces. To investigate amoeboid cell migration under more realistic conditions, we expose the *D.d.* to optical fibers and to sinusoidal wave structures.

Already in 1952, Weiss *et al.* found out that the local surface structures bias the cellular migration [22]. In 1976, G.A. Dunn and J.P. Health probed the behavior of chicken heart fibroblasts on, among others, cylindrical glass fibers of radii $< 200\,\mu m$. The fibroblasts revealed elongation in the direction of the cylinder axis up to a radius of $100\,\mu m$. They also observed a threshold behavior on prism ridges, since the cells did not show any response for ridge angles $< 4°$. They defined "contact guidance" as the directionality of the migratory response parallel to the direction of least curvature on the substrate [23].

To get a deeper insight in the mechanism of contact guidance, Sun *et al.* exposed amoeboid *D.d.* cells and human neutrophils to locally asymmetric nano- and micrometric sawteeth. The length of sawteeth varied from $1\,\mu m - 8\,\mu m$, the height from $0.4\,\mu m - 2.4\,\mu m$, the width from $400\,nm - 630\,nm$ whereas the spacing ranged from $0.4\,\mu m - 2\,\mu m$. Hence, the structure sizes are comparable to collagen fibers. In contrast to *D.d.* cells breeding pseudopodia in order to crawl, human neutrophils migrate via forming lamellipodia. Both cell types migrated unidirectionally whereby the dominance of contact guidance depends on the structure geometry and its scales. Sun *et al.* showed that the surface structure confines the actin polymerization waves within a cell to the same direction that the cells migrate [24]. Lateral confinement in channels of $5\,\mu m - 20\,\mu m$ width and of $20\,\mu m$ height is responsible for symmetry breaking in actin polymerization and thus for unidirectional motion [25].

Furthermore, the cellular migration of amoeboid *D.d.* cells on nanotopographic surfaces was examined by Discroll *et al.* They created structures including nanoridges with the constant spacing of $0.4\,\mu m - 10\,\mu m$, a width of $250\,nm$ and height of several hundred nm

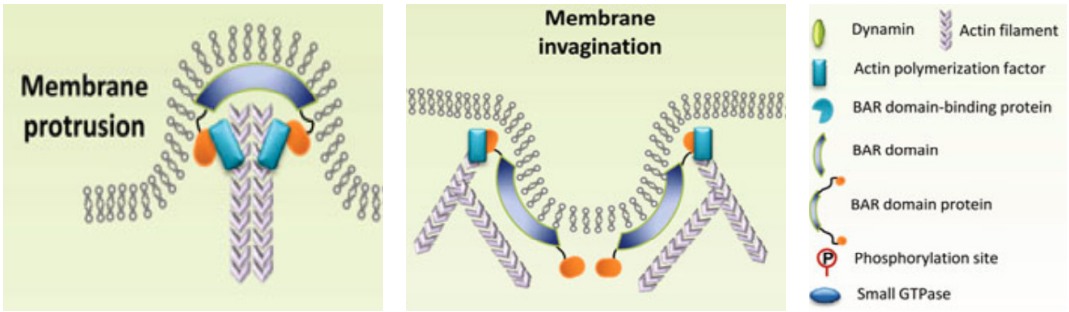

Figure 2.6: BAR domain superfamily proteins bind to curved membrane surfaces like membrane protrusions and invaginations. BAR proteins also activate the WASP/WAVE -Arp2/3 actin polymerization pathway. Modified from [28].

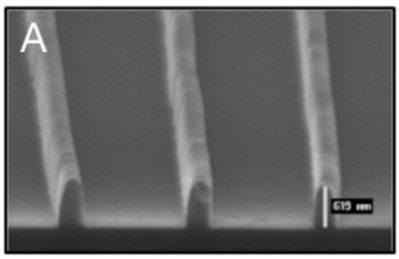

Figure 2.7: SEM image of three parallel nanoridges. Each nanoridge has a height of $\approx 600\,\text{nm}$ and a width of $\approx 250\,\text{nm}$. The scale bar corresponds to a length 619 nm. From [26].

as presented in Fig. 2.7. They observed that cells oriented parallel to the nanoridges move faster, form a more protrusive cell front, and are more polarized than cells oriented orthogonal to the nanoridges. Thus, nanotopography leads to contact guidance for cells without integrins. As a matter of fact, the directionality of cellular motion for chemotactic *D.d.* cells is comparable to the directionality of *D.d.* cells directed by contact guidance. Discroll *et al.* figured out from experiments, as well as from a damped harmonic oscillator model, that amoeboid *D.d.* cells are sensitive to their environment on time and length scales comparable to the scales for observed actin dynamics. They suggest this as a reason for contact guidance on nanotopographical surfaces [26]. Besides, if cells are adherent to curved substrates, their membrane also adopts the substrate curvature. Thereby, BAR domain superfamily proteins can bind to curved membrane regions (Fig. 2.6) with a diameter of several hundred nm stabilizing the membrane shape. Additionally, the BAR proteins can activate the WASp/WAVE -Arp2/3 actin polymerization pathway that adjusts the orientation of actin filaments towards the membrane resulting in membrane protrusions or invaginations [27].

Likewise, migrating *D.d.* cells on bone-shaped silica substrates (width $(24 \pm 8)\,\mu\text{m}$,

Cell type	Topography	Width [µm]	Height [µm]	Spacing [µm]
D.d. cells	sawteeth	$0.4 - 0.63$	$0.4 - 2.4$	$0.4 - 2$
D.d. cells	channel	$5 - 20$	20	
D.d. cells	nanoridges	0.25	≈ 0.6	$0.4 - 10$
D.d. cells	bone shaped	24 ± 8	60 ± 20	
T cells	sinusoidal waves	$\lambda = 20 - 160$		
fibroblasts	cylindrical fibers	$r < 200$		

Table 2.1: Overview of length scales, cell types and topographies in contact guidance related experiments. λ denotes the wavelength of sinusoidal-shaped waves and r the radius of cylindrical glass fibers.

height $(60 \pm 20)\,\mu m$) do not only show a more persistent directionality but also faster motion and higher motility compared to cells on planar glass substrates where the motility is estimated by a generalized diffusion coefficient. Emmert *et al.* demonstrated, furthermore, that myosinII and microtubuli play a crucial role in contact guidance. On planar surfaces, *D.d.* cells lacking myosinII move slower compared to *D.d.* cells with myosinII because the retraction of the cell rear is inhibited. Accordingly, myosinII-deficient cells are hindered in polarizing and they build up more actin foci. Surprisingly, the motility of myosinII null mutant *D.d.* cells does not change significantly on silica fibers in comparison to healthy *D.d.* cells. This points out that pseudopodia might be stabilized by surface curvature enabling cells to migrate even with reduced cortical tension. Notably, microtubuli are directly connected to the cellular actin cortex. Cells lacking microtubuli do mostly not adhere to a curved surface, contrarily to those exposed to flat surfaces. This behavior indicates that actin foci, directly connected to the actin cortex, underlie the migration mechanism [29].

Since many microscale structures in nature, such as blood vessels or bone cavities, are smooth, T cells face smooth sinusoidal wave structures with constant amplitude $A = 10\,\mu m$ and varying wavelength $\lambda = 20\,\mu m - 160\,\mu m$ [30]. According to [26, 29], the movement of T cells is also biased by surface curvature migrating within regions of concave curvature. Song *et al.* showed that T cells lacking myosinII are mostly caged within concave surfaces, in contrast to T cells treated with CK636 inhibiting the actin branching in lamellipodia (see section 2.2). They concluded that cells are able to sense curvatures with the help of lamellipodia. Within lamellipodia, actin polymerization is biased by surface curvature such that actin in T cells polymerizes in the direction of concave curvature. Furthermore, contractility due to myosinII activity reduces the curvature sensitivity of T cells and causes the cells to move away from regions of high curvatures but enhances the velocity [30].

From a purely mechanical point of view, cells always tend to minimize the total energy of deformation. Thus, the orientational response of cells to surface structures with convex curvatures underlies the competition between shear forces due to the contractility of the cytoskeleton, adhesion forces and bending of actin stress fibers. Accordingly, being exposed to cylindrical surfaces, cells with thick actin stress fibers, such as fibroblasts, are predicted to orient parallel to the cylinder axis since bending of the stiff actin stress fibers costs lots of energy. In contrast to fibroblasts, epithelial cells comprising thinner stress fibers, respectively a stiffer cytoskeleton, align orthogonally to the cylindrical axis, i.e. the direction of maximal curvature [31]. Moreover, surface curvature provides a mechanical stimulus in bending actin filaments which reduces the maximal contraction force of the cell [32]. Although *D.d.* cells lack actin stress fibers, their reaction to anisotropic substrates will be a superposition of bending of the cellular cortex and the contraction-induced shear stress.

3 Material and Methods

3.1 Cell Culture and Developement

The *D.d.* cell strains used in this work are axenic cell lines [33] meaning that the cells are cultured in an HL5 medium (HLG0101, Formedium) which does not comprise other living creatures. In [34], Fey *et al.* explain how to store, grow and develop *D.d.* cells on long terms. It is important to refresh cell cultures every $2-4$ weeks from permanent stocks in order to forestall genetic mutations within the cell culture. *D.d.* cells can be stocked permanently as spores or as cells frozen at $-80\,^{\circ}\mathrm{C}$.

To make the *D.d.* cells available for experiments, they have to be defreezed in a water bath of $\approx 21\,^{\circ}\mathrm{C} - 23\,^{\circ}\mathrm{C}$. Then, they are plated on petri dishes containing HL5 medium, also at room temperature providing a doubling time of $8\,\mathrm{h} - 9\,\mathrm{h}$. Since it is not preferable to exceed cell concentrations of $4 \times 10^6\,\mathrm{mL}^{-1}$, the cells have to be subcultured every $2-3$ days. In doing so, a dilution of 1:100 has to be applied. The subculturing procedure is repeated maximum 15 times to avoid genetic mutations. In the context of this work, mainly two different cell lines are used: Aca0 mRFPmars-LimΔcoil + myosinII-GFP and Ax2 Arpc4-GFP + LimE-mRFP. The label mRFPmars-LimΔcoil is provided by the group of A. Müller-Taubenberger (Med. Faculty, LMU Munich, [35]), myosinII-GFP by the group of A. Kortholt (University of Groningen, [36]) and pDM528 Arpc4-GFP by the group of D. Veltman (MRC LMB Cambridge, [37]).

The experiments are done with cells in their exponential growth phase (compare Fig. 2.1). *D.d.* cells are pulsed with cAMP for 6 h to render them chemotactic. Therefore, *D.d.* cells get polarized which allows them to migrate faster. For the experiments related to investigations on contact guidance, *D.d.* cells lacking adenylyl cyclase (Aca) are used to exclude aggregation effects in the cell tracks because this knock-out is not able to produce cAMP. In addition, chemical stimuli through external cAMP release are not applied in the experimental setup, we can approximately neglect chemotactic effects even if the cells are still able to sense cAMP.

For the single cell force spectroscopy, Ax2 mRFPmars-LimΔcoil + pDM528 Arpc4-GFP cells are used. With the aim of elucidating the role of the cortical tension in curvotaxis, this cell line is treated with CK666 providing inhibition of the Arp2/3 complex (section

2.2). Their preparation starts with washing the cells with phosphate buffer before the cells are counted. Then, CK666 is added with concentrations of 5 µM, 10 µM and 100 µM to the cell culture and incubated for 30 min (see section 3.2.1). After this time period, the cells are centrifuged and, subsequently, washed twice. In the end, the cells are counted again to ensure a cell concentration of $3 \times 10^5\,\mathrm{mL}^{-1}$ which is desirable since it leads to easily manageable cell numbers during the single cell force spectroscopy.

3.1.1 Pulsing

Pulsing *D.d.* cells begins one day before the actual experiment starts. At first, 1×10^6 cells are pipetted into a flask containing 25 mL of HL5 medium. This flask is fixed to a holder on a shaking table (SHKE - 2001CE, Thermo scientific) rotating with a rate of $150\,\mathrm{min}^{-1}$ at room temperature.

Then, the cells have to be centrifuged (centrifuge 5810R, eppendorf) with 1000 rpm for 3 min at 4 °C to remove the medium 7 h before the measurement starts. Subsequently, cells are washed with phosphate buffer and centrifuged another time, always with the same parameters. After throwing away the supernatant, the remaining pellet is diluted with 20 mL of the phosphate buffer. Afterwards, the pulsing begins technically in putting a flask with the liquid on the shaking table and in releasing a ≈ 60 µL droplet with a concentration ≈ 18 µM of cAMP (provided by Sigma-Aldrich) every 6 min.

3.2 Experimental Setups

3.2.1 Atomic Force Microscopy

Technology and Exemplary Setup

Since we want to investigate the influence of surface curvature on *D.d.* cell migration and cell-substrate adhesion, sinusoidal surfaces have to be designed and printed. The roughness and quality of the surface curvature has to be quantified before performing the data acquisition via single cell force spectroscopy and spinning disc confocal laser scanning microscopy.

In this work, atomic force microscopy (AFM) is used to scan the surfaces of 3D printed

structures (MFP-3D™, Asylum Research, [38]) in contact mode as well as to perform single cell force spectroscopy (Cellhesion 200, JPK Instruments AG). A standard head configuration of the MFP-3D™ is shown in Fig. 3.1. The principle behind this technique is usually applied in other devices, too, and explained exemplarily in the following.

An elementary component for AFM scanners is the piezoelectric crystal which sets the position of a sharp cantilever tip in response to a voltage. It also provides the oscillations required for tapping in AC (alternating current) mode. Both facilities are based on the piezo-electric effect where a crystal expands or shrinks as a response to an externally applied voltage. The MFP-3D™ AFM has three piezo-stacks to move the cantilever in all three spatial directions. In z-direction, the piezo displaces not only the cantilever but also the associated light source. Since the response of piezoelectric crystals to a command voltage is non-linear (hysteresis), occurring errors have to be eliminated by a nano-positioning system (NPS). The NPS in z-direction comprises two components. The first component detects the deviation from the desired position due to the hysteresis of the piezo-response. The second includes a feedback loop which keeps the cantilever on the commanded trajectory in transferring the NPS sensor information to the controller.

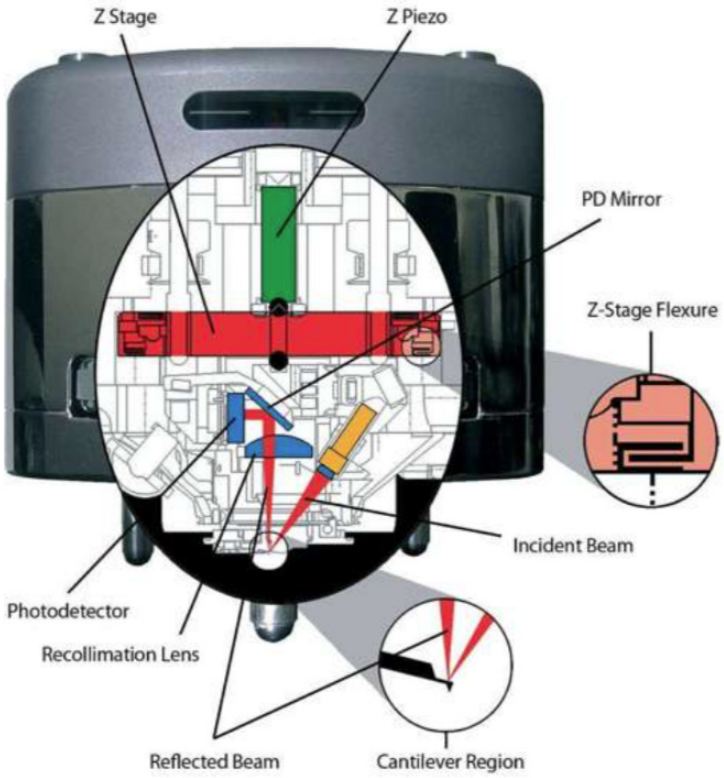

Figure 3.1: Scheme of standard AFM head including laser light path. From [38].

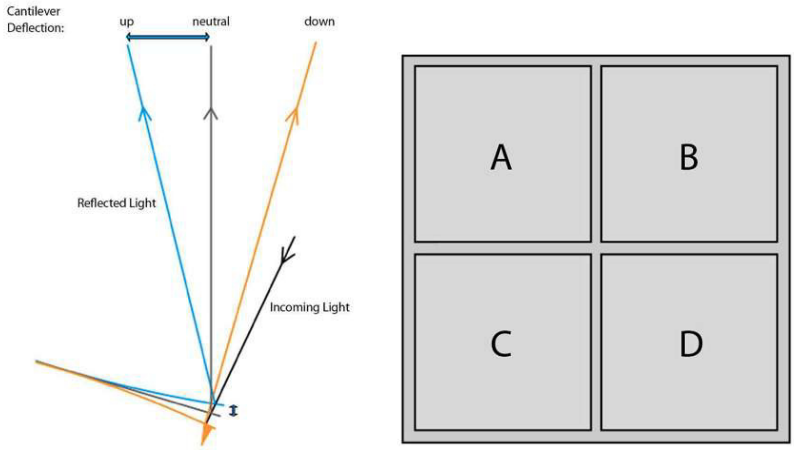

(a) Cantilever deflection (b) Photodetector

Figure 3.2: Quadrants of a photodetector (right) transforming laser intensity into electrical voltage whereby the laser is reflected by the cantilever tip (left). Deflection is dependent on the bending of the cantilever. From [38].

For measuring forces, a frequently used method is the optical lever detection. This method detects the bending of the cantilever tip interacting with a surface due to mainly electrostatic forces. As depicted in the schematic Fig. 3.1, light is focused on and reflected by the tip of a cantilever through an optical path onto a photo detector. The cantilever is mounted with an angle of 11° to the surface. The optical path comprises a mirror by which the light beam is adjusted to the center of the detector. As the cantilever is bent, the incident angle of the light onto the cantilever tip varies (Fig. 3.2a) and, in consequence, the light spot on the photodetector as well. Due to the large length of the optical path, the bending of the cantilever is amplified leading to high resolution.

According to Fig. 3.2b, the photodiode comprises four sections A, B, C and D. Each section induces a specific voltage as a function of its light illumination. Then, the deflection (lateral signal) is defined as the difference between the voltages generated by top and bottom (left and right) quadrants:

$$\text{Deflection} = V_{top} - V_{bottom} = (V_A + A_B) - (V_C + V_D) \,, \tag{3.1}$$

$$\text{Lateral} = V_{left} - V_{right} = (V_A + A_C) - (V_B + V_D) \,. \tag{3.2}$$

Before the actual measurement, the laser spot should be precisely aligned on the center of the photo diode when the cantilever is in its equilibrium position, i.e. far away from any surface. If the cantilever is exposed to an attractive force, it bends downwards

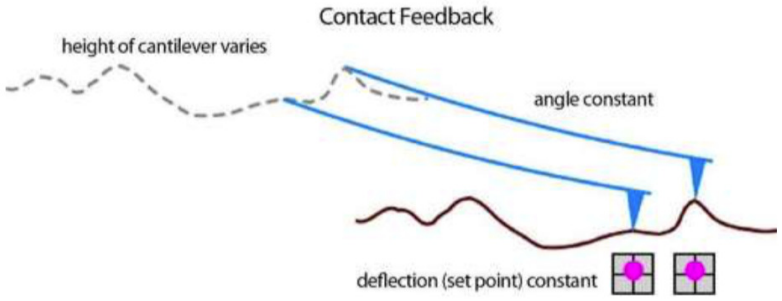

Figure 3.3: Imaging in contact mode. The height profile of a surface is acquired with the help of a feedback loop keeping the deflection constant. From [38].

and the spot orients towards the bottom half of the photo diode leading to a negative deflection and vice versa.

Calibration

First, the cantilever has to be calibrated. In doing so, the sensitivity of the cantilever has to be determined. The sensitivity is a parameter that measures the voltage generated by the photo diode depending on the cantilever deflection. This parameter is influenced mainly by the setup itself (optical elements and photo diode) and the cantilever (length, geometry, etc.).

Afterwards, the cantilever deflection is converted from volts to meter. With the spring constant k acquired from thermal noise calibration [39], the force F experienced by a cantilever during a surface approach can be calculated from Hook's Law

$$F = -k \cdot \delta z = -k \cdot S_z \cdot \delta U_z \ , \tag{3.3}$$

where δz denotes the cantilever deflection in z-direction in unit of length, δU_z (V) the cantilever voltage deflection, and S_z ($\mathrm{nm\,V^{-1}}$) the sensitivity in z-direction. The force constant k ($\mathrm{N\,m^{-1}}$) of the cantilever can be calibrated with different methods among which thermal noise measurement can be done in liquid. Further information is available in [17, 40].

Imaging in Contact Mode

In order to determine the characteristics of a surface, such as roughness or geometry, a sample has to be scanned with the help of an AFM. Using the MFP-3D™ AFM, there

are basically two different modes, namely AC and contact mode. Here, we use only the latter one in combination with MLCT cantilever (Bruker AFM Probes, Fig. 3.4).

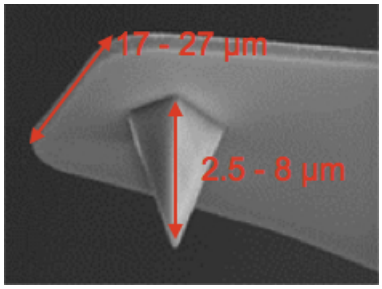

Figure 3.4: Geometry and measures of MLCT Bruker AFM Probes cantilever tip. From [41].

In the case of scanning a surface without any NPS feedback, the cantilever would permanently vary corresponding to height changes on the sample surface whereas the height of cantilever would not be adapted. Likewise, the deflection signal would vary being unfavorable since the force experienced by the cantilever would not be constant. This is not desirable since the z-range would be very small. This constraint can be revoked by adjusting the z-position of the z-piezo. As mentioned above, since the piezo (in z-direction) is controlled by a feedback loop, it moves in z-direction in order to keep the deflection, and, therefore, the force experienced by the cantilever, constant. The value of the set point, then, defines the standard deflection of the cantilever. If the deflection signal exceeds (or is inferior to) the set point, the z-piezo moves up (or down) so that the deflection decreases (or increases). In consequence, the z-position of the z-piezo indicates the height profile of the sample surface along the scan direction (Fig. 3.3). It is advantageous that the z-range is only limited by the z-piezo being larger than the range of the cantilever. Furthermore, the force exerted on the cantilever tip is constant avoiding high forces that could damage the cantilever tip.

If there is a difference ϵ between deflection and set point, the feedback signal varies the z-position of the cantilever in order to minimize ϵ. The response to the difference is higher for larger gains and defined by

$$\text{Feedback} = P \cdot \epsilon + I \cdot \int \epsilon \, \mathrm{d}t + S \cdot \iint \epsilon \, \mathrm{d}t' \, \mathrm{d}t \, , \tag{3.4}$$

where P represents the proportional, I the integral and S the secret gain. The latter one affects the x- and y-piezos and equals zero for the deflection feedback loop in z-direction. The other two gains (P and I) have to be set by the user for acquiring accurate images of the sample. Otherwise, the response of the piezo is not sufficient or too high that leads

to oscillations.

Single Cell Force Spectroscopy

Single cell force spectroscopy provides an experimental mean to investigate cellular adhesion including interactions between trans-membrane proteins and the surface as well as glycocalyx and membranes. Experiments for single cell force spectroscopy are done with Cellhesion 200 (JPK instruments) in combination with tipless silicon spm-sensors (Arrow-TL2-50, NanoWorld, spring constant $k = 0.03\,\mathrm{N\,m^{-1}}$, resonance frequency $f = 6\,\mathrm{kHz}$). The Cellhesion 200 has only a z-piezo having a range of 100 µm. The control software is provided by JPK NanoWizard Control (JPK Instruments).

Before starting the measurement, cells have to adhere to the substrate for 15 min − 30 min. First, *D.d.* cells are picked at the underside of a cantilever tip at the front. Then, the tip is slowly lifted so that the cells detach from the substrate while they remain attached to the tip. After $\approx 60\,\mathrm{s}$, the adhesion between *D.d.* cells and the cantilever tip is sufficiently strong to start with the technical measurement. To begin, the cantilever as well as the attached cell are moved to the desired position. This position is adequately far away from the location of picking and in a convexly curved region around a maximum of the sinusoidally shaped wave substrates. Next, the cell undergoes approach-retraction-cycles with the parameter settings shown in table 3.1. After 10 cycles, the cell is washed away from the cantilever tip by alternating crossing the interface between water and air several times carefully.

Parameter	Value
Set point	0.5 nN
Pulling length	60 µm
Extend speed	$2.5\,\mu\mathrm{m\,s^{-1}}$
Contact time	30 s
Sample rate	6000 Hz

Table 3.1: Parameter settings for single cell force spectroscopy with Cellhesion 200 (JPK instruments).

To quantify certain characteristics of *D.d.* cell adhesion on curved surfaces, an entire set of parameters is analyzed comprising the work of adhesion W_A, maximal force of adhesion F_{ad}^{max}, lifetime τ, height of last step h_{ls}, and number of steps N. The maximal force adhesion F_{ad}^{max} represents a first estimation for adhesion strength as it accounts for the maximal value of the force. Therefore, it sums up specific and unspecific interactions. The work of adhesion W_A, or rather work of de-adhesion, is the area enveloped by the

retraction force curve and the distance axis. This parameter is a measure for energy dissipation due to separation from the surface. In principle, tether building or other membrane deformations contribute to W_A. Since the membrane excess in cells is usually considered as infinite, membrane tethers are build in response to mechanical load by cells in order to avoid detachment of adhesion proteins from the membrane. The lifetime of a bond τ is determined by the retraction velocity and the position of last detachment event, namely the last step. The height of last step h_{ls} is used as an estimator for which proteins are involved in the anchoring to the substrate. Moreover, cells build up membrane tethers from their membrane reservoirs when an external force pulls them away from a surface. Therefore, the force at the membrane anchorage and the binding site remains constant that keeps the cells attached to the substrate. In a force distance curve detected with constant retraction velocity, a membrane tether is identified with an approximately constant force plateau followed by a rupture event, i.e. a step in the force-distance curve. The number of steps N counts the number of bond rupture events followed by force plateaus whereby it represents an indicator for distributions of clusters on the underside of the cell [12]. Additionally, there are single-molecule detachment events during initial retraction yielding an irregular structure. They are not analyzed in this work.

Cantilever Functionalization

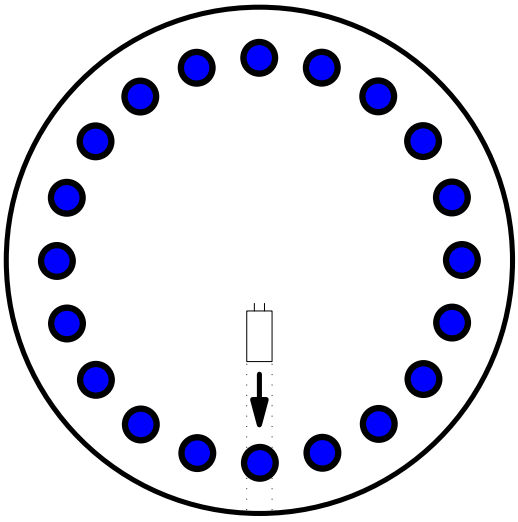

Figure 3.5: Sketch of the holder designed by Nadine Kamprad. The cantilevers are put into the accurate sized holes where the technical functionalization with CellTAK takes place.

For the experiments, we use tipless silicon spm-sensors (Arrow-TL2-50, NanoWorld). They have to be functionalized with CellTAK (BD Bioscience 354240, storage at 4 °C) so that *D.d.* cells stick strongly to the cantilever enabling measurement series of several ($N \approx 10$) repetitions with one single cell. Then, the cantilevers are put into the holder as shown in Fig. 3.5. Afterwards, we fill in the holes with a solution of 16.6 µL and 500 µl 0.1 M $NaHCO_3$ (1:30 dilution) so that the entire cantilever is coated. After 30 min of incubation, the solution is pipetted away and the holes are three times washed with bidistilled H_2O three times. In the end, the cantilevers have to dry.

Arp2/3 Inhibitor CK666

As reported in section 2.5 and 4.3, the directionality of cellular motion is confined by surface topography. To elucidate how the actin cortex mediates cell-substrate adhesion on surfaces of varying curvatures, the nucleation and branching of filamentous actin in the cellular cortex must be inhibited [8]. Therefore, the transition from inactive "splayed" into the active "short pitch" state, enabling the Arp2/3 to branch new actin filaments, has to be blocked. Inhibition of Arp2/3 not only reduces the number of cross-links in the filamentous actin network but also hinders the formation of pseudopodia in *D.d.* cells and, consequently, impacts the cell shape. Moreover, cortical actin contributes to cell-substrate adhesion. Hence, we want to investigate how pharmalogical treatment with CK666 changes the adhesive properties of *D.d.* cells on curved surfaces.

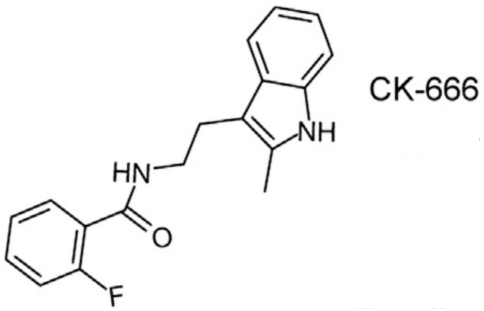

Figure 3.6: Chemical structure of Arp2/3 inhibitor CK666. From [8].

The Arp2/3 inhibitor CK666 binds to the Arp2/3 complex between the subunits Arp2 and Arp3 indicated by the arrow in Fig. 2.3a. Since the binding blocks conformational change of Arp2/3 from the inactivated "splayed" to the activated "short pitch" state, CK666 inhibits the nucleation of filamentous actin in the cellular cortex. More precisely, the inhibitor CK666 stabilizes the inactive state of Arp2/3. It has been shown that CK666 does not change the spatial organization of the subunits and does not stimulate the disassembly of actin networks, too, since both the rate constants before and after

treatment with CK666 are equal. This is favorable as the complex does not loose its functionalities. CK666 only affects the actin nucleation and not the nucleation promoting factors and, therefore, CK666 is useful to investigate the actin network initiation in the absence of branching nucleation.

3.2.2 Spinning Disc Confocal Laser Scanning Microscopy

In confocal microscopy, an excitation laser passes through a pinhole and excites the fluorophores in the specimen. This technique is desirable because it reduces the out-of-focus signals through a pinhole blocking non-focal emission light as shown in Fig. 3.7. This ensures an increase in axial and lateral resolution. In confocal laser scanning microscopy, the specimen is illuminated by a single excitation light spot scanning the region of interest in a certain raster pattern. The beam is guided by the galvano-mirror method where the emission signal is detected by a photo multiplier. This technique is particularly limited in temporal resolution.

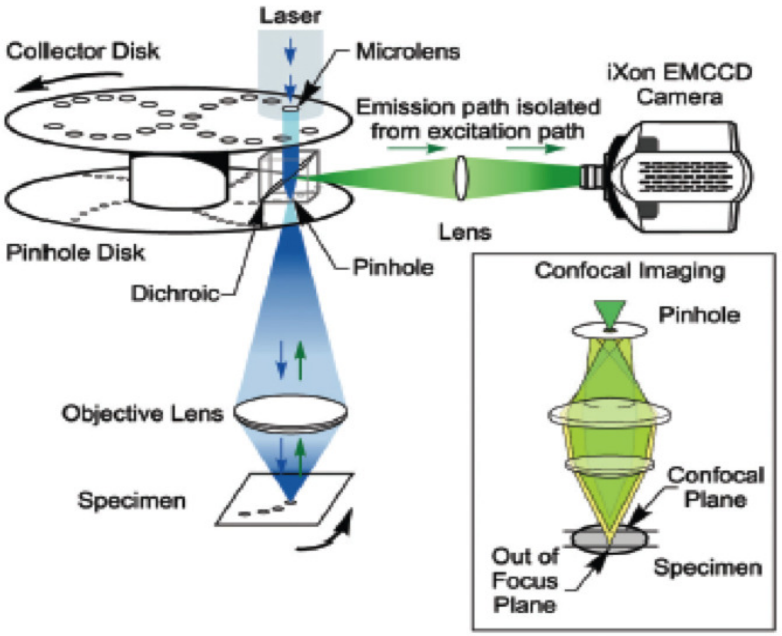

Figure 3.7: Dual disc arrangement for the spinning disc confocal laser scanning microscope (sdCLSM). The second disc comprises microlenses that are adjusted to first disc (that contains pinholes). Hence, excitation efficiency is improved compared to classical configuration. From [42].

Spinning disc confocal laser scanning microscope (sdCLSM) provides another mean for

imaging the dynamic cellular migration on curved substrates. The technique originates from confocal microscopes and was developed to increase the temporal resolution for biological specimen. The setup of a sdCLSM is shown in Fig. 3.7. It comprises one rotating disc with an array of multiple pinholes, a second rotating disc with multipe microlenses, and usually a CCD or EMCCD camera where each microlense is matching to a pinhole [43]. The excitation laser beam is widened and illuminates a certain section of the array of microlenses. They focus the light on the pinholes which leads to a simultaneous excitation of multiple spots in the focal plane. Importantly, the pinholes are arranged in a manner that the entire field of view is covered by the excitation laser after rotation.

After excitation being the strongest in the focal plane, emission light is radiated partially in direction of the optical path and focused on the pinhole array. It is axially located in the first image plane of the microscope. According to conventional confocal microscopy, only confocal light can pass the pinholes where it is afterwards reflected on the camera by a dichroitic mirror. Notably, only the emission light is reflected as a dichroitic mirror is selective in wavelength. Exposing the specimen only to low excitation intensities, this technique reduces photobleaching and damages to the sample. Advantageously, the optical axis of the system is constant during the entire measurement wherefore images can directly be captured [44]. The sdCLSM uses a highly efficient camera instead of a photomultiplier detector like conventional confocal microscopes.

A sdCLSM developed by Olympus is used in the scope of this work. The setup comprises two cameras (Andor iXon Ultra 897) with a pixel size of 266.667 nm with a LUMPLFLN W 60x / 1,00 submersion objective to detect two different emission wavelength simultaneously. The excitation wavelengths are are set to $\lambda_{ex} = 488\,\text{nm}$ and 561 nm whereas the emission wavelengths are $\lambda_{em} = 508\,\text{nm}$ and 585 nm, respectively for myosinII-GFP and mRFPmars-LimΔcoil. If not mentioned differently, a LUMPLFLN W 60x / 1,00 submersion objective is used to image the cellular migration of *D.d.* cells in phosphate buffer. The field of view, defined by both the numerical aperture of the objective and the array size of pinholes, is 116.5 µm × 107.7 µm.

3.3 3D Printing

3.3.1 General Workflow from Design to Print

Since we want to investigate cellular motion under more realistic environmental conditions, we expose D. d. cells to anisotropic curved surfaces. To quantify the effect of the surface curvature on the directionality of cellular motion, we produce well-defined surface structures with defined curvatures. Here, the surfaces are sinusoidally shaped to approach the environmental conditions that cells in nature are exposed to. According to section 2.5, research was frequently focused on sharp structures like sawteeth or ridges. Similar to [30, 45, 29], smooth structures are designed on microscales with varying curvatures.

For the beginning, we design sinusoidal structures comparable to planar waves as described in eq. (3.5)

$$h(x, y) = A \cdot \sin^2(n\pi \cdot x) + a \ , \tag{3.5}$$

where $h(x, y) = h(x)$ is the height profile as a function of distance x, A is the amplitude, and n the number of wave maxima within the entire x-range. The constant offset a is added in order to stabilize the printed structure on the glass substrate. Then, we create an outer volume matrix of zeros and embed an inner volume of ones being restricted to the surface function $h(x, y)$ at the top. Importantly, the boundary of the inner volume must not be part of the boundary of the outer volume. Subsequently, we used the `isosurface` function of Matlab ® (R2017a, MathWorks) to create a set of vertices and faces. To get an STL-file as an output-file which can be used for further processing, this set of vertices and faces is plugged into the `stlwrite` function (Copyright © 2015, Sven Holcombe). Importing the STL-file to MeshLab [46], the surfaces of the design can be faired, e.g., by means of Taubin smoothing (section 4.2.2). After that, the STL-file is imported by DeScribe (developed by Nanoscribe). DeScribe is an editing software for GWL-files and converts 3D designs in GWL-format being required by the Photonic Professional (GT) respectively the control software NanoWrite of the 3D printer.

At first, the objective being used later for the print as well as the appropriate photoresist has to be chosen. Here, the IP-S, a highly viscous photoresist, in combination with a 25x objective (ZEISS 25x/ 0,8 DIC Imm Korr LCI Plan-NEOFLUAR) and an ITO-coated DiLL glass substrate (size 25 mm × 25 mm; thickness 0.7 mm; optical transparent; provided by NanoScribe) is used. The voxel size in this configuration ranges from $\approx 0.4\,\mu\text{m} - 1\,\mu\text{m}$ ($\approx 0.15\,\mu\text{m} - 0.5\,\mu\text{m}$ for a 63x objective) depending on vicinity effects. Second, the absolute size (here in μm) has to be set. Since the field of view of the

60x objective (Olynmpus LUMPLFLN W 60x / 1,00) used in the sdCLSM setup is 116.5 µm × 107.7 µm, it is favorable to chose the absolute structure size larger than the field of view of the microscope for experimentally reasons. As the software converts the entire volume of the 3D design in a set of trajectories, slicing and hatching distances have to be determined in µm. The slicing distance is a measure for the distance between two layers whereas the hatching distance determines the distance between two adjacent trajectories in the same plane. There are, on the one hand, the adaptive slicing mode and, on the other hand, the fixed slicing mode. In this work, the latter one is chosen to keep the slicing distance constant. With regard to the fill mode, the solid one is chosen as the orders of magnitude of the current structures are small enough so that the print is finished in a reasonable time. In addition, simplification tolerance and the contour count have to be set. The simplification tolerance is chosen to 0 as an exact reproduction of the 3D structure is favorable. The contour count is a parameter for the number of contour lines being spatially separated by the contour distance. Furthermore, both the slicing and hatching distance are kept small so that the overlap of the laser voxel is quite high, ensuring a smooth surface.

At last, the scan modes in X-Y-direction and Z-direction have to be determined. To fasten up the print, the `GalvoScanMode` in X-Y-direction is chosen. Contrarily, the Z-axis is scanned in the `PiezoScanMode` in order to guarantee a smooth surface of the print by keeping a high overlap of the laser voxel lines. As the printing configuration is "DiLL", the correct setting for Z-Direction is `Upwards (+Z)`. Since the structure sizes here are covered by the range of the galvanometer, splitting is not needed.

Before printing, glass substrates are cleaned. To ensure high adhesion strength of the print, the glass substrates are immersed into an acetone bath for at least 30 min. Afterwards, they are rinsed with IPA and dried with nitrogen. Using the ITO-coated glass substrates, the ITO-coated side has to face upwards while fixing the substrate to the foreseen holder with tape. It is advantageous to measure the resistance of both sides because the ITO coated side is electroconductive. Subsequently, a droplet of the IP-S photoresist is casted on the ITO-coated side of the substrate. Importantly, the interface finder of the printer has to detect a sufficiently high intensity of reflected light in order to find the interface. Therefore, the difference of refractive indices has to fulfill the relation $\Delta n = n_{substrate} - n_{resist} > 0.05$ at a wavelength of 830 nm so that reflection is strong enough.

Then, the NanoWrite software has to be started. After stage calibration and loading the 25x objective to the setup, the substrate holder is mounted to the printer. Before loading and starting the print job, the objective approaches to the interface ITO/IP-S.

After printing, the sample holder has to be removed from the 3D printer. Preventing the print from damage, it is recommendable to put the samples vertically in the sample

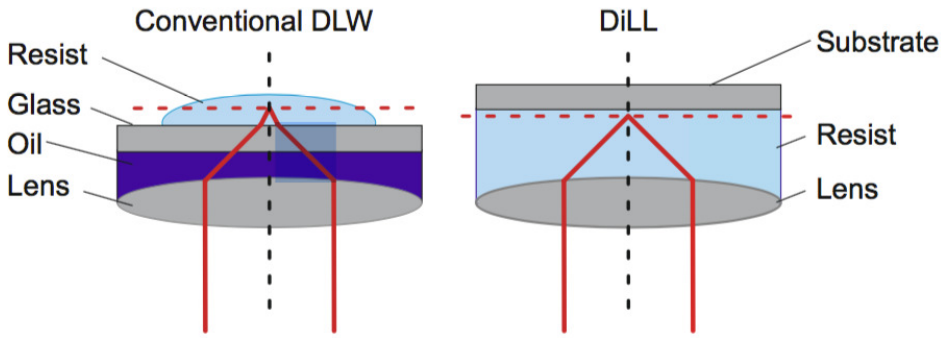

(a) Oil immersion configuration (left) and Dip-in Laser Lithography (right). From [47].

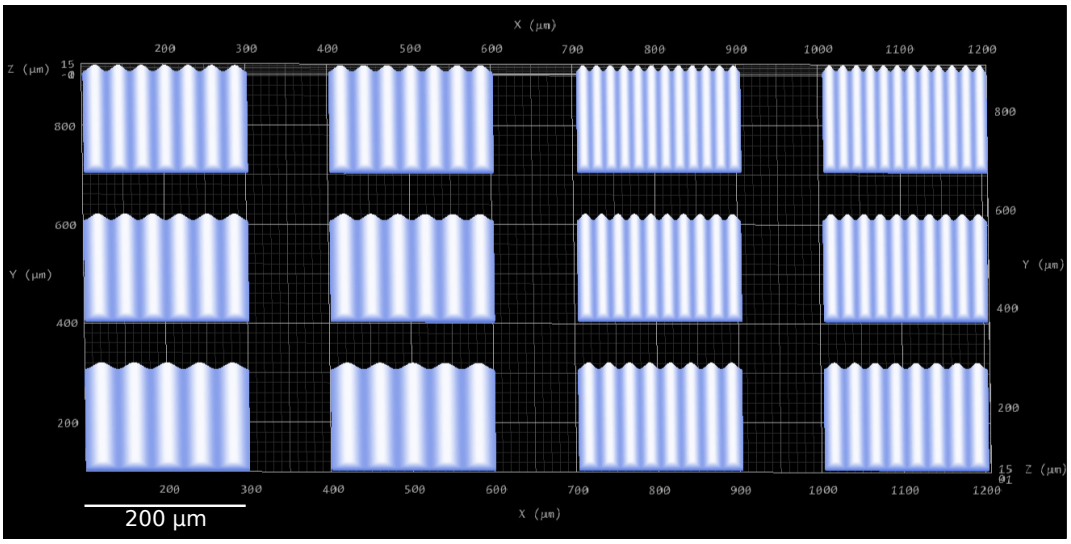

(b) Screenshot from DeScribe showing designed surfaces arranged in an array-like structure with N_{wm} = 5, 6, 7, 8, 10 and 12 wave maxima, corresponding half wavelengths $\lambda/2 = 40.00\,\mu m$, $33.33\,\mu m$, $28.57\,\mu m$, $25.00\,\mu m$, $20.00\,\mu m$ and $16.67\,\mu m$ and an amplitude of $A = 10\,\mu m$.

Figure 3.8: Printing configurations and structure design. The sinusoidal waves are printed in the DiLL configuration. **(a)** In Dip-in Laser Lithography configuration (DiLL), the objective is directly dipped into the photoresist. Advantageously, not only the spherical aberrations are minimized but also the printing range in z-direction is not limited by the refraction at the interface(s). In conventional DLW, the spherical aberration depends strongly on the distance from the focal plane to the interface between glass and resist. **(b)** Screenshot from DeScribe showing designed surfaces that are coated with PDMS. Thus, they represent the negative surface structure used during the 3D tracking over time of D.d. cell migration.

Parameter	Setting
Objective and substrate	MesoScale (25x, IP-S, ITO)
Slicing distance	$0.1\,\mu m - 0.3\,\mu m$
Hatching distance	$0.1\,\mu m - 0.3\,\mu m$
Contour count	$1 - 3$
Contour distance	$0.1\,\mu m - 0.5\,\mu m$
Laser Power	$38\,\% - 50\,\%$

Table 3.2: Parameter ranges for DeScribe settings.

holder. Next, the prints have to be developed including a bath in a 25 mL beaker filled with PGMEA for 30 min and in a second 25 mL beaker filled with IPA for 2 min. In the end, the sample is carefully dried with nitrogen. For further information the reader is referred to [47].

3.3.2 Two Photon Polymerization and Photoresist IP-S

There are mainly two types of photoresists - negative or positive tone photoresists [48]. Positive tone photoresists usually consist of long polymeric chains decaying into shorter pieces when they are exposed to two photons. Then, the shorter pieces can be dissolved by the developer. On the contrary, unpolymerized monomers are washed away in negative tone photoresists while the polymerized long chains are not dissolved by the developer. In this work, the negative tone photoresist IP-S from Nanoscribe is used. It is highly viscous, produces smooth surfaces and structures with high stability.

3D printing with the Photonic Professional (GT) is based on two-photon polymerization. The principle behind is the two-photon excitation activating chemicals [49]. Especially, it is beneficial that the excitation is confined to a tiny volume providing a high spatial resolution due to quadratic dependence of two-photon absorption probability p on intensity I.

$$p \propto I^2 \tag{3.6}$$

Therefore, the absorption is confined to a volume which is in the order of magnitude of λ^3 due to coincidence where λ represents the wavelength of the exciting laser light. Thus, the volume of excitation (and polymerization) of the photoresist is confined to such a small volume.

Absorption does not only depend on the coincidence of two photons but also on the absorption cross-section δ. Photoresists basically consist of monomers which comprise

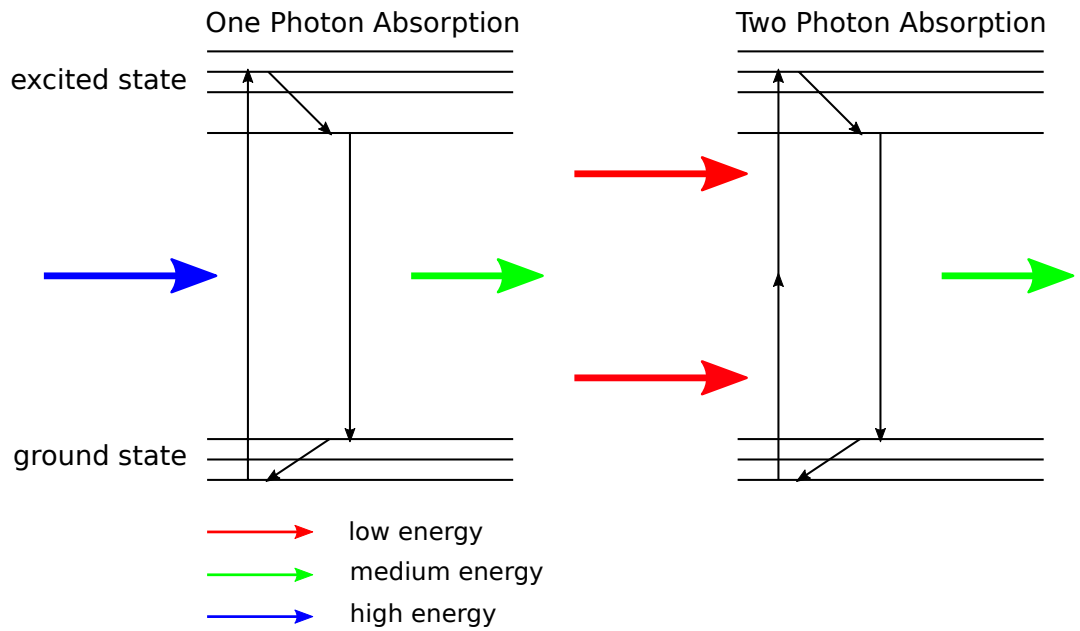

Figure 3.9: One photon absorption (left) and two photon absorption (right). If an electron is excited by absorbing a photon, the electron transitions into a higher, unstable energy state. Then, the electron transistions into a meta stable energy state without radiating, and subsequently to the ground state emitting a photon (of higher wavelength; fluorescence) and heat (or another photon with even longer wavelength). If the energy gap of ground state and excited state is $2h\nu$, two photons have to excite the electron coincidently wherefore the atomic transistion rate is weaker compared to one photon absorption.

subunits being chemically compounded via so called π-conjugated compounds. Typical structures of such molecules are D$-\pi-$D, D$-\pi-$A$-\pi-$D and A$-\pi-$D$-\pi-$A where A is an acceptor, D a donor, and π a π-conjugated bridge. The length of the $\pi-$bridge or the acceptor and donor strength can be increased in order to increase δ. This leads to higher delocalization of the electrons meaning that the excitation energy of electrons decreases. Since the D$-\pi-$D molecules are electron-rich, two-photon excitation leads to electron transfer towards acceptor molecules and thus activates polymerization.

3.4 Curvotatic Setup

Since the polymerized photoresist is highly auto-fluorescent, as shown in Fig. 3.10, cells cannot be imaged. For this reason, we use the 3D print as a negative and pour polydimethylsiloxane (PDMS) onto the structure. In general, the entire work flow starts with the mixing of the polymer. For this purpose, PDMS and the cross-linker (Sylgard 184, Th. Geyer) are mixed in a mass ratio 10:1 under the fume hood. Before the negative is placed in the plastic shell with the structure facing upwards, a small amount of the polymer is added to a plastic shell so that just the bottom is coated in order to avoid bubbles in the PDMS after baking. Afterwards, additional PDMS is dropped on the wafer. Then, the plastic shell with the PDMS and the wafer has to be put into the exicatore in order to get rid of the air bubbles in vacuum. After that, the PDMS is baked in the oven (from Memmert GmbH + Co. KG) at a temperature of 75 °C for approximately 45 min. Once it has cured and cooled down, the PDMS is cut with a razor blade and removed carefully from the wafer. Finally, the PDMS, as well as an Ibidi bottom glass substrate (ibidi GmbH), are treated with a plasma cleaner provided by Harrick Plasma to clean and to oxidize the surfaces. Thus, the PDMS sticks well to the substrate after treatment.

After building up the device, it is added to the optical setup and *D.d.* cells are pipetted onto the sinusoidal wave structures. With the help of the sdCLSM, the cells are tracked in 3D over time to observe their amoeboid motion (Fig. 3.10b). The related parameter settings are presented in Tab. 3.3.

Parameter	Value
exposure time	75 ms-100 ms
acquisition time	351 ms-376 ms
z-Step	0.8 µm-1.5 µm
time interval	30 s
number of slices	15-25

Table 3.3: Parameter ranges for 3D tracks of motile *D.d.* cells on sinusoidal wave structures.

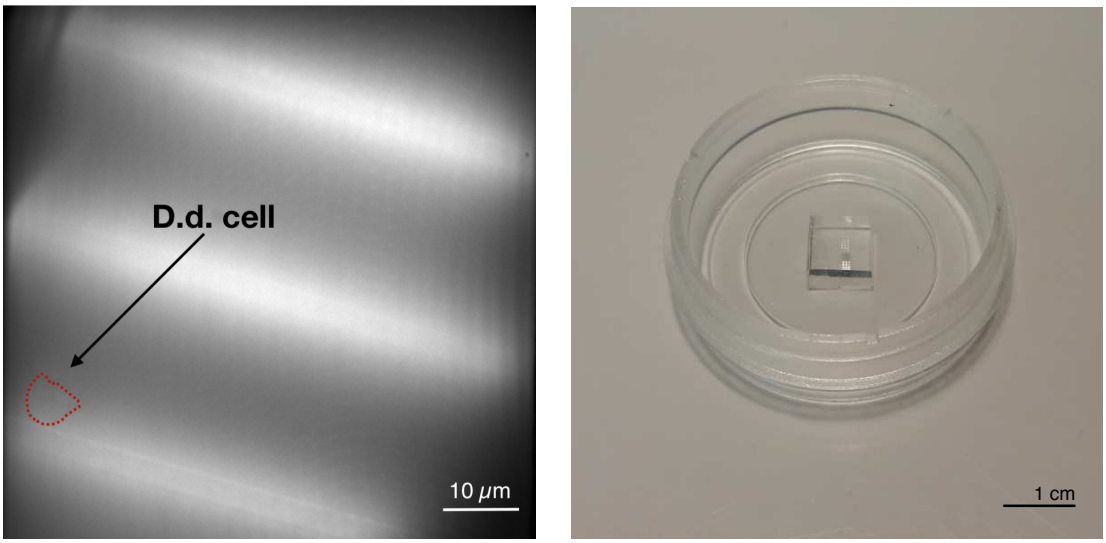

(a) Printed structure showing auto-fluorescence.

(b) PDMS block on Ibidi bottom glass substrate.

Figure 3.10: Printed structure showing high auto-fluorescence (left). The intensity of the background strongly exceeds the intensity of fluorescent labeled *D.d.* cells (Ax2 mRFPmars-Lim+myosinII-GFP). PDMS block with sinusoidal wave structures in the middle on Ibidi bottom glass substrates (right).

4 Results

4.1 Analysis Methods

For the purpose of analyzing the acquired in force-retraction experiments and on 3D cell tracking over time, the probability density functions of the data, as well as the sample distributions, are examined first. Therefore, a short overview of (central) moments is given in the section 4.1.1.

4.1.1 Characteristics of a Probability Density Function

In statistics, moments describe characteristics of probability density functions (PDF) obtained from the sample distributions of a measured parameter [50]. In this work, the data analysis is mainly focused on the mean value, variance, skewness and kurtosis. In general,

$$\mu_n = \int_{-\infty}^{\infty} \mathrm{d}x f(x)(x-c)^n \,, \tag{4.1}$$

defines the n-th moment, where $f(x)$ is the PDF of the real variable x, c is a constant value and the definition usually refers to $c = 0$. If c equals the mean value of $f(x)$, then μ_n is called the n-th central moment. Notably, the PDF is normalized so that

$$\int_{-\infty}^{\infty} \mathrm{d}x f(x) = 1 \,. \tag{4.2}$$

The first moment ($n = 1$) is known as the **mean value** and described by

$$\mu = \langle X \rangle = \int_{-\infty}^{\infty} \mathrm{d}x f(x) x \,, \tag{4.3}$$

with $c = 0$ whereas the second moment, the **variance**, is defined by

$$\sigma^2 = \left\langle (X - \mu)^2 \right\rangle \ , \tag{4.4}$$

$$= \int_{-\infty}^{\infty} \mathrm{d}x f(x)(x - \mu)^2 \ , \tag{4.5}$$

$$= \left\langle X^2 \right\rangle - \mu^2 \ . \tag{4.6}$$

σ^2 is a non-negative measure for the deviation of the data from the mean value of the distribution. Both the mean value and variance are not normalized, thus not dimensionless, in contrast to skewness as well as kurtosis. **Skewness** is a measure for the asymmetry of a distribution around its mean and is defined by

$$s = \frac{\mu_3}{\sigma^3} = \frac{\left\langle (X - \mu)^3 \right\rangle}{\left(\langle X^2 \rangle - \mu^2 \right)^{3/2}} \ . \tag{4.7}$$

If the skewness s is negative, the distribution has a longer tail on the left side ($X < \langle X \rangle$) wherefore it is also called left-tailed. Accordingly, if $s > 0$, the distribution has a longer tail on its right side and is called right-tailed. According to [51], the standard deviation of the skewness of a normal distribution is $\sqrt{15/N}$ wherefore the distribution is regarded as skewed if $s \gg \sqrt{15/N}$.

The **kurtosis** is the fourth central moment normalized by the variance squared, namely

$$k = \frac{\mu_4}{\sigma^4} = \frac{\left\langle (X - \mu)^4 \right\rangle}{\left(\langle X^2 \rangle - \mu^2 \right)^2} \ . \tag{4.8}$$

k measures the outliers of a distribution which is an indicator for the "tailness". Data within one standard deviation (σ) about the mean, hence, in the region of the mean, only contribute weakly to k. On the opposite, the contribution of data outside the region of the peak is much higher. In case of a normal distribution, the standard deviation amounts to $\sqrt{96/N}$. Thus, a variable is only not considered as normally distributed if k is significantly larger than $\sqrt{96/N}$ ([51]).

Experimental data provide a sample X_i with n measurement values $(x_1, \ldots, x_n)$ wherefore the mean value of the samples $\bar{X}$ is only an estimator for the real mean value μ of the underlying distribution of the variable X.

$$\bar{X} = \frac{1}{n} \sum_{i=1}^{n} X_i \ . \tag{4.9}$$

Notably, the real mean value μ is not (*a priori*) exactly known so that the variance has

to be estimated, too, by $\bar{\sigma}$ of the data being defined as

$$\bar{\sigma}^2 = \frac{1}{n-1} \sum_{i=1}^{n} \left(X_i - \bar{X}\right)^2 \ . \tag{4.10}$$

For further details on the derivation of the above equations, the interested reader is referred to [51]. In the following, σ^2 refers always to eq. (4.10).

4.2 Sinusoidal Surfaces

Before tracking *D.d.* cells on the curved surfaces over time and before performing single cell force spectroscopy, the roughness and global structure of the printed substrates have to be determined. The data were converted to txt-files with the help of Gwyddion [52].

4.2.1 Sinusoidal Surfaces Without Surface Fairing

According to the surface profile function $h(x, y)$ (eq. (3.5)), the profile data acquired with the help of the AFM scan is fitted line-by-line with the fit function

$$f(x, y) = f(x) = a_1 \cdot \sin^2 \left(a_2 \cdot (x - a_3)\right) \tag{4.11}$$

$$= \frac{a_1}{2} \cdot \left(1 - \cos \left(a_2 \cdot (x - a_3)\right)\right) \ . \tag{4.12}$$

Figure 4.1 shows a $20.08\,\mu m \times 20.08\,\mu m$ scan of a structure (Fig. 4.1a) with an amplitude of $A = 10\,\mu m$, a wavelength of $\lambda/2 = 25\,\mu m$ and $N_{wm} = 4$ wave maxima (Fig. 4.2) as well as a profile line (Fig. 4.1b). The asymmetry is probably due to the scan direction where I- and P-gain could only be well tuned for one direction. Figures 4.1c and 4.1d depict the roughness of the surface scan, being defined as the deviation of the fit $f(x)$ from the original data set $s(x, y)$

$$\rho(x, y) = |f(x, y) - s(x, y)| \ . \tag{4.13}$$

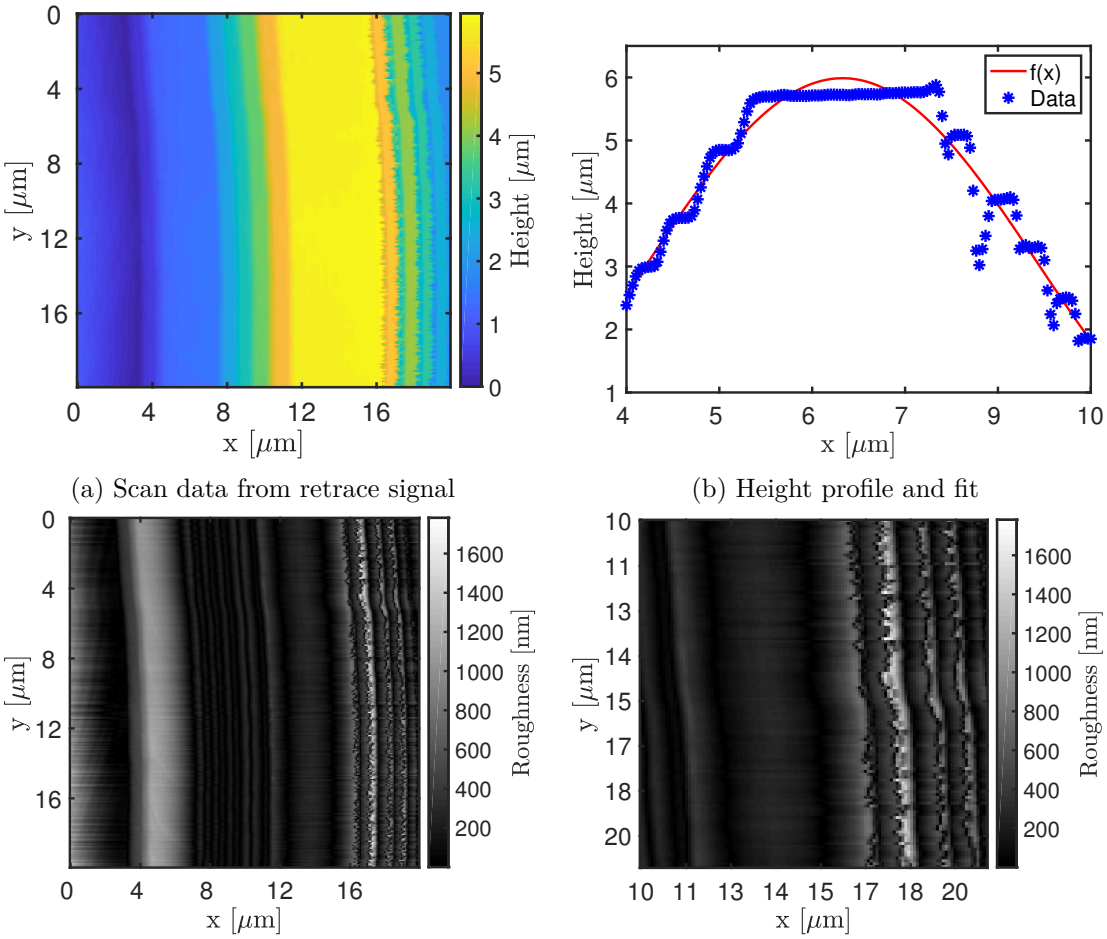

(a) Scan data from retrace signal

(b) Height profile and fit

(c) Roughness

(d) Roughness zoom

Figure 4.1: Scan and analysis of sinusoidal surface structure with an amplitude of $A = 10\,\mu m$, a wavelength of $\lambda/2 = 25\,\mu m$ and $N_{wm} = 4$ wave maxima without Taubin smoothing. **(a)**: Topography data acquired via surface scanning in contact mode with AFM. **(b)**: Fit of height profile across the wave according to eq. (4.11). **(c)**, **(d)**: Roughness of the structure computed according to eq. (4.13).

Both figures reveal that the width of a step is $\approx 1\,\mu m$ while the height differs from $0.5\,\mu m - 1\,\mu m$. Considering the ability of *D.d.* cells to sense nanotopographic structures as explained in section 2.5, it is necessary to smoothen the surfaces in order to ensure that contact guidance due to nanoscale influences does not interfere during the experiment.

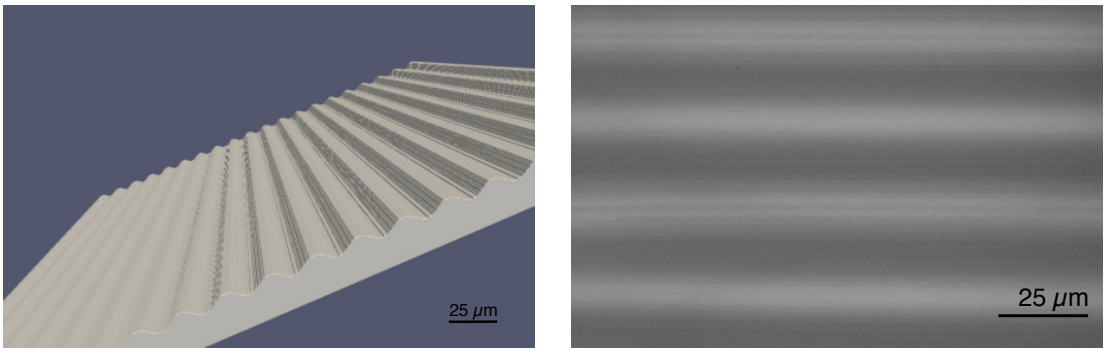

(a) ParaView screenshot. (b) Section of the bright field image.

Figure 4.2: Steps on the "sinusoidal" surface of faces and vertices of the 3D designs without surface smoothing. **(a)** Screenshot from ParaView of the step-containing 3D design with $N_{wm} = 20$ wave maxima and $A = 10\,\mu\text{m}$. The steps have to be eliminated to ensure that cells crawl on smooth sinusoidal-shaped surfaces.

Furthermore, it is not possible to image the entire amplitude because the amplitude is too high ($A = 10\,\mu\text{m}, \lambda/2 = 25\,\mu\text{m}$) in comparison to the length of the MLCT cantilever tip and overall geometry (presented in Fig. 3.4). In consequence, if the fit range does not comprise the whole amplitude, the fit will not represent the whole structure, too.

4.2.2 Taubin Surface Smoothing

One solution to remove the steps on the surface of the printed structures 4.2.1 is applying surface smoothing algorithms [53, 54] to the structure consisting of faces and vertices created by the `isosurface` function of Matlab®. Among those, the algorithm presented by G. Taubin in [53] provides a mean to fair surfaces depending only linearly on time and space. Additionally, the algorithm preserves exactly the number of vertices and faces of the original design. In principle, it applies a low-pass filter algorithm to the polygonal surface being considered as discrete surface signals.

Analogously to noise removal in signal processing, Taubin applies a low-pass filter to closed surfaces in order to smooth them. G. Taubin identifies the classical Fourier transform of a signal with the decomposition of the signal into a linear combination of the eigenvectors of the Laplacian operator [53]. Let $x = (x_1, \ldots, x_n)^t$ be a discrete signal in time defined on n vertices v_i of a polygon. Then, a vertex pair v_i and v_j is in the first order neighborhood if both vertices share a common face or, more formally, if j is in the neighborhood $i^\star$ of the vertex v_i. Hence, the neighborhood is symmetric if

$j \in i^\star \wedge i \in j^\star$.Taubin defines the weighted discrete Laplacian of a discrete surface by

$$\Delta x_i = \sum_{j \in i^\star} w_{ij}(x_j - x_i) \ , \tag{4.14}$$

where $\sum_{j \in i^\star} w_{ij} = 1$ and $w_{ij} > 0$ for each i. In matrix representation, eq. (4.14) reads

$$\Delta x = -Kx \ , \tag{4.15}$$

where K is symmetric and has real eigenvectors u_i, eigenvalues k_i and $i \in \{1, \ldots, n\}$. Thus, the signal x can be written in Eigen-basis as

$$x = \sum_{i=1}^{n} \xi_i u_i \ , \tag{4.16}$$

where the eigenvectors u_i of the matrix K are considered as natural vibration modes and the eigenvalues k_i as natural frequencies. Together with the matrix of weights $W = (w_{ij})$ with $w_{ij} = 0$, if $j \notin i^\star$, matrix K can be defined by $K = I - W$. In order to remove noise from the surface signal x, Taubin projects the frequency space onto a sub-space of low frequencies. Then,

$$x' = f(K)x = \sum_{i=1}^{n} \xi_i f(k_i) u_i \ , \tag{4.17}$$

where $f(K)$ is the transfer function. A low-pass filter has to fulfill the conditions $\lim\limits_{N \to \infty} f^N(k_i) \approx 1$ for low frequencies and $\lim\limits_{N \to \infty} f^N(k_i) \approx 0$ for high frequencies after N iterations in the region of interest. Since Gaussian smoothing leads to shrinkage, Taubin has chosen $f(k)$ as

$$f(k) = (1 - \lambda k) \cdot (1 - \mu k) \ , \tag{4.18}$$

where $\lambda > 0$ is a shrink factor and $\mu < -\lambda$ an un-shrink factor. The first factor in eq. (4.18) represents the Gaussian smoothing leading to shrinkage whereas the second factor performs the un-shrinking step. The factors originate from integration of the Laplace eq. (4.15) with the Euler method [55].

4.2.3 Surface Smoothing is beneficial

With the objective to elucidate contact guidance on sinusoidal wave structures properly without systematic nanotopographical perturbations (see section 2.5), the surfaces of the designed structures are smoothed with the help of the Taubin algorithm. The parameters were chosen to $\lambda = 0.99$, $\mu = -0.65$ and 100 iterations (see section 3.3). Figure 4.3 shows an overview of the entire array of the smoothed surfaces comprising sinusoidal structures with wavelengths $\lambda/2 = 40.00\,\mu m$, $33.33\,\mu m$, $28.57\,\mu m$, $25.00\,\mu m$, $20.00\,\mu m$ and $16.67\,\mu m$. The image was acquired by bright field microscopy and each structure measures $200\,\mu m \times 200\,\mu m$.

The surface of each structure is imaged by AFM scanning. The structure with $\lambda/2 = 28.57\,\mu m$ for amplitudes of $A = 5\,\mu m$ and $10\,\mu m$ together with structural analysis are shown in Fig. 4.4 and 4.5. The bright field images shown in Fig. 4.4a and Fig. 4.5a, as well as in the surface scans depicted by Fig. 4.4b and Fig. 4.5b, reveal smooth sinusoidal-shaped wave structures. These surfaces are fitted line by line with the eq. (4.11). Compared to the surface in Fig. 4.1 which was not previously smoothed, the fit function represents the surface data reasonably in the region of a single maximum in combination with the appropriate fit parameters (Fig. 4.4c and Fig. 4.5c). There is only a slight deviation at the boundary of the fit which results from low differences in the absolute hight in the two neighbored minima as exemplarily depicted in Figs. 4.4c and 4.4d. Probably, this is a consequence of Taubin smoothing and, therefore, appears especially at the boundaries of the structure. Since *D.d.* cells are mainly tracked sufficiently far away from the border, this small perturbation is neglected in further analysis. Thus, the surface is assumed to be ideal and represented perfectly by the fit function $f(x, y)$. The fit is performed using the Matlab® function `lsqcurvefit` [56]. The initial guesses of the fit parameters of the function $f(x, y)$ are shown in table 6.1.

Then, the roughness, defined in eq. (4.13), is plotted for the entire scan size pictured in Fig. 4.4d and Fig. 4.5d. Importantly, the large deviation in Fig. 4.5d results from the artifacts explained in the previous section 4.2.1 due to cantilever tip geometry. The regions of interest are shown in Figs. 4.4f and 4.5f. They are cut out from Figs. 4.4e and 4.5e where the fit reasonably represented the surface scan, *i.e.* in the area close to a maximum of the sinusoidal wavy height profile. These regions are chosen to calculate the root mean square roughness $\bar{\rho}$

$$\bar{\rho} :- \sqrt{\frac{1}{N}\sum_{i=1}^{N}\rho^2}\,. \tag{4.19}$$

Here, N represents the number of pixels. Noteworthily, the root mean square roughness

is usually a measure for quadratic deviation from a mean value given by the fit function $f(x, y)$.

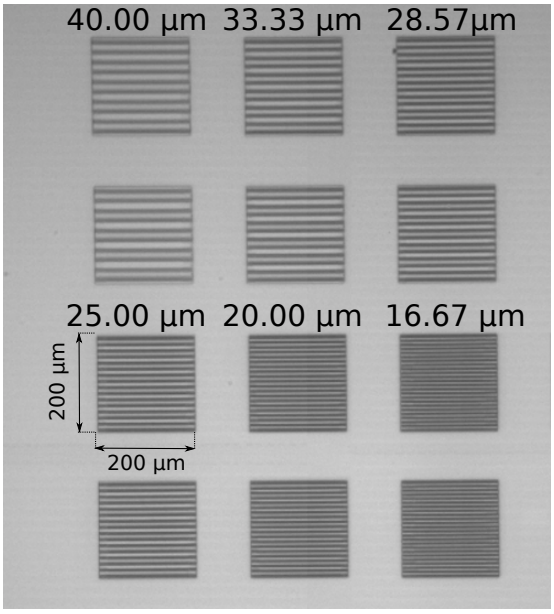

Figure 4.3: Bright field image of the entire array including always two structures with 5, 6, 7, 8, 10 and 12 wave maxima with an amplitude of $A = 10\,\mu m$. One structure measures $200\,\mu m \times 200\,\mu m$. Therefore, the wavelengths amount to $\lambda/2 = 40.00\,\mu m$, $33.33\,\mu m$, $28.57\,\mu m$, $25.00\,\mu m$, $20.00\,\mu m$ and $16.67\,\mu m$, respectively.

The results are shown in table 4.1 indicating a root mean square roughness $\bar{\rho} \leq 100\,nm$ for every structure except for the structure with $A = 10\,\mu m$ and $\lambda/2 = 33.33\,\mu m$ where $\bar{\rho} = (177.91 \pm 11.79)\,nm$. Notably, the number of iterations of the Taubin smoothing step was only 10 instead of 100 indicating that the surface roughness decreases as a function of the number of iterations.

The roughness estimation is probably quite generous as it also takes into account dust on the surface or cantilever fluctuations. Additionally, the scan could be fitted with a polynom of n-th degree representing the texture even more precisely. However, the surface of the sinusoidal wave structures appears smooth enough to exclude significant nanotopographic influences on contact guidance mediated by the microscaled sinusoidal wavy topographies.

Since the amoeboid cell migration will be investigated as a function of surface curvature,

N_{wm}	$\lambda/2$ [µm]	$\bar{\rho}$ [nm]	R [µm]
5	40.00	28.53 ± 2.57	16.18
6	33.33	88.58 ± 5.77	11.24
7	28.57	83.27 ± 3.81	8.29
8	25.00	56.68 ± 2.06	6.33
10	20.00	51.68 ± 1.67	4.05
12	16.67	97.41 ± 15.26	2.82

(a) $A = 5\,\mu\text{m}$

N_{wm}	$\lambda/2$ [µm]	$\bar{\rho}$ [nm]	R [µm]
5	40.00	60.54 ± 2.40	8.09
6	33.33	177.91 ± 11.79	5.62
7	28.57	23.79 ± 4.46	4.13
8	25.00	43.58 ± 13.78	3.16
10	20.00	49.54 ± 3.09	2.03
12	16.67	53.85 ± 6.80	1.41

(b) $A = 10\,\mu\text{m}$

Table 4.1: Half wavelength $\lambda/2$ of the structure, corresponding root mean square roughness $\bar{\rho}$ of zoomed region (eq. (4.19)) and radius of maximal curvature R (eq. (4.21)) for substrates with an amplitude of **(a)** $A = 5\,\mu\text{m}$ and **(b)** $A = 10\,\mu\text{m}$. The error is estimated by standard deviation from the mean value.

this parameter is evaluated, too. Curvature $C(x, y) = C(x)$ is defined as follows

$$C(x) :- \frac{f''(x)}{(1 + (f'(x))^2)^{3/2}} , \tag{4.20}$$

where f' (f'') denote the first (second) derivative of the fit function $f(x, y) = f(x)$. The reason for computing $C(x)$ in dependence on the (smooth) fit function is that the data are slightly noisy which is even amplified in the derivatives. Then, the local radius of curvature can be easily calculated with

$$R(x) :- \frac{1}{C(x)} . \tag{4.21}$$

For completeness, the first and second derivative of $f(x)$ (eq. (4.11)) are given by

$$f'(x) = 2a_1a_2 \cdot \sin\left(B \cdot (x - a_3)\right) \cdot \cos\left(a_2 \cdot (x - a_3)\right) , \tag{4.22}$$

$$= a_1a_2 \cdot \sin\left(2a_2 \cdot (x - a_3)\right) , \tag{4.23}$$

$$f''(x) = 2a_1a_2^2 \cdot \cos\left(2a_2 \cdot (x - a_3)\right) . \tag{4.24}$$

Exemplary, the results for $\lambda/2 = 28.57\,\mu\text{m}$, $A = 5\,\mu\text{m}$ and $10\,\mu\text{m}$ are shown in Figs. 4.4e and 4.5e. Naturally, the radius of curvature $R(x)$ diverges at locations where $f''(x) = 0 = C(x)$. The "minimal" radius of maximal curvature is located at positions where $f'(x) = 0$. It ranges from $1.41\,\mu\text{m} - 16.18\,\mu\text{m}$ for the sinusoidal wavy structures in this work (Tab. 4.1). Since these values stem from the fit of the scan data where the effective z range of the cantilever is not sufficient to scan also the valleys, the values for R base on the theoretically defined height function eq. (3.5) and are shown together with the roughness of the substrate in Tab. 4.1.

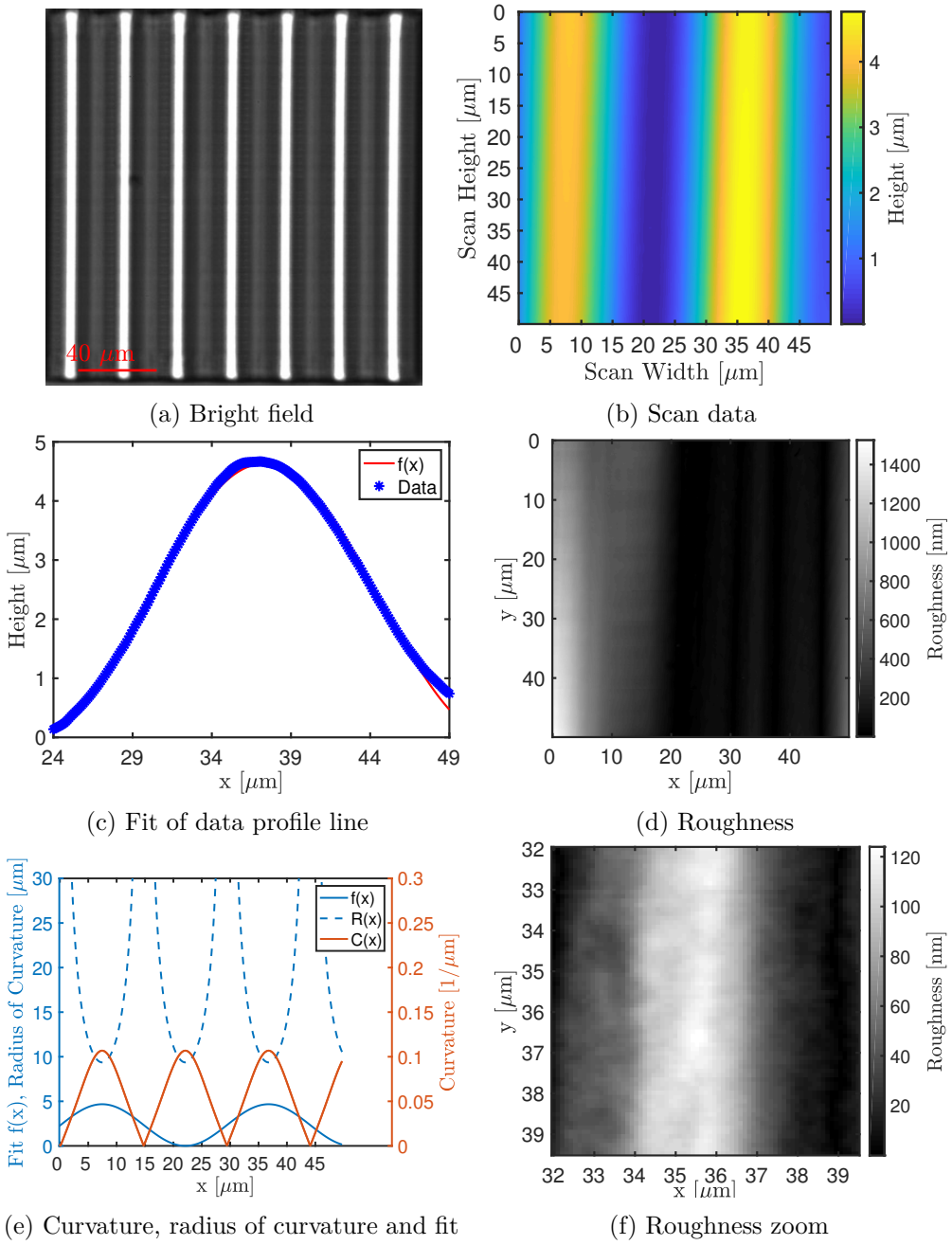

(a) Bright field

(b) Scan data

(c) Fit of data profile line

(d) Roughness

(e) Curvature, radius of curvature and fit

(f) Roughness zoom

Figure 4.4: Scan of sinusoidal surface with Taubin smoothing ($A = 5\,\mu\text{m}$, $\lambda/2 = 28.57\,\mu\text{m}$). **(a)** Bright field image of structure. **(b)** Topography data acquired via surface scanning in contact mode with AFM. **(c)** Fit of height profile across the wave according to eq. (4.11). **(d)**, **(f)** Roughness of the structure (eq. (4.13)). **(e)** Curvature and radius of curvature (eq. (4.20) and eq. (4.21)). The radius diverges at the zeros of curvature.

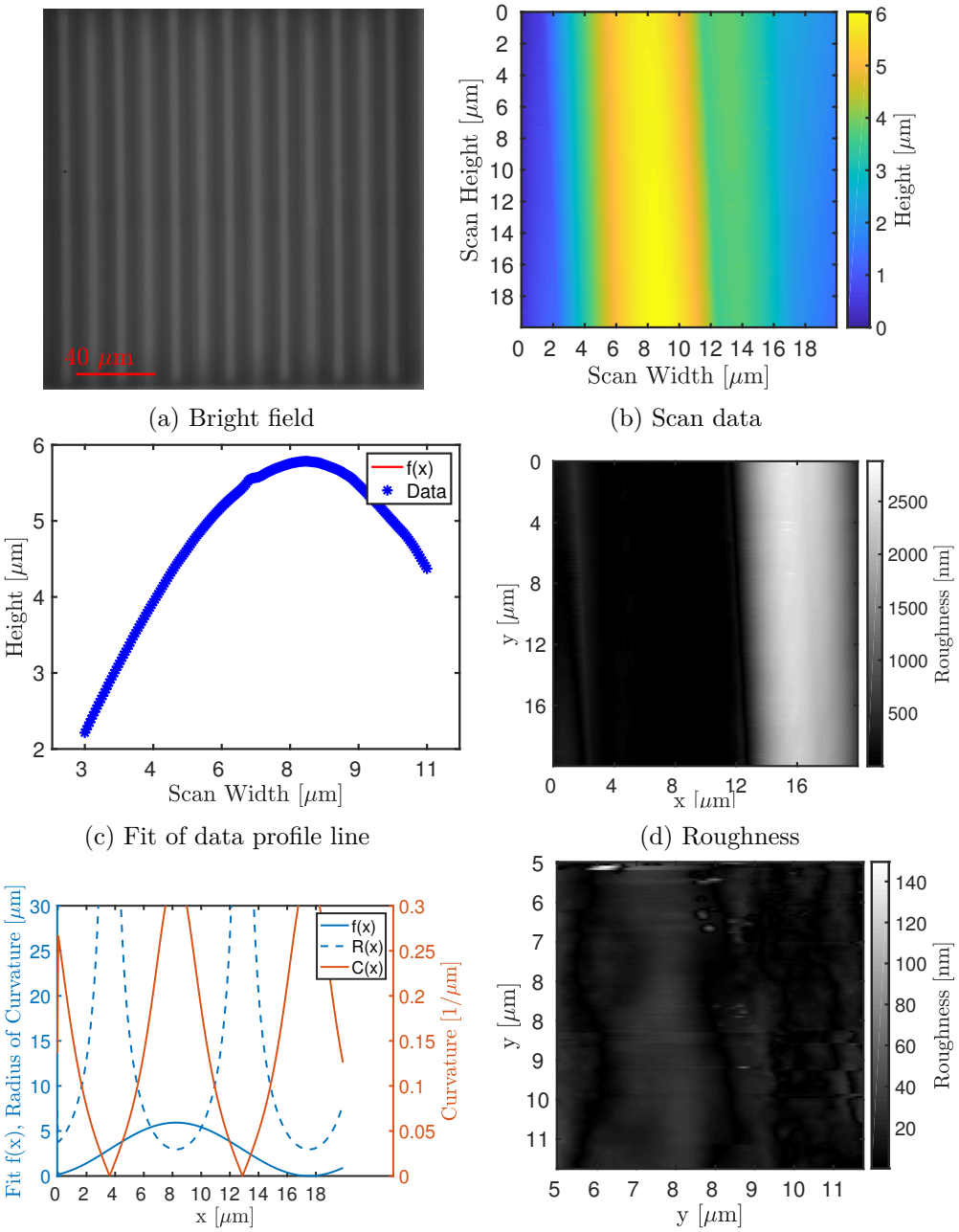

(a) Bright field

(b) Scan data

(c) Fit of data profile line

(d) Roughness

(e) Curvature, radius of curvature and fit

(f) Roughness zoom

Figure 4.5: Scan of sinusoidal surface with Taubin smoothing ($A = 10\,\mu m$, $\lambda/2 = 28.57\,\mu m$). **(a)** Bright field image of structure. **(b)** Topography data acquired via surface scanning in contact mode with AFM. **(c)** Fit of height profile across the wave according to eq. (4.11). **(d)**, **(f)** Roughness of the structure (eq. (4.13)). **(e)** Curvature and radius of curvature (eq. (4.20) and eq. (4.21)). The radius diverges at the zeros of curvature

4.3 Contact Guidance

Under laboratory conditions, amoeboid cell migration was most frequently investigated on flat surfaces. But in nature, *D.d.* cells usually face a geometrically complex environment. To examine the amoeboid migration under more realistic environmental conditions, we exposed the *D.d.* cells to sinusoidal surfaces as described above and acquire 3D data over time with a sdCLSM. The substrates reveal radii of maximal curvature ranging from 1.14 µm − 16.18 µm. The data are analyzed with the help of Imaris 8.3.1 © (Bitplane AG).

Image properties, such as pixel size, overall size of the field of view and time interval of each stack, have to be set. Then, the implemented function `Subtract Background` is applied to remove the background illumination. Afterwards, if necessary, the fluorescent signal can be linearly stretched with the implemented function `Linear Stretch`. After the pre-processing, the `Surface`-function recognizes the cellular volumes for each time step with the help of a marching cube algorithm [57] whereby it automatically calculates important parameters, such as the position of the center of homogeneous mass, straightness of the track, ellipticity (oblate and prolate) or volume for each time step. To guarantee statistical independent measurements, the results are taken from multiple measurements on several days (Tab. 4.2).

$\lambda/2$ [µm]	#days	# cells	# structure
40.00	4	24	4
33.33	4	25	5
28.57	4	27	4
25.00	4	23	4
20.00	4	25	4
16.67	4	30	3
∞	1	20	2

(a) $A = 5\,\mu m$

$\lambda/2$ [µm]	#days	# cells	# structure
40.00	4	24	5
33.33	4	24	4
28.57	4	33	6
25.00	4	25	4
20.00	1	25	2
16.67	1	25	2

(b) $A = 10\,\mu m$

Table 4.2: Statistics of experiments on 3D tracking over time on curved surfaces with amplitudes of $A = 5\,\mu m$ and $10\,\mu m$. The experimental data originate from different days and the *D.d.* cells on each structure were tracked several times so that a statistical independence can be assumed. The number of cells only considers moving cells on each structure.

From the position of the center of homogeneous mass $\vec{r} = (x, y, z)$ at the time t, we

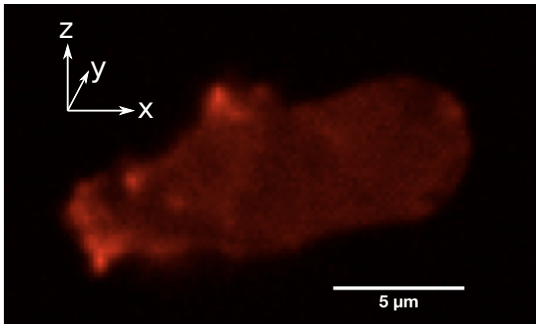

(a) 3D stack of a *D.d.* cell

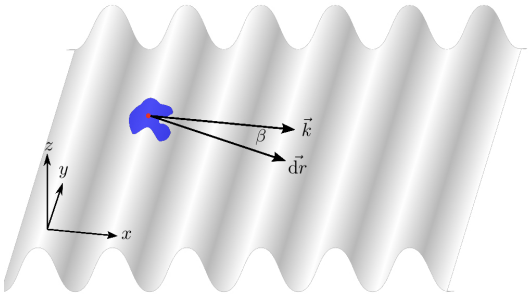

(b) Sketch of *D.d.* cell on sinusoidal wave structure.

Figure 4.6: A *D.d.* cell (blue) is crawling on a sinusoidal wave surface. The center of mass (red) is shifted by $\mathrm{d}\vec{r}$ between two subsequent time points whereby the migration angle β is a measure for the migration direction relative to the orientation of the waves defined by the wave vector $\vec{k}$.

calculate the displacement vector $\mathrm{d}\vec{r}$ by

$$\mathrm{d}\vec{r} = \vec{r}(t + \mathrm{d}t) - \vec{r}(t) \,, \tag{4.25}$$

where $\mathrm{d}t$ is the time interval of each stack. Then, the total length of each displacement $\mathrm{d}r_3$ as well as the projected displacement length over ground $\mathrm{d}r_2$ are given by

$$\mathrm{d}r_3 = \sqrt{\mathrm{d}x^2 + \mathrm{d}y^2 + \mathrm{d}z^2} \,, \tag{4.26}$$

$$\mathrm{d}r_2 = \sqrt{\mathrm{d}x^2 + \mathrm{d}y^2} \,. \tag{4.27}$$

From eq. (4.27), the mean velocity is directly obtained by

$$v_{2,3}(t) = \frac{\mathrm{d}r_{2,3}(t)}{T} \,, \tag{4.28}$$

where T is the time interval of the image acquisition. From eq. (4.27), we define the migration angle β for each time step by

$$\cos(\beta) = \left| \frac{\mathrm{d}x}{\mathrm{d}r_2} \right| \,, \tag{4.29}$$

where $\vec{k}$ the wave vector of the sinusoidal waves. Choose the coordinate system so that $\vec{k}$ points in x-direction. Due to the definition of β, the values range from $0° - 90°$.

In chemotactic cellular migration, the chemotactic index provides another parameter characterizing the cellular motion. Based on its definition, we define a curvotactic index for the z-projected motion as

$$CI = \left(\frac{\mathrm{d}x}{\mathrm{d}r_2}\right)^2 , \tag{4.30}$$

or analogously in 3D

$$CI_3 = \left(\frac{\mathrm{d}x}{\mathrm{d}r_3}\right)^2 . \tag{4.31}$$

If the migration is equally likely in x- and y- direction in 2D, *i.e.* β is distributed uniformly, then the CI is expected to be 0.5 in 2D. This can be derived from the expecting values of CI:

$$\langle CI\rangle = \left\langle \frac{\mathrm{d}x^2}{\mathrm{d}r_2^2}\right\rangle = \left\langle \cos^2(\beta)\right\rangle \overset{\mathrm{p}(\beta)=2/\pi}{=} \frac{1}{\pi/2}\int_0^{\pi/2}\cos^2(\beta)\,\mathrm{d}\beta = \frac{\pi/4}{\pi/2} = 1/2$$

In 3D, the behavior of CI_3 is slightly different. Without any special confinement, the entity of all possible migration directions is a sphere of radius R (total 3D step size) where every point on the sphere can be reached if $\beta \in [0, 2\pi)$ and $\gamma \in [0, \pi]$ yielding the boundaries of the related integrals (eq. (4.32)). Then, the expected value of the chemotactic index CI_3 is

$$\begin{aligned}\langle CI_3\rangle = \left\langle \frac{\mathrm{d}x^2}{\mathrm{d}r_3^2}\right\rangle &= \left\langle \frac{R^2\cos^2(\beta)}{R^2\cdot(1+\sin^2(\gamma))}\right\rangle \overset{\mathrm{p}(\beta)=1/2\pi,\ \mathrm{p}(\gamma)=1/\pi}{=} \frac{\frac{1}{2\pi}\int_0^{\pi/2}\cos^2(\beta)\,\mathrm{d}\beta}{1+\frac{1}{\pi}\int_0^{\pi}\sin^2(\gamma)\,\mathrm{d}\gamma} \\ &= \frac{1/2}{1+1/2} = 1/3\,. \end{aligned} \tag{4.32}$$

For analyzing the parameters of the shape, we use the prolate (e_P) obtained from Imaris statistics file. They are given by

$$e_P = \sqrt{1-\frac{a^2}{c^2}}\,, \tag{4.33}$$

$$\tag{4.34}$$

where a denotes the equatorial radius and c the polar radius of the prolate ellipsoid. Together with the definition of the volume of an ellipsoid $V = 4/3\pi a^2 c$, the polar radius

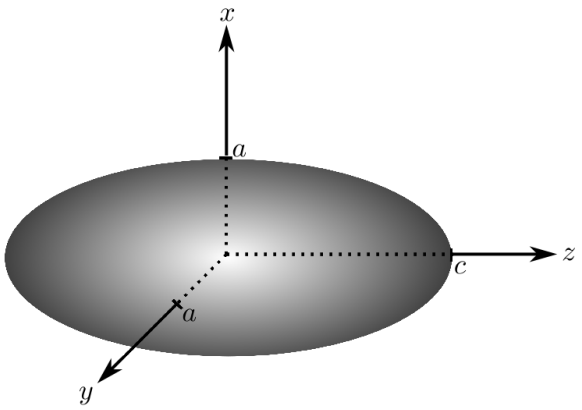

Figure 4.7: Prolate ellipsoid with equatorial radius a and polar radius c where $c > a$.

equatorial radius a of a prolate ellipsoid (Fig. 4.7) can be calculated by

$$a = \sqrt[6]{\frac{9V^2}{16\pi^2}(1 - e_P^2)} \,. \tag{4.35}$$

4.3.1 Thresholding

During migration on curved surfaces, *D.d.* cells alter between random and directed motility, as shown in Fig. 4.8. In this work, we are mainly interested in the direction and persistence of the cells' movement, hence, displacements of the center of mass due to shape changes of the cell are negligible. For this reason, the data from the 3D displacements (eq. (4.26)) have to be thresholded in order to take into account significant steps. Here, two different approaches are chosen to cut off "noisy" data: a constant cut-off and a so called dynamic thresholding.

The constant cut-off neglects all 3D displacements that are below a threshold of 5 µm, 10 µm, 20 µm and 30 µm. As typical length scales of *D.d.* cells range from 5 µm-10 µm, a displacement is regarded as significant if the center of (homogeneous) mass is shifted by approximately one cell length. Hence, the first two constants of 3D displacement lengths are related to the lower and upper limit of typical sizes of *D.d.* cells whereas 20 µm and

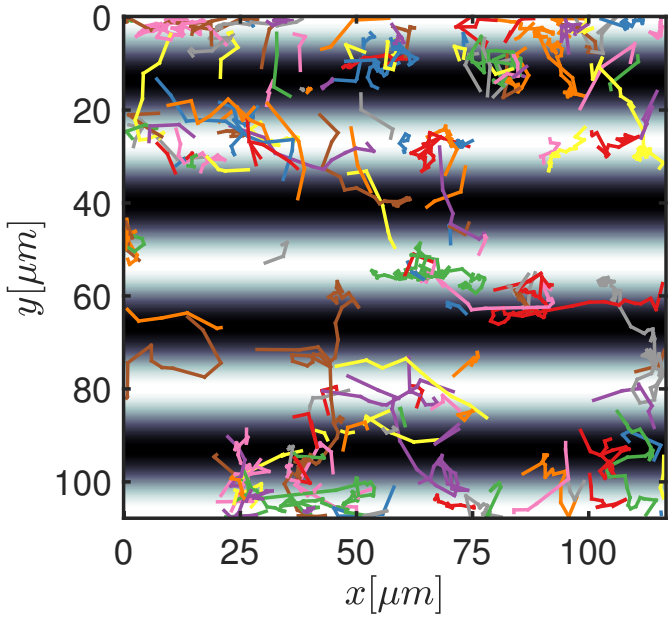

Figure 4.8: Tracks on a surface with $A = 5\,\mu m$ and a half wavelength of $\lambda/2 = 28.57\,\mu m$. The radius of maximal curvature amounts to $R = 8.29\,\mu m$. The cellular migration of *D.d.* cells alters between random and directed motility.

30 µm describe displacements of two or three times the typical cell length.

The dynamic thresholding sorts the displacement data in 10 different groups based on their value so that the first group with percentiles $0\,\% - 10\,\%$ contains the lowest values. Likewise, the last group with percentiles ranging from $90\,\% - 100\,\%$ comprises the highest values. Then, the mean value of each group k and the difference of two subsequent groups k and $k+1$ are calculated. The threshold is chosen to the index k if the mean value difference of the groups $k+1$ and k is maximal. All values below the mean value of group k are neglected in the further analysis [4]. Therefore, the threshold varies if the data are differently distributed as shown in Fig. 4.9. The example demonstrates the different cutoffs for a normal and log-normal distribution indicated by the two dashed lines in Fig. 4.9b.

Figures 4.9c and 4.9d show the mean value of the step size $\mathrm{d}r_3$ (eq. (4.26)) and its standard deviation as a function of the applied threshold. "0" implies no thresholding and "dyn." the dynamic thresholding. The error bars grow for higher thresholds since the number of data points shrinks dramatically which is why thresholds $\geq 10\,\mu m$ are not significant for the underlying statistics. The mean values for both "dyn." (dynamical thresholding) and 5 µm threshold are in the order of magnitude of the lower limit of one typical cell length. Taking into consideration the length of the error bars that are longer for the threshold of 5 µm, the dynamical thresholding will be applied in the following to

cut off the "noise" of the data. Every step that is neglected in $\mathrm{d}r_3$ due to the threshold will be also neglected in other quantities.

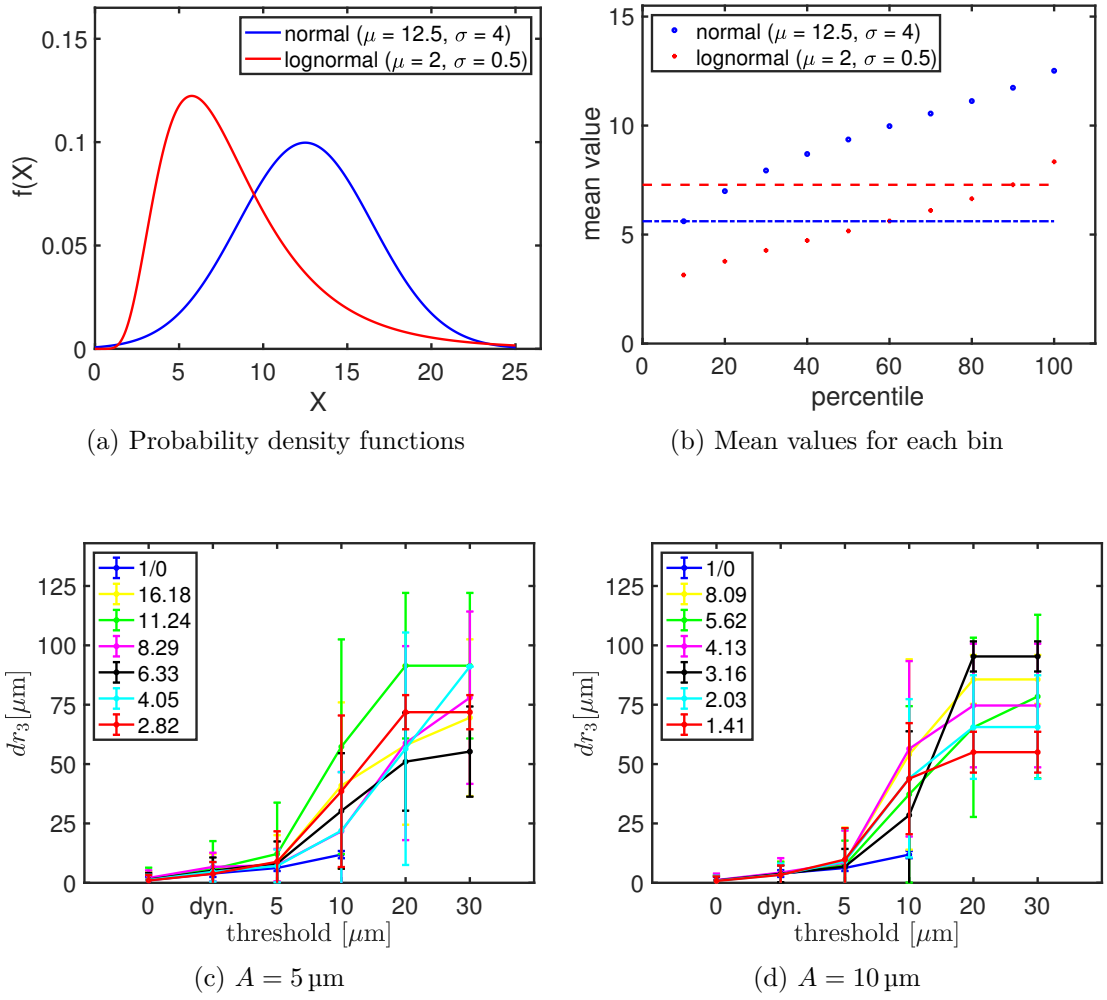

(a) Probability density functions

(b) Mean values for each bin

(c) $A = 5\,\mu\mathrm{m}$

(d) $A = 10\,\mu\mathrm{m}$

Figure 4.9: **(a)** Dynamic thresholding. First the data are sorted and classified into the percentiles $0\,\% - 10\,\%$ to $90\,\% - 100\,\%$. Then, the mean value is calculated for each group before the difference of the mean values of two subsequent groups is computed. The threshold is chosen to be the index of maximal mean value difference. **(b)** Depending on the underlying PDF, the threshold is varying as demonstrated for a normal and log-normal distribution by the dashed lines. **(c)**, **(d)** Dependence of the mean value of $\mathrm{d}r_3$ distributions and its standard deviation on the threshold. "0" implies no thresholding and "dyn." refers to the dynamical thresholding method. The error bars grow since the number of non-neglected data points shrinks dramatically for a threshold $\geq 10\,\mu\mathrm{m}$. The different colors correspond to different radii of maximal curvature.

4.3.2 Probability Density Functions of the Parameters

Probing the influence of different topographies on the cellular migration of *D.d.* cells, a significant test is applied to the different parameter sample distributions. It decides whether two data sets stem from distributions with equal mean (two-sided t-test) or with equal median (Wilcoxon rank test, [58]). The choice of the significance test is based on the underlying probability density function (PDF) of the data sets which is measured by accordance of the mean value μ, variance σ^2, skewness s and kurtosis k from the fit and data. The error of the mean value is assumed to be the standard deviation. To obtain the PDF of a data set, the Matlab® function `hist()` bins the data to N_{bins} equally distanced bars whereby the height of the bars is determined from the number of values in the bar. Next, the numbers of values in a single bin are divided by both the total number of data points and the bin width. The Matlab® function `bar()` plots the result creating a bar graph, and `pdf(PD, x)` returns a "continuous" representation the PDF object PD from the data if the sampling in x is much finer than the sampling of the bar graph.

In Tabs. 6.2 and 6.3, the statistical moments are shown for the data of the 3D step size $\mathrm{d}r_3$, the absolute value of 3D velocity v_3, the migration angle β, the curvotactic indices CI as well as CI_3 and the equatorial radius of an ellipsoid on substrates with an amplitude of $A = 5\,\mu\mathrm{m}$ and $10\,\mu\mathrm{m}$. These values are also compared to related measurements on a planar substrate where *D.d.* cells perform random motion without any external stimuli.

Notably, the experimental data are limited to $\mathbb{R}_{\geq 0}$ except for the curvotactic indices ranging only from $0 - 1$. Generally, taking into account that the standard deviation of the mean skewness of a normal distribution is $\approx \sqrt{15/2500} \approx 0.08$ and for the kurtosis $\approx \sqrt{96/2500} \approx 0.2$, values for s and k of distributions exceeding these boundaries indicate that the corresponding quantity is not symmetrically distributed. This is the case for most of the analyzed quantities in this work (Tabs. 6.2 and 6.3). Moreover, the skewness of all distributions from $\mathrm{d}r_3$, v_3 and β are negative indicating an asymmetry of the distributions around the mean value .

Since the mean step size $\mathrm{d}r_3$ and the mean velocity v_3 in 3D are positive and real numbers, the value of s and k exceed those of the standard normal distribution and $s < 0$, the data of both parameters are fitted with the Rayleigh distribution. The Rayleigh

distribution $f(x)$ [59, 60] is defined on $x \in [0, \infty)$ by

$$f(x) = \frac{x}{b^2} \exp\left(-\frac{x^2}{2b^2}\right) , \tag{4.36}$$

$$\mu = \sqrt{\pi/2}b , \tag{4.37}$$

$$\sigma^2 = \frac{4-\pi}{2}b^2 , \tag{4.38}$$

$$s = \frac{2\sqrt{\pi}(\pi-3)}{(4-\pi)^{3/2}} , \tag{4.39}$$

$$k = -\frac{6\pi^2 - 24\pi + 16}{(4-\pi)^2} + 3 , \tag{4.40}$$

where $b > 0$ is a scale parameter. As shown in Tabs. 6.4 and 6.5, there is a high overlap of the confidence intervals of the mean values for both substrates ($A = 5\,\mu\text{m}$ and $10\,\mu\text{m}$) although the values for s obtained from the fit are positive and the values for k are one order of magnitude bigger than those obtained from the data. For $\mathrm{d}r_3$, the variances σ^2 show the same behavior in the data and the fit for both amplitudes. Thus, the Rayleigh distribution appears as a reasonable representation of the sample PDF.

The migration angle β and the equatorial radius a of a prolate ellipsoid behave differently from the step size and mean velocity. As they reveal multiple maxima, the probability distribution functions are fitted with a kernel distribution function [61]. A kernel distribution is a nonparametric representation of the PDF and does not require any assumptions on the data set. This distribution is defined by a bandwidth and its kernel smoothing function.

Both chemotactic indices CI and CI_3 range from 0 to 1 and the skewness, as well as the kurtosis, exceed the mean standard deviation of the skewness and kurtosis of a normal distribution for several orders of magnitude. For this reason, the data are fitted with a Beta distribution where $x \in (0, 1)$ and $\alpha > 0$, $\beta > 0$ are (real) shape parameters. The Beta distribution $f(x)$ [62, 63] is defined as

$$f(x) = \frac{x^{\alpha-1}(1-x)^{\beta-1}}{B(\alpha, \beta)} , \tag{4.41}$$

where

$$B(\alpha, \beta) = \frac{\Gamma(\alpha)\Gamma(\beta)}{\Gamma(\alpha+\beta)} . \tag{4.42}$$

The statistical parameters are given by

$$\mu = \frac{\alpha}{\alpha+\beta} \,, \tag{4.43}$$

$$\sigma^2 = \frac{\alpha\beta}{(\alpha+\beta)^2(\alpha+\beta+1)} \,, \tag{4.44}$$

$$s = \frac{2(\beta-\alpha)\sqrt{\alpha+\beta+1}}{(\alpha+\beta+2)\sqrt{\alpha\beta}} \,, \tag{4.45}$$

$$k = \frac{6\left[(\alpha-\beta)^2(\alpha+\beta+1) - \alpha\beta(\alpha+\beta+2)\right]}{\alpha\beta(\alpha+\beta+2)(\alpha+\beta+3)} \,. \tag{4.46}$$

For both substrates ($A = 5\,\mu\text{m}$ and $10\,\mu\text{m}$) and both parameters CI and CI_3, the fit with a Beta distribution yields mean values and variances that are in high accordance with those obtained from the data set. The skewness of the data for both parameters is more than $10 - 100$ fold higher than for the fit on both substrates. For CI, the kurtosis values from both the data sample and the PDF fit are consistent. The kurtosis of the PDF fit of CI_3 is one order of magnitude smaller than the kurtosis of the data. However, in both cases the Beta distribution seems to represent the PDF from the experimental data well enough.

To conclude, a normal distribution is not appropriate to describe the PDF of the experimental data. Therefore, the Wilcoxon rank test is chosen to decide whether there is a significant difference between two different samples.

4.3.3 Statistics and Significances

In the following, the direct influence of substrate topography on the different parameters characterizing the cellular migration and cell shape is analyzed. It is necessary to apply significance tests to the data sets in order to make a decision if the two samples stem from distributions with equal or different median (in the case of Wilcoxon rank test). Thereby, the p-value is the probability that the median of two distributions is equal. The test decides for "not significant" (n.s.) if the p-value is > 0.1. If the p-value is smaller than a significance level $\alpha = 0.1$, 0.05 and 0.01, the test decides for a significant difference indicated by "$*$", "$**$" and "$***$", respectively. Table 4.3 shows the p-values for both substrates and the parameters of v_3, β, CI_3 and a. Notably, the significance test for the distributions of $\mathrm{d}r_3$ and v_3 as well as β and CI yields the same results, since the v_3 (CI) is a function of $\mathrm{d}r_3$ (β) according to the definitions in eqs. (4.28) and (4.30). In the following, $f(5\,\mu\text{m})$ refers to the substrates with $A = 5\,\mu\text{m}$ and $f(10\,\mu\text{m})$ to $A = 10\,\mu\text{m}$ where f represents a distribution of a parameter sample.

After thresholding with the dynamical method, the mean step size $\mathrm{d}r_3$ for both substrates is shown in Fig. 4.10. This parameter is obtained from the position of the center of homogeneous mass (COHM) by eq. (4.26). Figures 4.10a and 4.10b show the PDF of the data and a PDF fit with the Rayleigh distribution as well as the mean value in dependence of the radius of maximal curvature for the sinusoidal wave structures with an amplitude of $A = 5\,\mu\mathrm{m}$ and Figs. 4.10c and 4.10d for the sinusoidal wave structures with an amplitude of $A = 10\,\mu\mathrm{m}$. The p-values of the significance tests are equal to those of the distributions for v_3 and listed in Tab. 4.3. As shown in Fig. 4.10b, the mean value is highest for $R(5\,\mu\mathrm{m}) = 11.2\,\mu\mathrm{m}$ and $8.3\,\mu\mathrm{m}$ with $\mathrm{d}r_3(11.2\,\mu\mathrm{m}) = (5.7858 \pm 11.7749)\,\mu\mathrm{m}$ and $\mathrm{d}r_3(8.3\,\mu\mathrm{m}) = (6.6885 \pm 5.9775)\,\mu\mathrm{m}$ (Tab. 6.2a). Only the mean step sizes for $R(5\,\mu\mathrm{m}) = 16.1\,\mu\mathrm{m}$ and $6.3\,\mu\mathrm{m}$ are not significantly different. Importantly, the mean step sizes on sinusoidal wave structures are significantly larger than those on a planar substrates ($\mathrm{d}r_3(\infty\,\mu\mathrm{m}) = (3.9010 \pm 1.4479)\,\mu\mathrm{m}$) except for $\mathrm{d}r_3(2.8\,\mu\mathrm{m}) = (3.7869 \pm 4.9671)\,\mu\mathrm{m}$. Moreover, the standard deviation of the mean step size is also the smallest on planar surfaces indicating a more persistent migration on sinusoidal wave structures. In the case of $A = 10\,\mu\mathrm{m}$, the mean as well as the standard deviation of the step size is maximal for $R = 4.1\,\mu\mathrm{m}$ with $\mathrm{d}r_3 = (4.3067 \pm 6.0779)\,\mu\mathrm{m}$ (Tab. 6.3a) although there is no significant difference to the control experiment on planar surfaces ($\mathrm{d}r_3(\infty\,\mu\mathrm{m}) = (3.9010 \pm 1.4479)\,\mu\mathrm{m}$). Furthermore, the two data sets $\mathrm{d}r_3(2.0\,\mu\mathrm{m}) = (3.4308 \pm 4.6853)\,\mu\mathrm{m}$ and $\mathrm{d}r_3(1.4\,\mu\mathrm{m}) = (3.3401 \pm 3.9589)\,\mu\mathrm{m}$ are also not significantly different. However, the standard deviation of the control measurement on planar surfaces is smaller than on curved surfaces. Thus, the probability density for larger step sizes on curved surfaces is higher than on planar surfaces. Notably, the step size is related to a mean displacement over the time period between two stack acquisitions and is also an indicator for the persistence of the cell trajectories. Importantly, the mean step size is in the scale of a typical cell length so that we can consider the steps as significant displacements of the COHM.

The distributions of the samples from the mean velocity v_3 as well as the mean values for all substrates are shown in Fig. 4.11 and the p-values obtained from the Wilcoxon rank test in Tab. 4.3. Since $v_3 = \mathrm{d}r_3/\,\mathrm{d}t$ where $\mathrm{d}t$ is the time interval of the stack acquisition, the two distributions only differ in a constant factor so that the p-values of the significance test are equal for both parameters. Likewise, the maximal mean velocity and standard deviation on substrates with an amplitude of $A = 5\,\mu\mathrm{m}$ amount to $v_3(11.2\,\mu\mathrm{m}) = (11.5715 \pm 23.5499)\,\mu\mathrm{m\,min^{-1}}$ and $v_3(8.3\,\mu\mathrm{m}) = (13.3770 \pm 11.9551)\,\mu\mathrm{m\,min^{-1}}$ (Tab. 6.2b). The mean velocities are significantly larger than $v_3(\infty\,\mu\mathrm{m}) = (7.8020 \pm 2.8957)\,\mu\mathrm{m\,min^{-1}}$ with exception of the mean velocity $v_3(2.8\,\mu\mathrm{m}) = (7.5738 \pm 9.9342)\,\mu\mathrm{m\,min^{-1}}$. The behavior on sinusoidal waves with an amplitude of $A = 10\,\mu\mathrm{m}$ is slightly different. Similar to the mean step size $\mathrm{d}r_3$, the mean

(R_1, R_2)	v_3	β	CI_3	a
(1/0, 16.18.)	**0.0000**	0.9075	0.1173	**0.0000**
(1/0, 11.24)	**0.0000**	0.8581	0.8806	**0.0000**
(1/0, 8.29)	**0.0000**	0.8268	**0.0383**	**0.0000**
(1/0, 6.33)	**0.0000**	0.1212	0.7913	**0.0000**
(1/0, 4.05)	**0.0000**	0.7717	0.4811	**0.0000**
(1/0, 2.82)	**0.0000**	**0.0000**	**0.0000**	**0.0000**
(16.18, 11.24)	**0.0000**	0.8387	0.2812	**0.0002**
(16.18, 8.29)	**0.0000**	0.9873	0.7566	**0.0000**
(16.18, 6.33)	0.4683	0.2577	0.2978	**0.0657**
(16.18, 4.05)	**0.0027**	0.7745	0.5265	**0.0714**
(16.18, 2.82)	**0.0000**	0.0004	**0.0000**	**0.0000**
(11.24, 8.29)	**0.0000**	0.7680	0.1621	0.3708
(11.24, 6.33)	**0.0000**	0.1696	0.9703	**0.0684**
(11.24, 4.05)	**0.0787**	0.9010	0.6724	**0.0194**
(11.24, 2.82)	**0.0000**	**0.0003**	**0.0003**	0.5134
(8.29, 6.33)	**0.0000**	0.2497	0.1599	**0.0067**
(8.29, 4.05)	**0.0000**	0.6819	0.3596	**0.0014**
(8.29, 2.82)	**0.0000**	**0.0004**	**0.0000**	0.4364
(6.33, 4.05)	**0.0173**	0.1555	0.6957	0.6181
(6.33, 2.82)	**0.0000**	**0.0214**	**0.0001**	**0.0105**
(4.05, 2.82)	**0.0000**	**0.0003**	**0.0001**	**0.0006**

(a) $A = 5\,\mu m$

(R_1, R_2)	v_3	β	CI_3	a
(1/0, 8.09)	**0.0000**	0.7855	0.5910	0.1249
(1/0, 5.62)	**0.0000**	**0.0066**	**0.0001**	**0.0003**
(1/0, 4.13)	0.4095	**0.0281**	**0.0001**	**0.0030**
(1/0, 3.16)	**0.0000**	**0.0026**	**0.0003**	**0.0618**
(1/0, 2.03)	**0.0000**	**0.0000**	**0.0000**	**0.0000**
(1/0, 1.41)	**0.0000**	**0.0000**	**0.0000**	**0.0000**
(8.09, 5.62)	**0.0001**	**0.0087**	**0.0040**	**0.0000**
(8.09, 4.13)	**0.0000**	**0.0329**	**0.0036**	0.4725
(8.09, 3.16)	**0.0484**	**0.0046**	**0.0081**	**0.0016**
(8.09, 2.03)	**0.0000**	**0.0000**	**0.0000**	**0.0000**
(8.09, 1.41)	**0.0000**	**0.0000**	**0.0000**	**0.0000**
(5.62, 4.13)	**0.0000**	0.6423	0.8931	**0.0000**
(5.62,3.16)	**0.0625**	0.7883	0.8622	**0.0873**
(5.62 2.03)	**0.0000**	**0.0000**	**0.0000**	**0.0000**
(5.62, 1.41)	**0.0000**	**0.0000**	**0.0000**	**0.0209**
(4.13, 3.16)	**0.0000**	0.4202	0.7883	**0.0000**
(4.13, 2.03)	**0.0000**	**0.0000**	**0.0000**	**0.0000**
(4.13, 1.41)	**0.0000**	**0.0000**	**0.0000**	**0.0000**
(3.16, 2.03)	**0.0000**	**0.0000**	**0.0000**	**0.0000**
(3.16, 1.41)	**0.0000**	**0.0000**	**0.0000**	**0.0002**
(2.03, 1.41)	0.6267	0.2085	0.3318	**0.0000**

(b) $A = 10\,\mu m$

Table 4.3: p-values for Wilcoxon rank sum test for both substrates. Since the definition of dr_3 and v_3 (eqs. (4.26) and (4.28)) are only different by a factor and the definitions of CI and β (eqs. (4.29) and (4.30)) base on the same fraction, the significance test reveals exactly the same results at a precision of at least 10^{-4}. $R_{1,2}$ are the radii of maximal curvature from two different structures with the same amplitude. The data are thresholded by the dynamical method described in section 4.3.1. The numbers are formatted in bold, if $p < 0.1$ indicating significant differences of two samples.

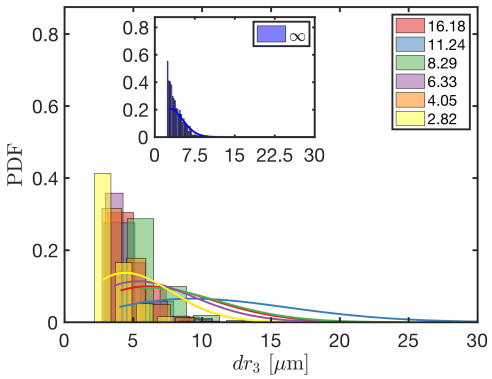

(a) Rayleigh distribution fit for $A = 5\,\mu\text{m}$.

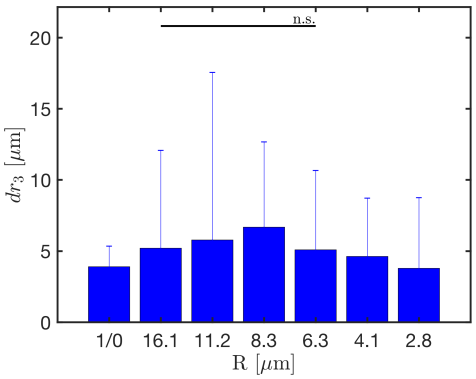

(b) $\langle \mathrm{d}r_3(R) \rangle$ for $A = 5\,\mu\text{m}$.

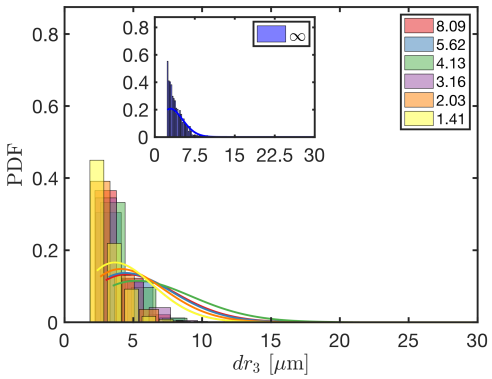

(c) Rayleigh distribution fit for $A = 10\,\mu\text{m}$.

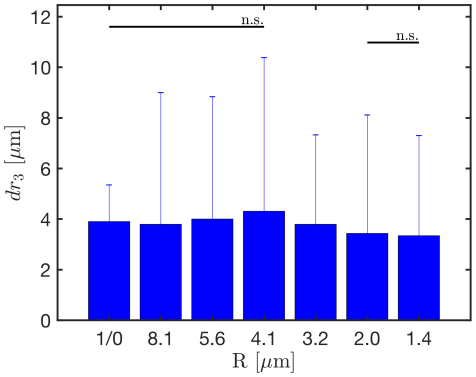

(d) $\langle \mathrm{d}r_3(R) \rangle$ for $A = 10\,\mu\text{m}$.

Figure 4.10: PDF of the effective **step size** $\mathrm{d}r_3$ and its mean value as a function of radius of maximal curvature.The effective step size $\mathrm{d}r_3$ is extracted from the positions of the center of homogeneous mass at two subsequent time points. **(a)** and **(c)** show histograms of the data and corresponding Rayleigh fits on substrates with $A = 5\,\mu\text{m}$ and $10\,\mu\text{m}$, respectively. **(b)** and **(d)** show the mean value as a function of the radius of maximal curvature and associated significance levels where the error is given by the standard deviation. In **(b)**, the data on substrates with finite radius differ significantly from the data on a planar surface ($R = 1/0\mu\text{m} = \infty\mu\text{m}$). In **(d)**, the sample distributions of $R = 2.0\,\mu\text{m}$ and $1.4\,\mu\text{m}$ as well as $R = \infty$ and $4.1\,\mu\text{m}$ are not significantly different. Each color corresponds to another structure whereby the numbers represent the radius of maximal curvature in µm.

value and the standard deviation of $v_3(4.1\,\mu m) = (8.6133 \pm 12.1558)\,\mu m\,min^{-1}$ (Tab. 6.3b) are maximal but not significantly different from the control measurement on the planar surface. Furthermore, the significance test decided for distributions of equal medians in the case of $v_3(2.0\,\mu m) = (6.8616 \pm 9.3705)\,\mu m$ and $v_3(1.4\,\mu m) = (6.6802 \pm 7.9178)\,\mu m$, i.e. they are slightly smaller than the control measurement and originate from the two substrates with lowest radius of maximal curvature. Consequently, all velocities are in the same scale and comparable to velocities of cells migrating on planar substrates. However, the probability density for higher velocities is higher on curved surfaces than on planar surfaces because of the elevated standard deviation of v_3 being consistent with the behavior for the step size dr_3.

To assess whether there is a preferential migration direction, the migration angle β is calculated for each step. This parameter is calculated by eq. (4.29) and ranges from $0° - 90°$. It is the angle between the wave vector $\vec{k}$ and the z-projected migration step $d\vec{r}_2$. Figure 4.13 shows the PDF of the data as well as the mean values for both classes of substrates with each $A = 5\,\mu m$ and $10\,\mu m$. The migration angle β for $A = 5\,\mu m$ demonstrates that there is only a significant difference to the data acquired on the sinusoidal waves with $R = 2.8\,\mu m$ (Tab. 4.3 and Fig. 4.13b) at significance levels of $\alpha = 0.1$ and 0.01. The mean values of the planar surface as well as for all sinusoidal wave substrates are close to 45° where the standard deviation is $\approx 27°$ except for $\beta(2.8\,\mu m) = (50.3939 \pm 27.1474)°$ (Tab. 6.2c). Additionally, the PDF for β from the data and the PDF fit in Fig. 4.13a resembles an equal distribution where only in the PDF of the sample with $R = 2.8\,\mu m$ is a higher preference for direction roughly perpendicular to the wave vector. On substrates with an amplitude of $A = 10\,\mu m$, there is no significant change in the migration angle between $R = \infty$ and $8.1\,\mu m$, $R = 5.6\,\mu m$, $4.1\,\mu m$ and $3.2\,\mu m$ as well as $R = 2.0\,\mu m$ and $1.4\,\mu m$ (Fig. 4.13d and Tab. 4.3). The mean values change from $\beta(\infty\,\mu m) = (45.1957 \pm 26.6931)°$, $\beta(5.6\,\mu m) = (47.6604 \pm 26.7702)°$ to $\beta(2.0\,\mu m) = (53.2916 \pm 26.7231)°$ (Tab. 6.3c). Unlikely to Fig. 4.13a, the skewness is lower for the PDF in Fig. 4.13c, i.e. on the substrates with $A = 10\,\mu m$, indicating a higher probability to migrate at angles closer to 90°. From these results, we suggest that the migration angle is only biased if the radius of maximal curvature is small enough and that cells then tend to migrate orthogonally to the wave vector. Figure 4.12 shows all positions of the COHM for each cell during the entire tracking. The positions of COHM are mainly located in concave regions suggesting that cells crawl preferentially along concavely curved regions. Otherwise, the direction of cellular migration appears to be not significantly different from that of randomly migrating cells.

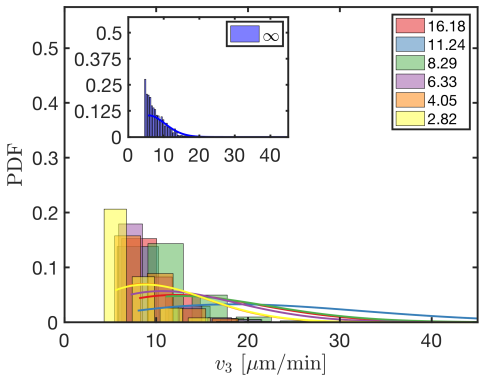

(a) Rayleigh distribution fit for $A = 5\,\mu\text{m}$.

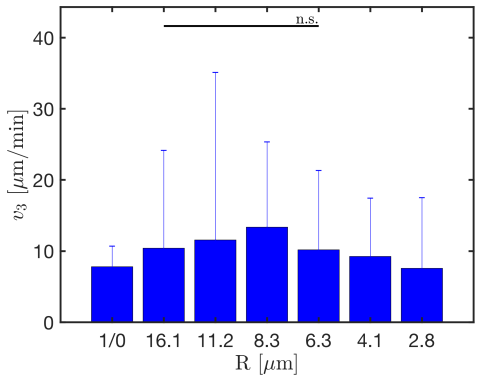

(b) $\langle v_3(R) \rangle$ for $A = 5\,\mu\text{m}$.

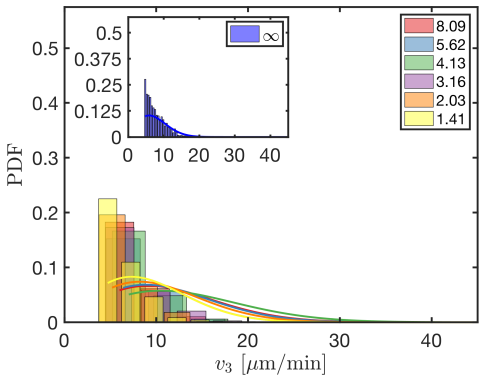

(c) Rayleigh distribution fit for $A = 10\,\mu\text{m}$.

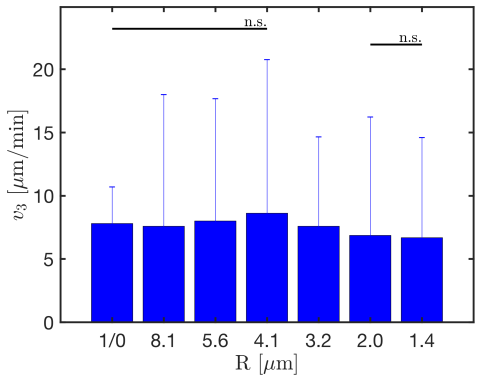

(d) $\langle v_3(R) \rangle$ for $A = 10\,\mu\text{m}$.

Figure 4.11: PDF of the **3D velocity** v_3 and its mean value as a function of radius of maximal curvature.The effective velocity v_3 is extracted from the positions of the center of homogeneous mass at two subsequent time points divided by the time interval. **(a)** and **(c)** show histograms of the data and corresponding Rayleigh fits on substrates with $A = 5\,\mu\text{m}$ and $10\,\mu\text{m}$, respectively. **(b)** and **(d)** show the mean value as a function of the radius of maximal curvature and associated significance levels where the error is given by the standard deviation. In **(b)**, the data on substrates with finite radius differ significantly from the data on a planar surface ($R = 1/0\mu\text{m} = \infty\mu\text{m}$). In **(d)**, the sample distributions of $R = 2.0\,\mu\text{m}$ and $1.4\,\mu\text{m}$ as well as $R = \infty$ and $4.1\,\mu\text{m}$ are not significantly different. Each color corresponds to another structure whereby the numbers represent the radius of maximal curvature in µm.

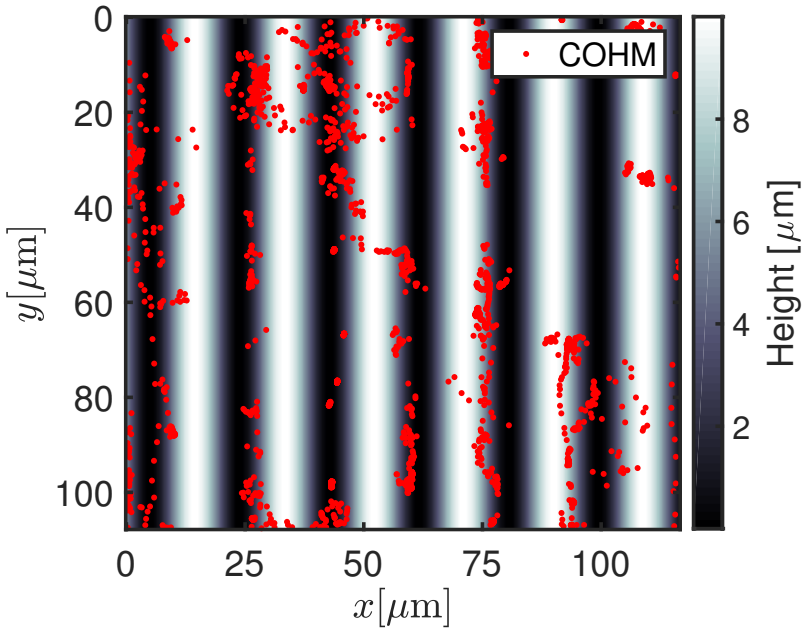

Figure 4.12: Positions of the center of homogeneous mass for each cell and every time point over the whole track. The bright regions of the substrate have a concave curvature whereas the dark regions have a convex one. There are more cells in dark than in bright regions. The substrate has an amplitude of $A = 10\,\mu m$ and a half wavelenght of $\lambda/2 = 16.67\,\mu m$.

Another parameter to characterize the preferential direction of migration steps of motile *D.d.* cells is the curvotactic index. It is related to the chemotactic index that literature often refers to and it is defined by eq. (4.30). The PDF of the data obtained on sinusoidal-shaped surfaces as well as on a flat control surface are shown for both amplitudes in Fig. 4.14 whereby the statistic parameters are presented in Tabs. 6.2d and 6.3d. Since the CI is defined as $\cos^2(\beta)$ and $\beta \in [0°, 90°]$ where $\cos^2(\beta)$ is monotonously decreasing, the Wilcoxon rank test yields the same p-values as for β (Tab. 4.3). Analogously to β, CI points out that there is no significant difference from random motility ($CI \approx 0.5$) on all substrates but for $R = 2.8\,\mu m$ (Figs. 4.14a and 4.14b). The significance levels are $\alpha = 0.1$ and 0.01 and $CI(2.8\,\mu m) = 0.4292 \pm 0.3639$. The PDF shows slightly higher values at the boundaries where the PDF of the data from $R = 2.8\,\mu m$ is maximal at $CI \approx 0$. Apart from that, the PDF remains roughly constant. On substrates with $A = 10\,\mu m$, there is an increasing trend with the radius of maximal curvature (Fig. 4.14d). Furthermore, the PDF fit in Fig. 4.14c reveals at $CI \approx 0.9$ that the probability density for $R = 8.1\,\mu m$ is higher than for $R = 1.4\,\mu m$. Again, there is no significant change of CI between $R = \infty$ and $8.1\,\mu m$, $R = 5.6\,\mu m$, $4.1\,\mu m$ and $3.2\,\mu m$ as well as $R = 2.0\,\mu m$ and $1.4\,\mu m$ (Fig. 4.14d and Tab. 4.3). The mean values change from $CI(\infty\,\mu m) = 0.4989 \pm 0.3602$,

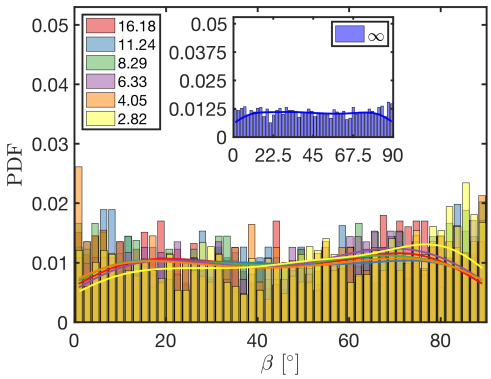

(a) Kernel distribution fit for $A = 5\,\mu m$.

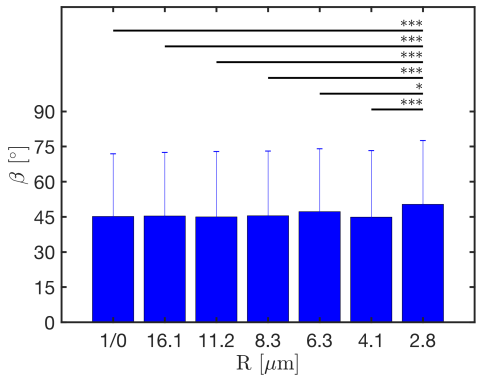

(b) $\langle \beta(R) \rangle$ for $A = 5\,\mu m$.

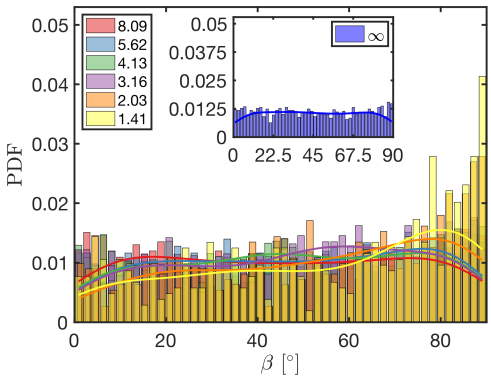

(c) Kernel distribution fit for $A = 10\,\mu m$.

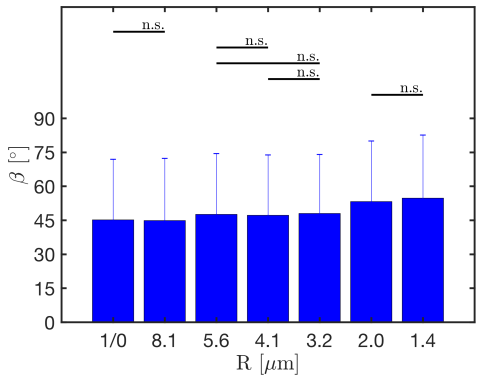

(d) $\langle \beta(R) \rangle$ for $A = 10\,\mu m$.

Figure 4.13: PDF of the migration angle β and its mean value as a function of radius of maximal curvature. The migration angle β is calculated by eq. (4.29). **(a)** and **(c)** show histograms of the data and corresponding Kernel fits on substrates with $A = 5\,\mu m$ and $10\,\mu m$, respectively. **(b)** and **(d)** show the mean value as a function of the radius of maximal curvature and associated significance levels where the error is given by the standard deviation. In **(b)**, the data on substrates with finite radius differ significantly from the data on a planar surface ($R = 1/0\mu m = \infty\mu m$) but there is no significant difference for data obtained on sinusoidal surfaces. In **(d)**, the mean value of the migration angle tends to decrease with increasing radius of maximal curvature. Each color corresponds to another structure whereby the numbers represent the radius of maximal curvature in μm.

$CI(5.6\,\mu m) = 0.4653 \pm 0.3618$ to $CI(2.0\,\mu m) = 0.3930 \pm 0.3573$ (Tab. 6.3d). Hence, the results suggest that the migration direction is biased for small radii of maximal curvatures. Then, the cells show a slight preference to crawl orthogonally to the direction of the wave vector, thus, avoiding crossing the waves.

Another definition of the curvotactic index is given by eq. (4.31) comparing the directions of 3D displacement and wave vector shown in Fig. 4.15. The data from the experiments on both surface structures with amplitudes of $A = 5\,\mu m$ and $10\,\mu m$ are presented in Figs. 4.15a and 4.15c where the data are fitted with a Beta distribution. The PDF fit in Fig. 4.15a shows the highest probability density for the data of $R = 8.29\,\mu m$ and lowest for $R = 2.82\,\mu m$ ($CI_3(2.82\,\mu m) = 0.3190 \pm 0.3088$) at $CI_3 \approx 0.9 - 1$. Figure 4.15b confirms these findings as all data samples differ significantly from the substrate with $R = 2.82\,\mu m$ at a significance level $\alpha = 0.01$. Additionally, there is a significant difference of $CI_3(8.29\,\mu m) = 0.4100 \pm 0.3325$ and $CI_3(\infty\,\mu m) = 0.3765 \pm 0.3175$ at $\alpha = 0.1$ (Tabs. 4.3 and 6.2e). In Fig. 4.15c, the probability density of $R = 8.09\,\mu m$ in the range of $CI_3 \approx 0.9 - 1$ for substrates of an amplitude $A = 10\,\mu m$ is the highest whereas the distributions of $R = 2.03\,\mu m$ and $1.41\,\mu m$ reveal the smallest values for the PDF of CI_3. The mean values related to the distributions of the data in Fig. 4.15d and Tab. 6.2e amount to $CI_3(\infty\,\mu m) = 0.3694 \pm 0.3146$, $CI_3(8.09\,\mu m) = 0.3694 \pm 0.3146$ and $CI_3(1.41\,\mu m) = 0.2579 \pm 0.2920$. The red, dashed line at $CI_3 = 1/3$ in Figs. 4.15b and 4.15d indicates the unconfined 3D random motion (section 4.3). But this value has to be corrected since the *D.d.* crawling on surfaces are confined to the substrate topography. Thus, "1/3" does not correspond to the random motion corrected for the attainable space. Analogously to the distributions of β and CI on substrates with $A = 10\,\mu m$, the data of $R = \infty\mu m$ and $8.09\,\mu m$, $R = 5.62\,\mu m$, $4.13\,\mu m$ and $3.16\,\mu m$ and $R = 2.03\,\mu m$ and $1.41\,\mu m$ show no significant difference. Therefore, as before, we draw the conclusion that the bias on the direction of cellular motion is small except for the two substrates with smallest radius of maximal curvature.

Beside the quantification of the directionality of cellular migration of *D.d.* cells on sinusoidal-shaped surfaces, the shape is quantified by the equatorial radius of an prolate ellipsoid (eq. (4.35)). The PDF fits with a kernel distribution as well as the corresponding data are shown in Figs. 4.16a and 4.16c for substrates with an amplitude of $A = 5\,\mu m$ and $10\,\mu m$, respectively. The PDF fits of the equatorial radius reveal two maxima at $a \approx 2\,\mu m$ and $a \approx 5\,\mu m$. Since motile cells are more elongated or even polarized than inactive cells, the peak with smaller a is identified with motile and the peak with higher a with inactive cells. Importantly, the cells were not exposed to an external chemical stimulus. Figures 4.16b and 4.16d show the mean values for the distribution on each substrate whereby the mean value is given by the standard deviation. There is no clear trend in Fig. 4.16b. However, according to the results of the significance test,

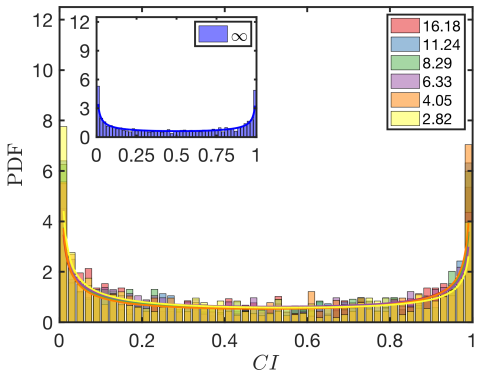

(a) Beta distribution fit for $A = 5\,\mu\text{m}$.

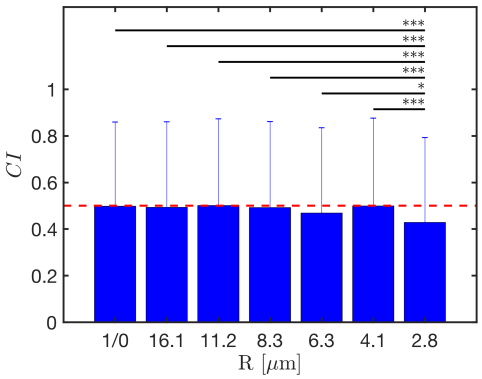

(b) $\langle CI(R) \rangle$ for $A = 5\,\mu\text{m}$.

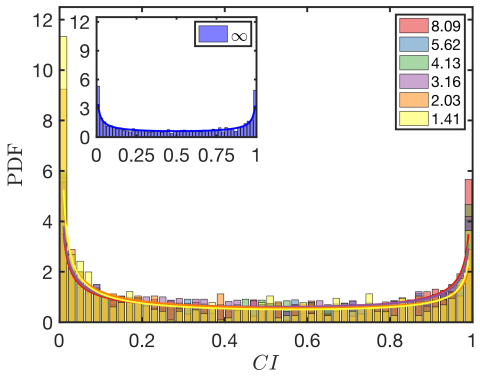

(c) Beta distribution fit for $A = 10\,\mu\text{m}$.

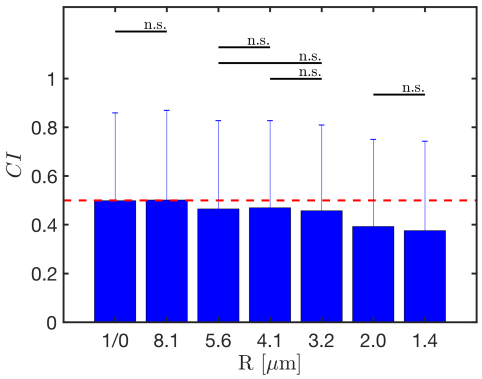

(d) $\langle CI(R) \rangle$ for $A = 10\,\mu\text{m}$.

Figure 4.14: PDF of the curvotactic index CI and its mean value as a function of radius of maximal curvature. The curvotactic index CI is calculated by eq. (4.30). **(a)** and **(c)** show histograms of the data and corresponding fits with the Beta distribution on substrates with $A = 5\,\mu\text{m}$ and $10\,\mu\text{m}$, respectively. **(b)** and **(d)** show the mean value as a function of the radius of maximal curvature and associated significance levels where the error is given by the standard deviation. The red, dashed line in **(b)** and **(d)** indicates the CI for random motion, i.e. for an equally distributed migration angle. In contrast to **(d)**, there is only significant difference to the sample on the substrate with $R = 2.8\,\mu\text{m}$ in **(b)**. Each color corresponds to another structure whereby the numbers represent the radius of maximal curvature in µm.

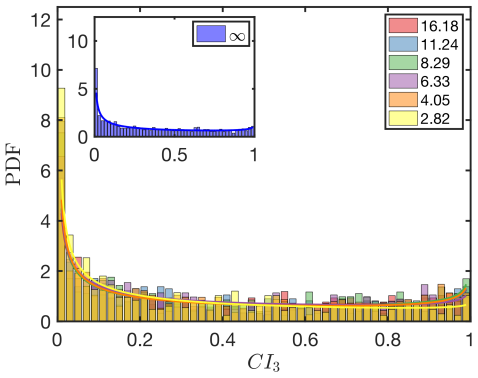

(a) Beta distribution fit for $A = 5\,\mu\text{m}$.

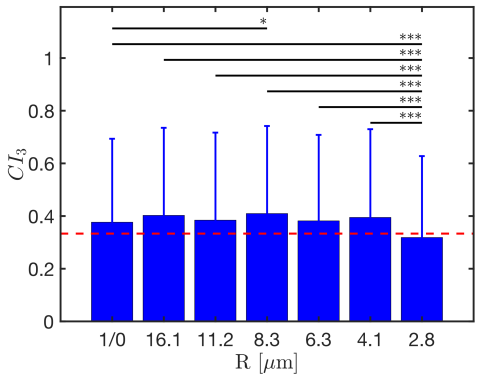

(b) $\langle CI_3(R) \rangle$ for $A = 5\,\mu\text{m}$.

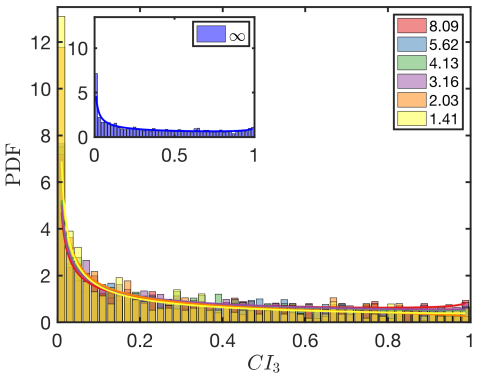

(c) Beta distribution fit for $A = 10\,\mu\text{m}$.

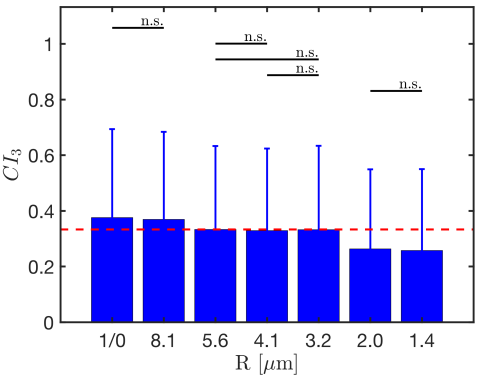

(d) $\langle CI_3(R) \rangle$ for $A = 10\,\mu\text{m}$.

Figure 4.15: PDF of the **curvotactic index** CI_3 and its mean value as a function of radius of maximal curvature. The curvotactic index CI_3 is calculated by eq. (4.31). **(a)** and **(c)** show histograms of the data and corresponding fits with the Beta distribution on substrates with $A = 5\,\mu\text{m}$ and $10\,\mu\text{m}$, respectively. **(b)** and **(d)** show the mean value as a function of the radius of maximal curvature and associated significance levels where the error is given by the standard deviation. The red, dashed line in **(b)** and **(d)** indicates the CI_3 for random motion in 3D, i.e. for an equally distributed migration angle. In contrast to **(d)**, there are only significant difference to the sample on the substrate with $R = 2.8\,\mu\text{m}$ in **(b)** as well as between the control measurement and the distribution of $R = 8.3\,\mu\text{m}$ at a significance level $\alpha = 0.1$. Each color corresponds to another structure whereby the numbers represent the radius of maximal curvature in µm.

the equatorial radius is significantly smaller on the the planar substrate ($a(\infty\,\mu\text{m}) = (2.5942 \pm 2.0930)\,\mu\text{m}$)) compared to measurements on sinusoidal-shaped surfaces with $A = 5\,\mu\text{m}$ where $a \geq 3\,\mu\text{m}$ (Tabs. 4.3 and 6.2f). As shown in Fig. 4.16d and Tab. 6.3f, there is no significant difference between $a(\infty\,\mu\text{m})$ and $a(8\,\mu\text{m}) = (2.5143 \pm 2.0396)\,\mu\text{m}$. Furthermore, the data do not show any trend depending on the substrates radius of maximal curvature R. The results indicate that there are more motile cells on planar surfaces.

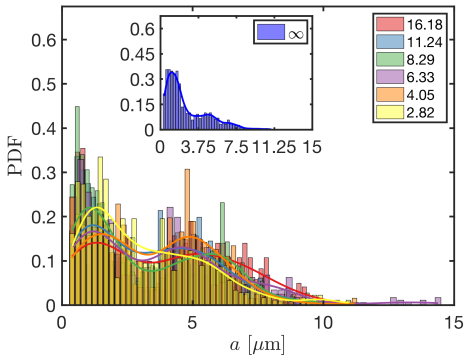

(a) Kernel distribution fit for $A = 5\,\mu\text{m}$.

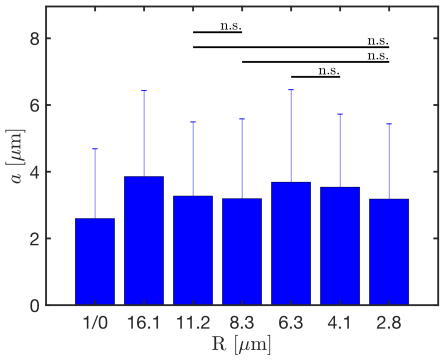

(b) $\langle a(R) \rangle$ for $A = 5\,\mu\text{m}$.

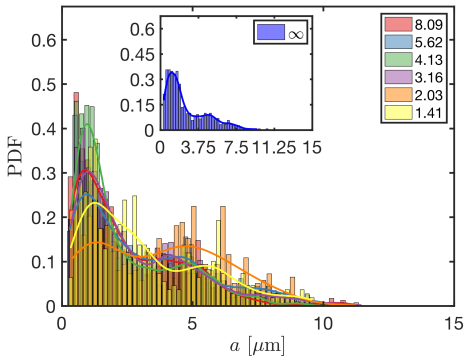

(c) Kernel distribution fit for $A = 10\,\mu\text{m}$.

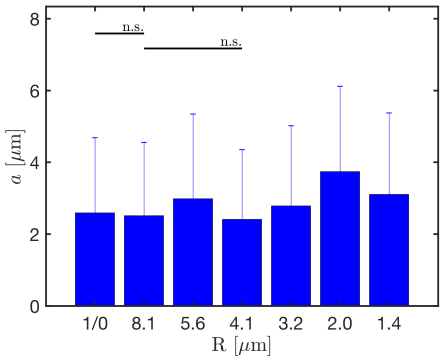

(d) $\langle a(R) \rangle$ for $A = 10\,\mu\text{m}$.

Figure 4.16: PDF of the **equatorial radius of a prolate ellipsoid** a and its mean value as a function of radius of maximal curvature. The equatorial radius a is calculated by eq. (4.35) and a measure for the cell shapes. **(a)** and **(c)** show histograms of the data and corresponding fits with the Kernel distribution on substrates with $A = 5\,\mu\text{m}$ and $10\,\mu\text{m}$, respectively. **(b)** and **(d)** show the mean value as a function of the radius of maximal curvature R and associated significance levels where the error is given by the standard deviation. The shape parameter depending on R does not show any unique trend. Each color corresponds to another structure whereby the numbers represent the radius of maximal curvature in μm.

4.4 Single Cell Force Spectroscopy

The analysis of cellular migration on curved surfaces points out an influence of surface topography if the radii of maximal curvature are small enough. Then, cells on sinusoidal curved substrates feel confined which leads to a biased migration direction. As cell-substrate adhesion, as well as cortical tension, might play a crucial role, single cell force experiments are used to investigate cell-substrate adhesion on convexly curved surfaces. The force-retraction experiments are performed with *D.d.* cells on sinusoidal surfaces (see section 3.2.1) with an amplitude $A = 20\,\mu m$ and a wavelength of $\lambda/2 = 20.00\,\mu m$ as shown in Fig. 6.1. The high amplitude is chosen to ensure that the experiments are performed in the "curvotactic" regime and that cells are exposed to a sufficiently curved surface topography. The experiments on planar surfaces were performed during an internship at the Max Planck Institute for Dynamics and Self-Organization in 2017. Since *D.d.* cells, being attached to a cantilever tip, are still motile, it is impossible to provide the information which exact radius of curvature of the substrate they sense. However, the radius of curvature of the regions that the *D.d.* cells were exposed to was in between $0.5\,\mu m - 3\,\mu m$ in the range of biased motion. As cells tend to maximize their work of adhesion, there is a competition between cell-substrate adhesion and cortical tension affecting the stretching energy of the cell. To assess how cortical actin influences cell-substrate adhesion, the cells are incubated with CK666 concentrations of $0\,\mu M$, $5\,\mu M$, $10\,\mu M$ and $100\,\mu M$ because the Arp2/3 knock out in *D.d.* cells is lethal.

In the experiments, we acquire force-distance curves (FDC) as depicted in Fig. 4.17. The signal originates from deflection of the cantilever tip that is transformed into a force with the help of prior calibration of the AFM setup. During the extension of the piezo, the cantilever does not exert any forces to the attached cell. Only if the cell is in contact with the surface of the substrate, a force is acting against the cortical tension of the cell. Retracting the cell from the surface, the cell is exposed to forces related to the detachment yielding the retraction curve. Here, cell-substrate adhesion is quantified by the maximal force of adhesion F_{ad}^{max}, work of (de-) adhesion W_{ad}, lifetime τ, number of steps N_{st} and the height of last step h_{ls} where the results are compared to cell-substrate adhesion on planar surfaces. The lifetime $\tau = d/v$ of the cell-substrate adhesion is calculated by where v is the pulling velocity and d the distance of the de-adhesion event. The related amount of cells and analyzable FDC are shown in Tab. 4.4. Since the data are acquired with 4 different cell populations on different days, it is reasonable to assume the data as independent.

[CK666]	# cells	# FDC
0 µM	20	94
5 µM	23	118
10 µM	18	82
100 µM	18	89

(a) Curved substrate

# cells	# FDC
6	20
7	32
3	21

(b) Planar substrate

Table 4.4: Statistics of experiments on single cell force spectroscopy. The number of cells and force-distance-curves (FDC) are presented for CK666 concentrations of 0 µM, 5 µM, 10 µM and 100 µM. The data in **(a)** stem from 4 different cell populations.

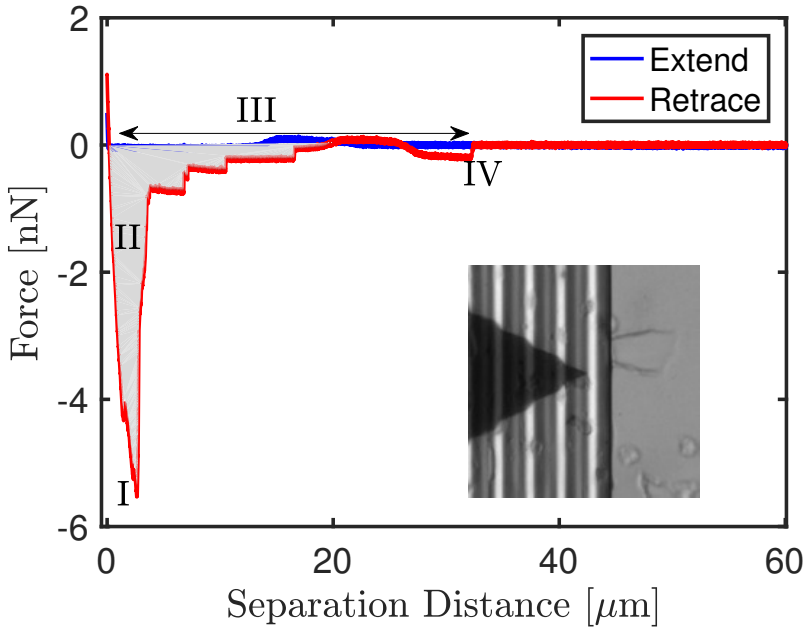

Figure 4.17: Force Distance Curve acquired from single cell force spectroscopy. A single *D.d.* cell is picked by the cantilever tip far away from the wave maximum where the force-retraction experiments are performed on. The picture shows the cell in contact with the sinusoidal-shaped surface. I: maximal force of adhesion F_{ad}^{max} (nN), II: work of de-adhesion W_{ad} (10^{-14} J), III: distance of detachment (µm), IV: height of last step (pN). The parameter settings are shown in table 3.1.

4.4.1 Statistics and Significances

Since we want to assess the effect of Arp2/3 inhibition with CK666 on the cortical actin network, we have to compare the samples with each other for each parameter of interest with the help of appropriate significance tests. Analogue to section 4.3.3, if statistical parameters, such as μ, σ^2, s and k, point out that the data are well described by a normal distribution, the two-sample t-test is applied. Otherwise, the Wilcoxon rank sum test is chosen as it does not assume normally distributed data. In the following, "$*$", "$**$" and "$***$" denote the significance levels of $p < \alpha = 0.1$, 0.05 and 0.01, respectively, where p is the probability that two sample distributions have the same median (Tabs. 4.5 and 4.6). The red line in the boxplots represents the median of the distribution. The box comprises 50% of the data set where the bottom edge is a sign for the $25\hat{}th$ percentile (q_1) and the upper one for $75\hat{}th$ percentile (q_3). The whisker covers the data range that is not considered as outliers. x is an outlier if $x < q_1 - w \cdot (q_3 - q_1)$ or $x > q_3 + w \cdot (q_3 - q_1)$ with the maximum whisker length $w = 1.5$ by default. Furthermore, the mean values are taken from the experimental data and the mean value $\mu_p\,(\mu_c)$ is related to **p**lanar (**c**urved) surfaces.

Figure 4.18 shows the PDF of the data and the boxplot for F_{ad}^{max} on both curved (Figs. 4.18a and 4.18b) and planar (Figs. 4.18c and 4.18d) surfaces. Each of the data sets is fitted with a log-normal PDF to guarantee consistency, although the PDF from data on planar surfaces for [CK666] = 5 µM reveal a different behavior in Fig. 4.18c. As depicted in Fig. 4.18b, inhibition of the Arp2/3 complex reduces F_{ad}^{max} significantly compared to no inhibition at a significance level of $\alpha = 0.1$ and 0.05. According to Tab. 6.6a, the mean value decreases from $\mu_c(0\,\mu\text{M}) = (4.7837 \pm 4.4540)\,\text{nN}$ to $\mu_c(5\,\mu\text{M}) = (3.8424 \pm 3.6319)\,\text{nN}$, $\mu_c(10\,\mu\text{M}) = (4.0561 \pm 6.1809)\,\text{nN}$ and $\mu_c(100\,\mu\text{M}) = (3.8279 \pm 3.9114)\,\text{nN}$. However, there is no significant change in the data for [CK666] = 5 µM, 10 µM and 100 µM in the case of curved surfaces (Tab. 4.5a). In contrast to this, all samples in Fig. 4.18d decrease significantly ($\alpha = 0.05$ and 0.01) where the p-values are shown in Tab. 4.5b. More precisely, the mean values reduce from $\mu_p(5\,\mu\text{M}) = (5.3024 \pm 2.6080)\,\text{nN}$ over $\mu_p(10\,\mu\text{M}) = (3.2214 \pm 2.2836)\,\text{nN}$ to $\mu_p(100\,\mu\text{M}) = (0.8713 \pm 0.6389)\,\text{nN}$ (Tab. 6.7a). Comparing the data sets of F_{ad}^{max} from curved and planar surfaces and taking into account the p-values in Tab. 4.6, both samples for [CK666] = 5 µM and 100 µM reveal a significant difference whereas there is no significant difference for [CK666] = 10 µM. Notably, the mean value $\mu_p(5\,\mu\text{M}) > \mu_c(5\,\mu\text{M})$ and $\mu_c(100\,\mu\text{M}) < \mu_c(100\,\mu\text{M})$. From that, we suggest that curvature might stabilize cell-substrate adhesion as F_{ad}^{max} is a first estimator for adhesion strength.

The work of (de-)adhesion W_{ad} shows a similar behavior as depicted in Fig. 4.19. Analogue to F_{ad}^{max}, the data both from planar and curved surfaces are fitted with a

Parameter	0/5	0/10	0/100	5/10	5/100	10/100
F_{ad}^{max}	**0.0686**	**0.0198**	**0.0546**	0.4337	0.7293	0.6693
W_{ad}	**0.0800**	**0.0014**	**0.0005**	**0.0623**	**0.0263**	0.6342
τ	0.6678	**0.0001**	**0.0191**	**0.0001**	**0.0110**	0.1216
h_{ls}	**0.0586**	**0.0000**	**0.0796**	**0.0023**	0.8529	**0.0278**
N_{st}	0.2560	**0.0000**	**0.0000**	**0.0006**	**0.0002**	0.7902

(a) Curved surface

Parameter	5/10	5/100	10/100
F_{ad}^{max}	**0.0358**	**0.0000**	**0.0004**
W_{ad}	0.1402	**0.0000**	**0.0000**
τ	0.1051	0.5593	**0.0574**
h_{ls}	**0.0010**	0.4848	**0.0043**
N_{st}	**0.0749**	0.2252	0.7153

(b) Planar surface

Table 4.5: Influence of different CK666 concentrations on force-retraction experiments with *D.d.* cells on **(a)** curved and **(b)** planar surfaces. The numbers 0, 5, 10 and 100 represent different samples with corresponding concentrations of CK666 in µM. The numbers are formatted in bold, if $p < 0.1$ indicating significant differences of two samples. The precision of listed p-values from the significance test is 10^{-4}.

Parameter	[CK666] = 5 µM	[CK666] = 10 µM	[CK666] = 100 µM
F_{ad}^{max}	**0.0246**	0.6847	**0.0000**
W_{ad}	0.8154	0.2058	**0.0000**
τ	0.3890	**0.0006**	0.8751
h_{ls}	**0.0042**	**0.0080**	**0.0336**
N_{st}	0.1687	0.2529	0.7377

Table 4.6: Probabilities for two samples with equal CK666 concentrations of 5 µM, 10 µM and 100 µM on **each planar and curved** surfaces. The numbers are formatted in bold, if $p < 0.1$ indicating significant differences of two samples.

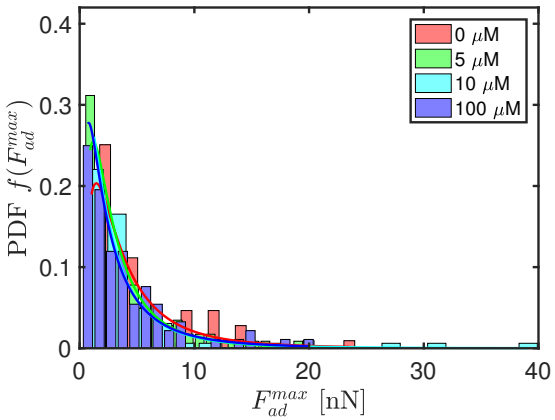

(a) Data from curved surface and exponential fit

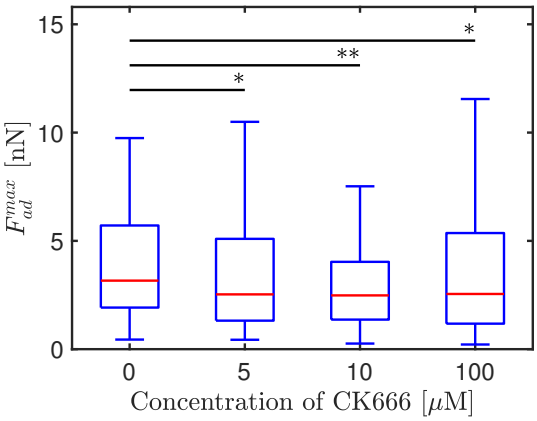

(b) Boxplot and significance levels of data from curved surface

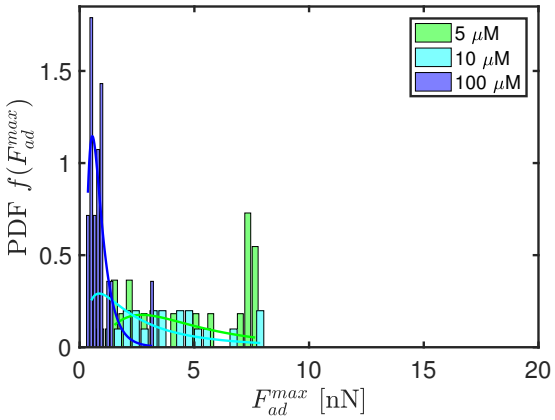

(c) Data from planar surface and exponential fit

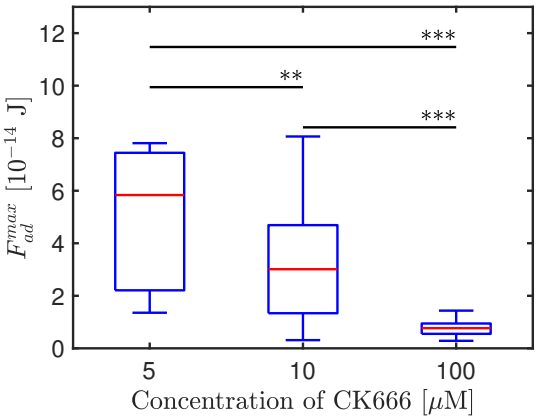

(d) Boxplot and significance levels of data from planar surface

Figure 4.18: The maximal force of adhesion F_{ad}^{max} is extracted from force-distance curves for each concentration and surface. **(a)** and **(c)** show histograms of the data and corresponding log-normal fits on curved and planar substrates, respectively. **(b)** and **(d)** show boxplots of data acquired on curved and planar substrates, respectively, and associated significance levels where the red line represents the median. In **(b)**, the data with [CK666] = 5 µM, 10 µM and 100 µM differ significantly from the data with [CK666] = 0 µM. In **(d)**, all sample distributions reveal significant difference.

log-normal PDF (Figs. 4.19a and 4.19c). In both figures, the log-normal PDF fit appears to be an appropriate description for the overall behavior of the samples. Furthermore, the data acquired on curved surfaces decrease significantly with the concentration of CK666 except for [CK666] = 10 µM and 100 µMa (Fig. 4.19b, Tab. 4.6). In the case of significant change, the mean values decay with inhibitor concentration of CK666 as $\mu_c(0\,\mu\text{M}) = (1.4900 \pm 1.6358) \times 10^{-14}\,\text{J}$, $\mu_c(5\,\mu\text{M}) = (1.0177 \pm 1.0170) \times 10^{-14}\,\text{J}$ and $\mu_c(10\,\mu\text{M}) = (0.8189 \pm 0.8666) \times 10^{-14}\,\text{J}$ (Tab. 6.6b). In contrast to the data from curved surfaces, there is a significant decay of W_{ad} for [CK666] = 5 µM and 100 µM as well as for [CK666] = 10 µM and 100 µM at $\alpha = 0.01$ whereas there is no significant proof that the samples with [CK666] = 5 µM and 10 µM stem from distributions with different medians on planar surfaces. According to Tab. 6.7b, the mean values of W_{ad} decrease dramatically for planar surfaces with $\mu_p(5\,\mu\text{M}) = (1.0232 \pm 1.0859) \times 10^{-14}\,\text{J}$, $\mu_p(10\,\mu\text{M}) = (0.6227 \pm 0.7111) \times 10^{-14}\,\text{J}$ and $\mu_p(100\,\mu\text{M}) = (0.0875 \pm 0.1711) \times 10^{-14}\,\text{J}$. Figure 4.23 and Tab. 4.6 show that the data with [CK666] = 100 µM reveal a highly significant difference with $\mu_p(100\,\mu\text{M}) < \mu_c(100\,\mu\text{M})$ at $\alpha = 0.01$. W_{ad} is a measure for the energy that is stored in the cell due to adaptation to the surface topography during cell-substrate adhesion. This leads to the suggestion that more energy is stored in the cell for high concentration of CK666 if it is adherent to a curved surface than to a flat one.

In Fig. 4.20, the PDFs and boxplots for the lifetime τ are shown. The lifetime is a quantity that describes the kinetics of biological bonds as τ accounts for the time of the last detachment event. The kinetics also include unspecific adhesion sites through van der Waals, hydrophobic and electrostatic interactions. In agreement with Tab. 6.6c, the data are fitted with a normal distribution wherefore the significance is tested by the two-sample t-test. Both samples with [CK666] = 0 µM and 5 µM have significantly higher mean values than the samples with [CK666] = 10 µM and 100 µM on curved surfaces whereby the test rejects the H_0 hypothesis of the t-test (equal means) at the significance level $\alpha = 0.05$ and 0.01 (Tab. 4.5a). While the mean values of the lifetime τ on curved surfaces amount to $\mu_c(0\,\mu\text{M}) = (9.7278 \pm 0.3403)\,\text{s}$ and $\mu_c(5\,\mu\text{M}) = (10.1066 \pm 7.0153)\,\text{s}$, the mean values are smaller for higher concentrations of CK666 with $\mu_c(10\,\mu\text{M}) = (6.5112 \pm 5.4839)\,\text{s}$ and $\mu_c(100\,\mu\text{M}) = (7.8209 \pm 5.5338)\,\text{s}$ suggesting a threshold behavior. On planar surfaces, only the data from [CK666] = 10 µM and 100 µM are significantly different at $\alpha = 0.1$. The mean values are similar to those from the data on curved surfaces. They account for $\mu_p(5\,\mu\text{M}) = (7.8653 \pm 4.1667)\,\text{s}$, $\mu_p(10\,\mu\text{M}) = (10.4692 \pm 4.4756)\,\text{s}$ and $\mu_p(100\,\mu\text{M}) = (6.3650 \pm 3.0740)\,\text{s}$ so that the lifetime τ does not show any monotone dependence on the concentration of CK666 during experiments on planar surfaces. Comparing the data from both curved and planar surfaces, the sample distributions of [CK666] = 10 µM reveal a significant difference (Tab. 4.6 and Fig. 4.23c) where

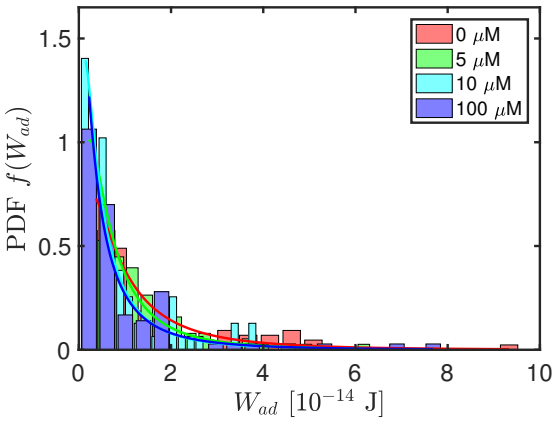

(a) Data from curved surface and exponential fit

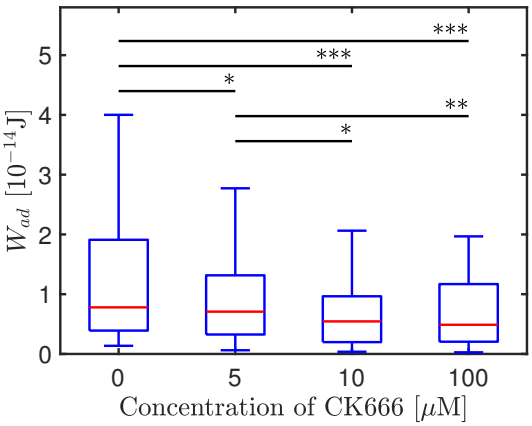

(b) Boxplot and significance levels of data from curved surface

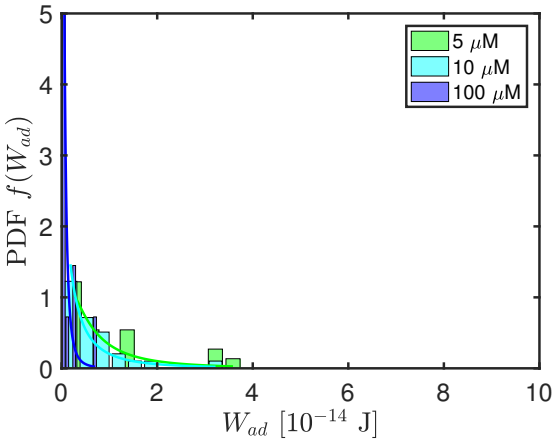

(c) Data from planar surface and exponential fit

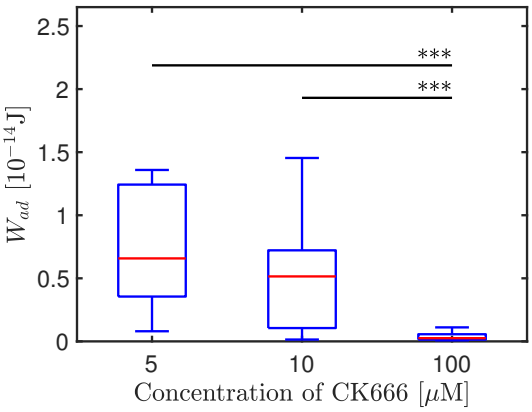

(d) Boxplot and significance levels of data from planar surface

Figure 4.19: The work of (de-) adhesion W_{ad} is extracted from force-distance curves for each concentration and surface. **(a)** and **(c)** show histograms of the data and corresponding log-normal fits on curved and planar substrates, respectively. **(b)** and **(d)** show boxplots of data acquired on curved and planar substrates, respectively, and associated significance levels where the red line represents the median. In **(b)**, the sample distributions are significantly different but for [CK666] = 10 µM and 100 µM. In **(d)**, the sample distributions for [CK666] = 5 µM and 10 µM reveal significant difference from [CK666] = 100 µM.

$\mu_c(10\,\mu M) < \mu_p(10\,\mu M)$. Nevertheless, it is possible that the sample of [CK666] = 10 µM does not properly describe the real median (or mean value) due to low statistics. For this reason, it is still possible to assume that the kinetics of adhesion sites remain the same on curved and planar surfaces.

The PDF of the height of last step h_{ls} is well described by a log-normal distribution (Tab. 6.6d and Fig. 4.21a). Hence, we apply the Wilcoxon rank sum test to the data testing for significance. On curved surfaces, there is no significant difference for [CK666] = 0 µM and 100 µM and [CK666] = 10 µM and 100 µM but the other samples differ from each other at significance levels of $\alpha = 0.1$ and 0.01 (Fig. 4.21b and Tab. 4.5b). Nevertheless, the mean values are all in the same order of magnitude with $\mu_c(0\,\mu M) = (148.1422 \pm 78.1605)\,pN$, $\mu_c(5\,\mu M) = (128.9656 \pm 69.1869)\,pN$, $\mu_c(10\,\mu M) = (101.9002 \pm 51.8213)\,pN$ and $\mu_c(100\,\mu M) = (158.0910 \pm 135.6547)\,pN$. In the case of samples from planar surfaces, the samples from [CK666] = 5 µM and 100 µM are not significantly different whereas the samples from [CK666] = 5 µM and 10 µM and [CK666] = 10 µM and 100 µM reveal different mean values at a significance level of $\alpha = 0.01$ (Tab. 4.5b). The mean values amount to $\mu_p(5\,\mu M) = (81.6294 \pm 29.2471)\,pN$, $\mu_p(5\,\mu M) = (125.6556 \pm 49.7453)\,pN$ and $\mu_p(5\,\mu M) = (71.1429 \pm 30.5419)\,pN$ (Tab. 6.7d). For both types of substrates, there is no real trend for the development of h_{ls} depending on the CK666 concentration. However, the samples on both substrates reveal a significant difference for [CK666] = 5 µM and 10 µM as well as for [CK666] = 10 µM and 100 µM at $\alpha = 0.01$ (Tab. 4.6 and Fig. 4.23d). Notably, single transmembrane proteins rapture from the surface at a load of $80\,pN - 120\,pN$ and peripheric proteins at $20\,pN - 50\,pN$. Tethers are able to resist a pulling force of $200\,pN - 1000\,pN$ [12]. As $\mu_c(5\,\mu M \text{ and } 100\,\mu M) > \mu_p(5\,\mu M \text{ and } 100\,\mu M)$, there might be an impact of curvature on the assembly of adhesion proteins at the membrane. Possibly, also the membrane tension varies wherefore tether rupture events take place.

To investigate the distributions of adhesion sites on the underside of the cell, we further analyzed the number of steps N_{st} that are followed by a force plateau. Figure 4.22 shows the data and boxplots for N_{st} on both planar and curved surfaces. According to the corresponding statistics presented in Tab. 6.6e and the PDF in Fig. 4.22a for curved substrates, the data are fitted with a log-normal distribution which is why we choose again the Wilcoxon rank sum test to test for significance. As depicted in Fig. 4.22b, the mean values of samples with [CK666] = 0 µM and 5 µM are significantly higher than those of the samples with [CK666] = 10 µM and 100 µM at a significance level $\alpha = 0.01$. But there is no significant change for the samples with [CK666] = 0 µM and 5 µM and [CK666] = 10 100. As the mean values of the data measured on curved surfaces vary from $\mu_c(0\,\mu M) = 6.5275 \pm 4.5664$, $\mu_c(5\,\mu M) = 5.6281 \pm 3.5288$ and $\mu_c(10\,\mu M) = 3.9634 \pm 2.7507$ to $\mu_c(100\,\mu M) = 4.0000 \pm 3.0295$, they are in the same

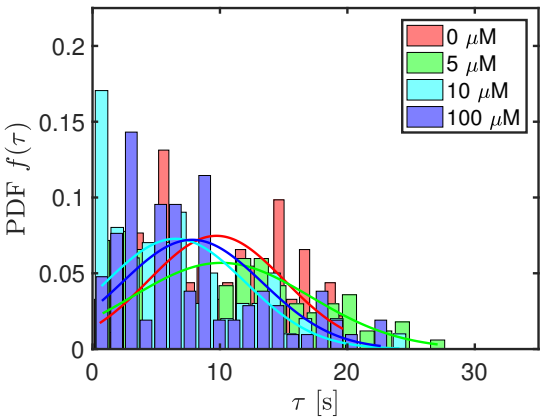

(a) Data from curved surface and normal fit

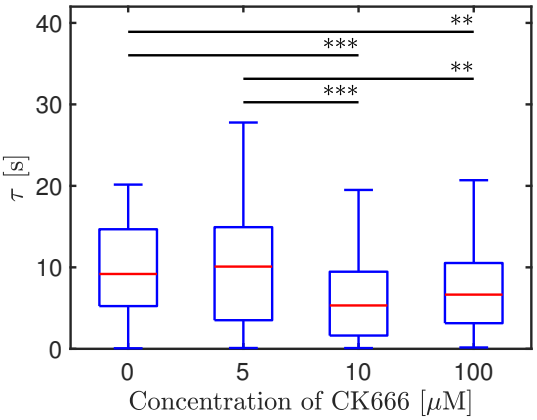

(b) Boxplot and significance levels of data from curved surface

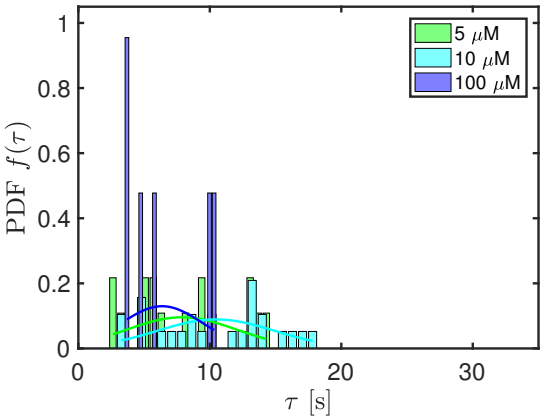

(c) Data from planar surface and normal fit

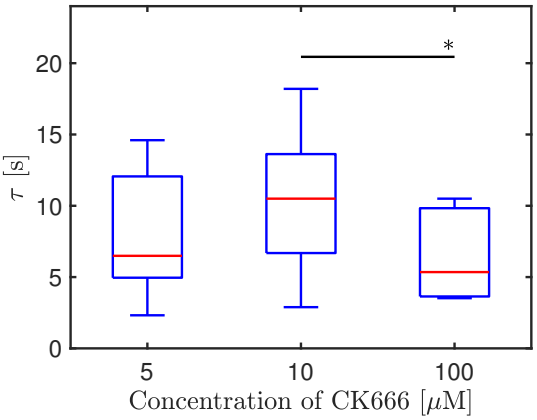

(d) Boxplot and significance levels of data from planar surface

Figure 4.20: The lifetime τ is extracted from force-distance curves for each concentration and surface. **(a)** and **(c)** show histograms of the data and corresponding normal fits on curved and planar substrates, respectively. **(b)** and **(d)** show boxplots of data acquired on curved and planar substrates, respectively, and associated significance levels where the red line represents the median. In **(b)**, the sample distributions are significantly different but for [CK666] = 0 µM and 5 µM and [CK666] = 10 µM and 100 µM. In **(d)**, the sample distributions for [CK666] = 5 µM and 10 µM reveal significant difference from each other.

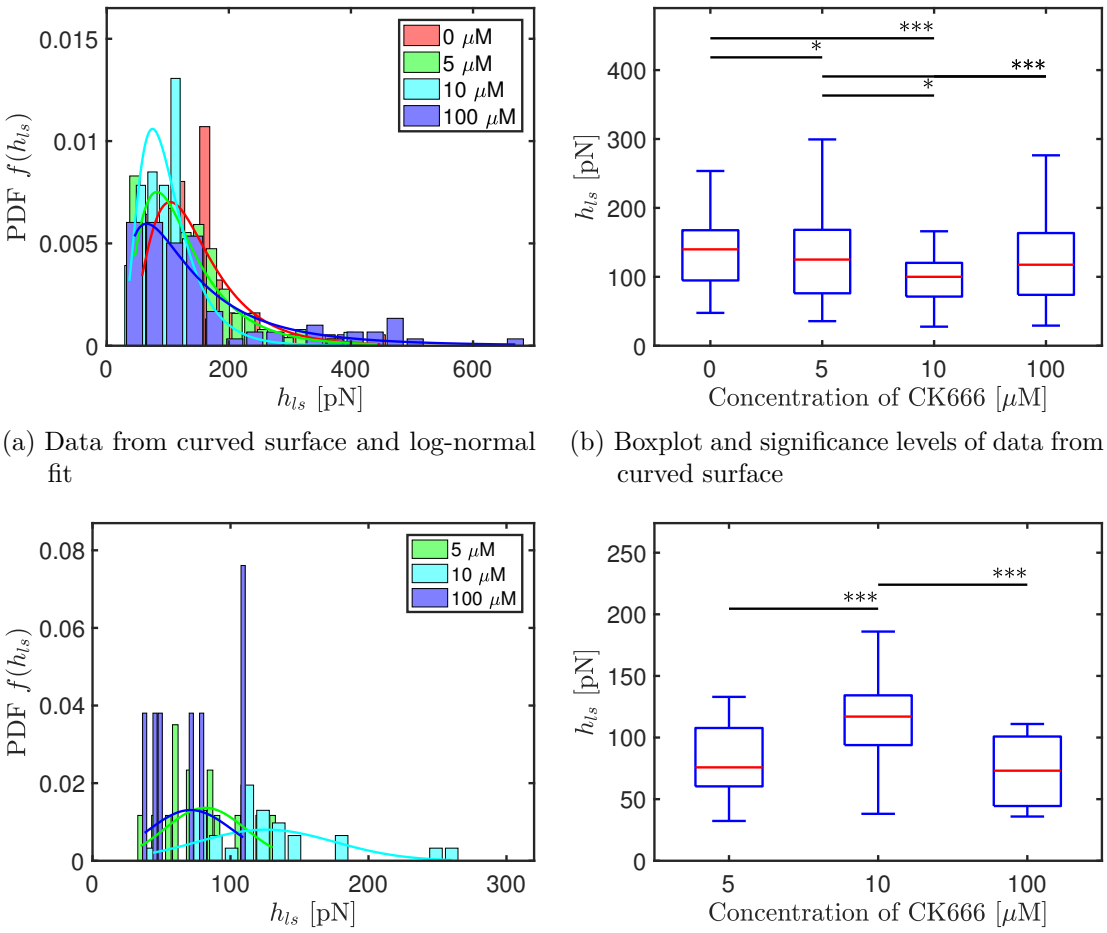

(a) Data from curved surface and log-normal fit

(b) Boxplot and significance levels of data from curved surface

(c) Data from planar surface and log-normal fit

(d) Boxplot and significance levels of data from planar surface

Figure 4.21: The height of last step h_{ls} is extracted from force-distance curves for each concentration and surface. **(a)** and **(c)** show histograms of the data and corresponding log-normal fits on curved and planar substrates, respectively. **(b)** and **(d)** show boxplots of data acquired on curved and planar substrates, respectively, and associated significance levels where the red line represents the median. In **(b)**, the sample distributions are significantly different but for [CK666] = 0 µM and 100 µM and [CK666] = 10 µM and 100 µM. In **(d)**, the sample distributions for [CK666] = 5 µM and 10 µM and [CK666] = 10 µM and 100 µM reveal significant difference between each other.

order of magnitude as those obtained from experiments on planar surfaces. Namely, they are $\mu_p(5\,\mu\text{M}) = 8.2353 \pm 6.6005$, $\mu_p(10\,\mu\text{M}) = 5.2222 \pm 4.3086$ and $\mu_p(100\,\mu\text{M}) = 4.8571 \pm 4.2201$ (Tab. 6.7e). There is only a significant difference in the distributions for [CK666] = 5 µM and 10 µM at $\alpha = 0.1$ (Fig. 4.22d and Tab. 4.5b). Noteworthily, there is a threshold behavior since concentrations of CK666 exceeding $5\,\mu\text{M} - 10\,\mu\text{M}$ reduce the number of steps and, therefore, the number of adhesion sites at the underside of the cell. This is not confirmed by the behavior of the data from planar surfaces. This might be owed to low statistics as well. The comparison of data from both planar and curved surfaces does not show a significant difference in the distributions (Fig. 4.23e). Thus, we conclude that important biological properties that are necessary and strongly influencing cell-substrate adhesion, such as chemical structure of a surface or its roughness, are conserved in the experiments on planar as well as curved substrates.

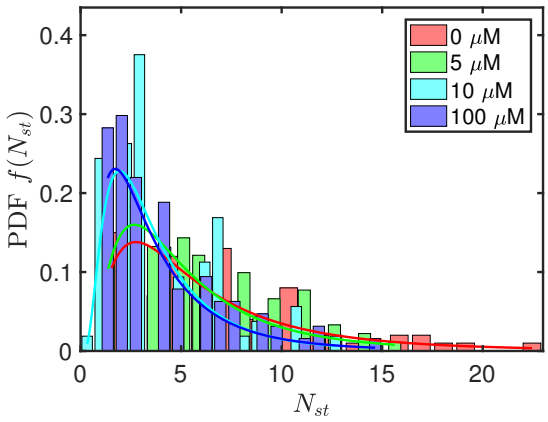

(a) Data from curved surface and log-normal fit

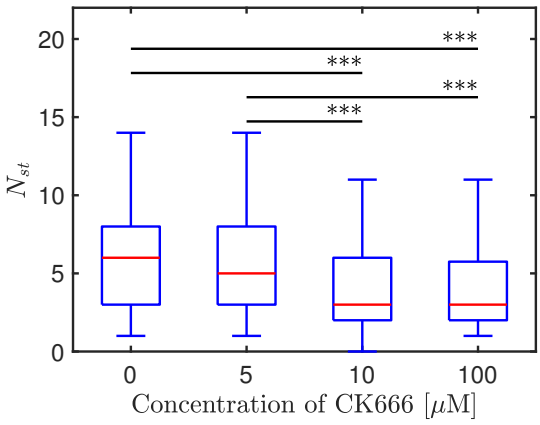

(b) Boxplot and significance levels of data from curved surface

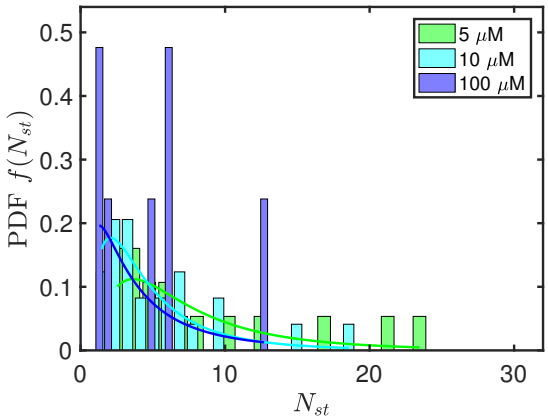

(c) Data from planar surface and log-normal fit

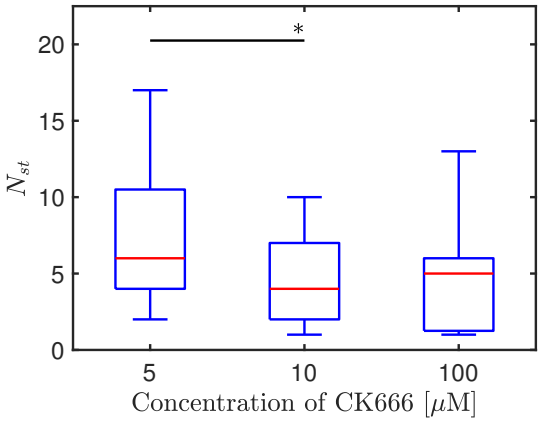

(d) Boxplot and significance levels of data from planar surface

Figure 4.22: The number of steps N_{st} is extracted from force-distance curves for each concentration and surface. **(a)** and **(c)** show histograms of the data and corresponding log-normal fits on curved and planar substrates, respectively. **(b)** and **(d)** show boxplots of data acquired on curved and planar substrates, respectively, and associated significance levels where the red line represents the median. In **(b)**, the sample distributions are significantly different but for [CK666] = 0 µM and 5 µM and [CK666] = 10 µM and 100 µM. In **(d)**, the sample distributions for [CK666] = 5 µM and 10 µM reveal significant difference from each other.

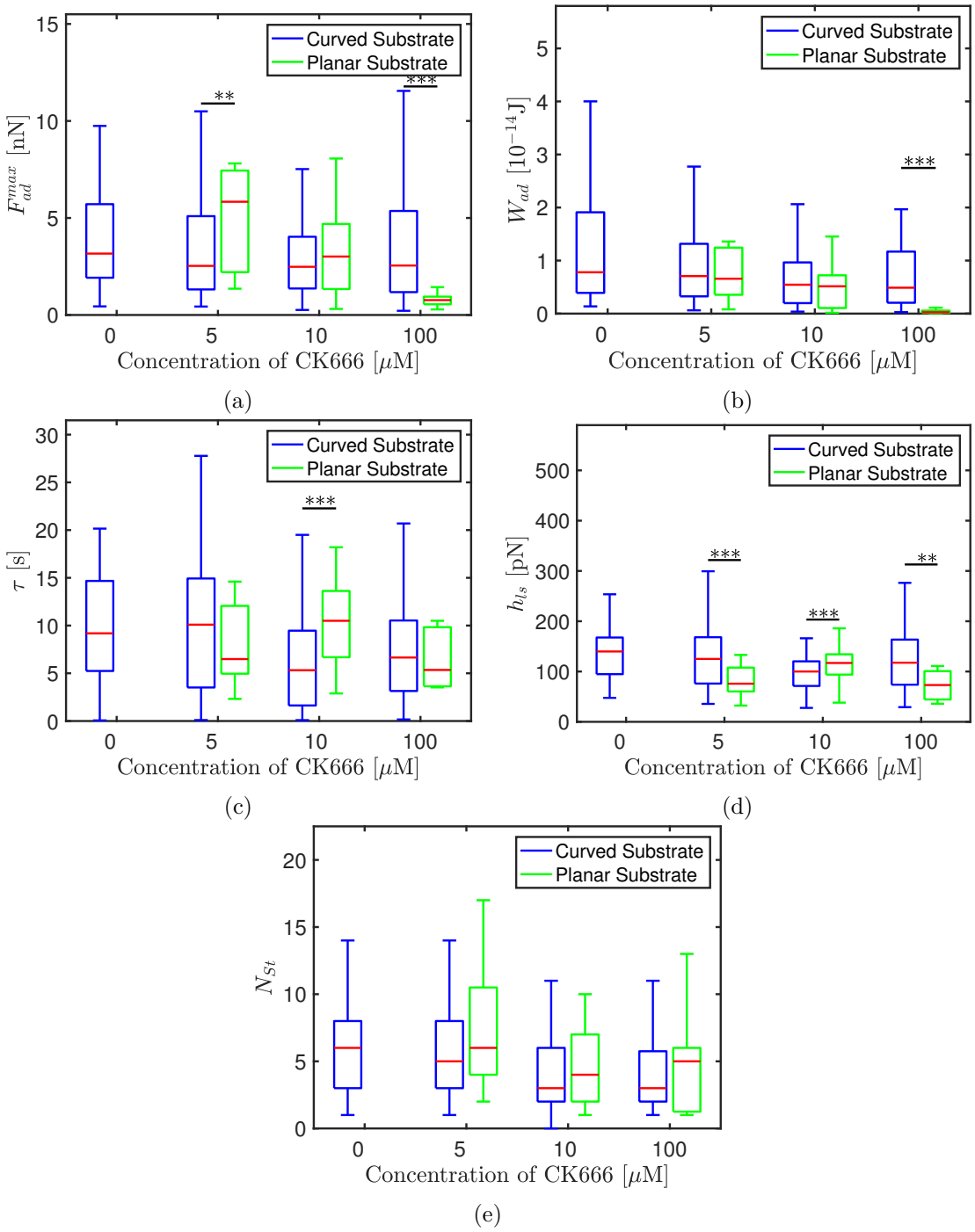

Figure 4.23: Combined boxplots of the parameters F_{ad}^{max}, W_{ad}, τ, h_{ls} and N_{st} obtained from SCFS experiments on both planar and curved surfaces. The data for [CK666] = 5 µM, 10 µM and 100 µM are tested for a significant difference between those acquired on planar surfaces and curved surfaces. Except for the number of steps N_{st}, there is at least one pair that differs significantly from each other.

5 Discussion and Outlook

In this chapter, the production of sinusoidal surfaces and the results obtained from 3D cell tracking over time as well as single cell force spectroscopy will be discussed. Additionally, the results will be compared to other works.

5.1 Sinusoidal Surfaces

The sinusoidal surfaces are topographies with varying curvature and are, therefore, more complex than topographies with constant curvature, e.g. cylindrical structures. In contrast to cylindrical optical fibers, sinusoidal surfaces have both convexly and concavely curved regions. In [33], Christoph Blum *et al.* made cylindrical structures of radii $25\,\mu m - 120\,\mu m$ by pulling on optical glass fibers having a convex curvature. Since the pulling did not produce fibers with constant radii in the full pulling regime, *D.d.* cell migration on top of cylindrical structures was tracked in regions that indicated optically a constant radius. For increasing the complexity of the substrate, Christoph Blum *et al.* created also sinusoidal structures based on PDMS wrinkles. But these wrinkles were neither perfectly parallel nor of exact sinusoidal shape complicating a profound analysis of the *D.d.* cell migration. Additionally, *D.d.* cells were exposed to surfaces having strictly speaking more than one curved direction as the wrinkles did not show parallel "wavefronts".

In this work, we used 3D printing to produce the negatives of well defined and parallel oriented sinusoidal structures that the *D.d.* cells migrated on. The photoresist IP-S, in combination with the 25x objective ($0.5\,\mu m - 1\,\mu m$ resolution), yielded stable structures. However, without any surface smoothing, the printed negatives showed a rather step-like than sinusoidal surface topography. In detail, the spacing ($\approx 1\,\mu m - 2\,\mu m$) of the nanoridges in Driscoll *et al.* ($\approx 0.6\,\mu m$ height and $\approx 250\,nm$ width) was exactly in the same order of magnitude that was identified to be efficient in contact guidance. Unlike the high contact guidance efficiency for $\approx 1\,\mu m - 2\,\mu m$, smaller scales of spacing $\approx 400\,nm$ were the least effective [26].

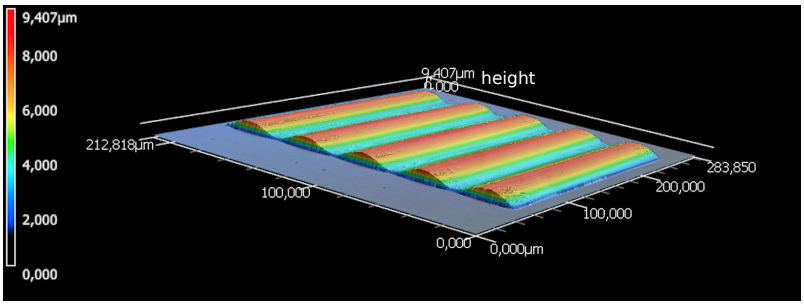

Figure 5.1: 3D scan of a sinusoidal structure with $A = 5\,\mu m$ and $N_{wm} = 5$. The surface is both well defined and smooth. The z-axis represents the height of the structure in µm.

Therefore, surface smoothing with the help of a method suggested by Taubin [54] was applied. Especially, the root mean square surface roughness was reduced to values $\leq 100\,nm$. Hence, migrating *D.d.* cells were not further guided by nanotopographic influences and influences related to curvature sensing by BAR/IBAR could be excluded as well. These proteins were most of all sensitive to length scales of up to 200 nm in regions of curved membrane surfaces [27] as well as in more extended membrane structures like filopodia. The use of the 63x objective combined with IP-Dip photoresist would lead to a higher resolution but it would also increase the surface roughness. Besides, the voxel size could be regulated down to $150\,nm - 300\,nm$.

To test the quality and to quantify the surface roughness of the negatives, we scanned the surfaces with an AFM in contact mode. The cantilever tips used for the scans were $17\,\mu m - 27\,\mu m$ wide in combination with a tip height of $2.5\,\mu m - 8\,\mu m$ whereby the peak-to-peak distance of the printed wave maxima varied from $\approx 16.7\,\mu m - 40\,\mu m$. Taking into account the amplitudes of $A = 5\,\mu m$ and $10\,\mu m$, it was not possible to scan the regions around the minima due to limitations related to the cantilever geometry. Furthermore, it already took roughly 1.5 h to scan a region with $25\,\mu m \times 25\,\mu m$ at a resolution of $512\,px \times 512\,px$. However, the scan area covered only a small percentage of the entire structure. Therefore, we scanned each structure at least in two different regions. Recently, another possibility is the 3D laser scanning microscope (VK–X1000) provided by Keyence that scanned a larger region of interest in a much shorter time. The scan of a structure with $A = 5\,\mu m$ and $N_{wm} = 5$ with a 50x objective is shown in Fig. 5.1 demonstrating that the field of view is large enough to image the entire structure and that the surface of the structure is both well defined and smooth.

It is necessary to print equivalent structures to those produced in this work with the aim to expose *D.d.* cells also to structures with higher radii of maximal curvature. A reasonable amplitude amounts to $A = 2.5\,\mu m$ as this is certainly lower than a typical

D.d. height. In this case, the radii of maximal curvature are in the order of magnitude of those of the cylindrical optical fibers in [33]. Hence, it seems obvious to assume that the behavior of *D.d.* cells will be comparable to the related findings on constantly convex curved substrates. Otherwise, the local curvatures would influence the cell migration stronger than the global properties. In this context, it is also desirable to print iterating cylindrical structures with similar radii of curvature to the sinusoidal structures.

Possible future projects also include measurements on circular sinusoidal wave structures in order to introduce a second direction of principal curvature around the wave center. Given that the amplitude $A \gtrsim 5\,\mu m$, we expect that *D.d.* cells are confined in concave regions migrating around the wave center if they are far away from the wave center. Otherwise, if the radius of the second principal curvature is comparable to length scales of a typical *D.d.* cell and smaller than the radius of maximal principal curvature parallel to the wave vector, the migration direction might point radially away from the center. If the amplitude decays in addition and if *D.d.* cells are far away from the center, the radius of the second principal direction curvature is much larger than the length scales of a typical *D.d.* cell. Thus, the *D.d.* cell migration in these regions is comparable to random motion on planar surfaces. Analogously, we expect a change in the directionality of *D.d.* cell migration on substrates with varying wavelength (Song *et al.* in [30]) and/or amplitude. The larger the wavelength, the more random *D.d.* cell migration.

Generally, the radius of maximal curvature is only a local parameter which does not contain any information about global topography except for substrates with constant curvature (e.g. a cylinder). Therefore, it could be favorable to classify regions with different curvature by different radii of curvature.

5.2 Contact Guidance

As explained in section 3.4, *D.d.* cells were exposed to the sinusoidal substrates and, thereby, faced a geometrically complex environment. We observed their motion with the help of a spinning disk microscope and acquired 3D data over time. Regarding the signal to noise ratio (SNR), the optical signal was acceptable for the actin label mRFPmars-LimΔcoil and was used for the 3D cell tracking with the help of Imaris. Unfortunately, the SNR was really low for myosinII-GFP such that it could not be analyzed. In this regard, the gene vector for myosinII-GFP was not sufficiently effective. Additionally, the exposure time had to be short to prevent bleaching for long-lasting tracks. For the same reason, the laser power could not be even more increased. Therefore,

for the analysis of temporal and spatial signals of 2 different labels, the SNR of the second label has to be improved.

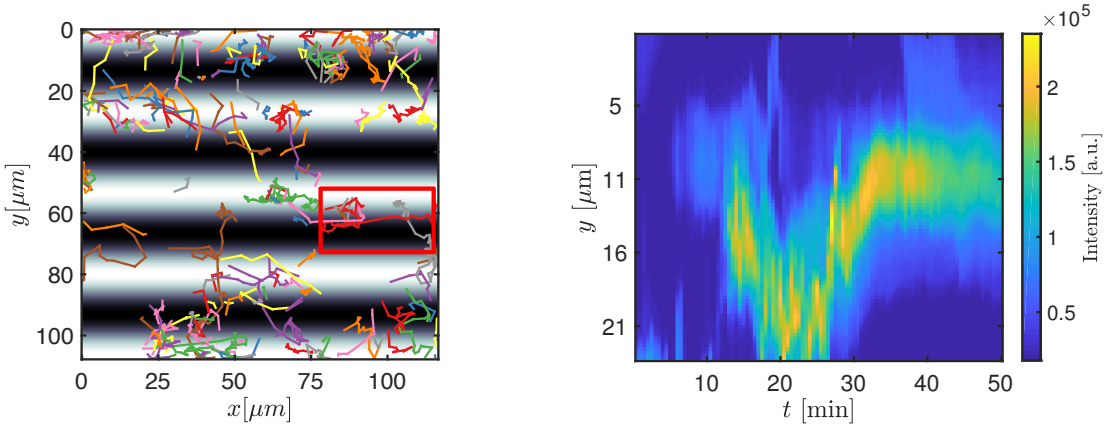

(a) The box marks the analyzed area of the z-projected images.

(b) Kymograph of the marked area.

Figure 5.2: Cell tracks of the center of homogeneous mass over time **(a)** and kymograph **(b)** of the actin signal. The red box in **(a)** marks the region whereby the red colored track moving from right to left is represented as a kymograph in **(b)**. The intensity I depends only on the direction parallel to the wave vector y in µm and the time t in min. The related cell appears around $t = 12$ min and shows zig-zagging in the time between 13 min and 30 min where the tracks suggests a directed cell migration along the wave structure. Afterwards, the cell enters random motility and the kymograph appears symmetric in the projection.

A [µm] | λ [µm]	0	40.00	33.33	28.57	25.00	20.00	16.67
5	0.0106	0.0242	-0.0422	0.0099	-0.0053	-0.0072	-0.0456
10	0.0106	-0.0449	-0.0393	-0.0398	-0.0090	0.0611	0.0277

Table 5.1: Correlation coefficient r of the cell velocity and the migration angle calculated with Maltab® function `corr2` using Pearson's definition with $-1 \leq r \leq 1$. If $r > (<) 0$, the correlation of two variables is positive (negative) meaning that an increasement (decreasement) in one variable leads two an increasement in the other one. If $r \approx 0$, the two variables are uncorrelated.

In general, the tracks of the center of homogeneous mass for substrates with $A = 5$ µm and 10 µm were only influenced in a direction by the substrate topography if the wavelength λ was small, i.e. the radius of maximal curvature small with $R \lesssim 5$ µm corresponding to typical length scales of a *D.d.* cell (section 4.3). On other structures with

larger R and λ, the migration resembled rather random motion without any preferential direction which is indicated by the distributions of curvotactic index CI as well as migration angle β. Consequently, there was no unique trend in the development of the equatorial radius of a prolate ellipsoid which is an indicator for the elongation of a *D.d.* cell. The two peaks in the data PDF are identified with elongated, thus motile cells and round cells being inactive.

Furthermore, there is no correlation between the cell velocity and the migration angle (Tab. 5.1) as the correlation coefficient is close to 0. Thus, we can conclude that the migration velocity is not dependent on the migration angle being consistent with the findings of Christoph Blum *et al.* in [33] for *D.d.* cell migration on the wrinkled substrates with a radius of maximal curvature ranging from $43\,\mu m - 137\,\mu m$. Unlike the experiments on wrinkles, *D.d.* cell migration is clearly influenced on cylindrical glass fibers showing a preference to migrate in the direction of highest curvature if the radius $R \lesssim 80\,\mu m$.

In Fig. 5.2b, an exemplary kymograph of the actin signal in a moving cell is shown where the intensity is summed up in z- and x-direction so that the intensity I depends only on y in µm, the direction parallel to the wave vector, and the time t in min. The associated region of interest is marked with the red box in Fig. 5.2a. After the *D.d.* cell entered the field of view around $t \approx 12\,min$, the cell showed a directed motility along the wavy structure with a zigzag pattern until $t \approx 30\,min$ indicated by the asymmetry in projected actin intensity in Fig. 5.2b. Afterwards, the cell exhibited random-like motion, as shown in Fig. 5.2a, which is why the signal is symmetrically distributed in y-direction (Fig. 5.2b). The maxima of the projected intensity to a fixed time point t are identified as the locations of actin-rich pseudopodia of the crawling *D.d.* cell. Even though *D.d.* cells revealed contact-mediated guidance in narrow channels, the spatio-temporal actin distribution in moving *D.d.* cells observed by Nagel *et al.* in [25] differs from the exemplary kymograph in Fig. 5.2b.

The results obtained from experiments with *D.d.* cells on substrates with a radius of maximal curvature $R \lesssim 5\,\mu m$ are in accordance with the work of Driscoll *et al.* [26]. Namely, *D.d.* cells crawled along nanoridges or nanogrooves whereby Driscoll *et al.* observed actin polymerization waves along the nanotopographic structures. Moreover, Song *et al.* observed T lymphocytes crawling on sinusoidal wavy surfaces in [30]. Without any treatment, the majority of the biological cells migrated along the concavely curved regions for high curvatures. This effect diminished as the curvature decreases. Even though most of the wavelengths of the structures in this work were smaller than those in [30] with $\lambda = 20\,\mu m - 160\,\mu m$, *D.d.* cells showed a similar behavior. Namely, they were also confined by sinusoidal wave structures if the radius of maximal curvature was small enough (section 4.3). To study these findings deeply, Song *et al.* treated T cells with blebbistatin and CK636 inhibiting myosinII functionality and the Arp2/3 complex,

respectively. Noteworthily, CK636 acts similarly to CK666 both binding at the interface between Arp2 and Arp3 [8]. As an actin branching molecule, the Arp2/3 complex is responsible for building up a dense actin network that is mainly located in pseudopodia (*D.d.* cells) or lamellipodia (T cells). In experiments with T cells, Song *et al.* observed that CK636 treated T cells frequently crossed the wave maxima and, therefore, revealed decreased contact guidance. Taking into account the width of a typical lamellipodium in an untreated cell, it was exposed from nearly flat to highly concave curvatures if the T cell is located around the "turning line" of the sinusoidal substrate. They presumed that the cell sensed surface curvature by the lamellipodium and that the actin polymerization was amplified in concave regions. Thus, this kept T cells staying in the concave curved grooves. We suggest a similar process in *D.d.* cells, forming pseudopodia instead of lamellipodia, to explain their behavior on sinusoidal wavy surfaces.

On a molecular level, the curvature of bent actin filaments biases the binding of Arp2/3. According to [9], the Arp2/3 complex prefers binding to convexly curved actin filaments confining the direction of branching actin filaments. This holds for the actin polymerization in pseudopodia of *D.d.* cells as suggested by Sun *et al.* in [24] where *D.d.* cells faced an asymmetric nanotopographic environment. Differently, Ramirez *et al.* Arp2/3 inhibition in fibroblasts led to more elongated cells and, consequently, higher directionality of fibroblast cell migration on fibrillar extra-cellular matrix (spacing $2\,\mu m - 10\,\mu m$, [64]). Importantly, in contrast to *D.d.* cells, fibroblasts contain stress fibers leading to a cell alignment on curved surfaces that minimizes the bending energy of these stiff bundles [31]. Apart from stress fibers, lamellipodia of fibroblasts are longer (several µm) than lamellipodia of T cells ($\approx 1\,\mu m$) and fibroblasts strongly adhere to substrates through focal adhesions [45]. *D.d.* cells do not form focal adhesions [13] and a typical length scale of a pseudopodium is $R = 1/C \sim 1/0.4\,\mu m = 2.5\,\mu m$ [10]. Thus, we do not expect a related performance of *D.d.* cells. Besides the Arp2/3 complex, the Bin-Amphiphysin-Rvs (BAR) as well as inverse BAR (IBAR) domain proteins [65] might contribute to contact guidance. Namely, BAR/IBAR proteins bind to concavely curved membrane regions and therefore affect actin polymerization into the direction pointing towards concavely curved grooves. Additionally, these proteins stabilize membrane curvature [66, 28, 27] – also in *D.d.* cells (section 2.5).

Furthermore, myosinII also plays a key role in contact guidance. On the one hand, as myosinII embedded into the actin network induces the contractile forces within a cell, it also counteracts cell-substrate adhesion and, therefore, interferes with cell motility. In the experiments with T cells performed by Song *et al.* in [30], myosinII inhibition led to an increased directionality and confined the cells to concave regions whereas untreated T cells tend to migrate temporally away from concave to low curved regions. This behavior can be explained by the fact that T cells try to increase the contact area and touch the

"side walls" in concave regions. On the other hand, myosinII affects the cell shape and cell shape reacts to cell surface curvature [18]. In consequence, it is also responsible for enhancing the directionality of cellular motion. Otherwise, in [29], Emmert *et al.* found out that cellular migration of myosinII null mutant *D.d.* cells on dog-bone shaped silica fibers is comparable to *D.d.* cell migration with complete myosinII functionality on planar surfaces suggesting that nanotopography stabilizes pseudopodia and might compensate for a decrease in cortical tension. Based on poor SNR of the myosinII-GFP signal in the experimental data in this work, it is not possible to derive information from the 3D tracks concerning the role of myosinII-mediated contractility.

To find out which of the above described myosinII-mediated effects is predominant and to prove the above-mentioned hypothesis, we have to track *D.d.* cells that are treated with blebbistatin or CK666 inhibiting the myosinII activity or the Arp2/3 complex, respectively. Moreover, it is necessary to track other reporters in *D.d.* cells that are labeled such as Arp2/3 or SadA. Their spacial distributions within the cell or at the cell membrane, respectively, gives information about the role of pseudopod formation as well as cell-substrate adhesion during *D.d.* cell migration on curved surfaces.

In possible future projects, it is desirable for spatial and temporal pattern analysis to acquire faster 3D tracks in order to increase the temporal resolution. Until now, the time interval of data acquisition is 30 s guaranteeing less bleaching since the cells are not permanently exposed to laser light. But typical time scales in the actin cortex ($\approx 2\,\mathrm{s}$, [1]) and the signal cascade (e.g. for Ras dynamics $8\,\mathrm{s} - 42\,\mathrm{s}$, [67]) are shorter. Hence, a time interval of 3D tracking $\lesssim 10\,\mathrm{s}$ leads to more detailed insight into the spatio-temporal distribution of labeled reporters. Simultaneously, the laser power has to be regulated down to prevent bleaching. Another suitable method is provided by MIET (Metal-Induced Energy Transfer). As a control experiment, it is desirable to repeat the experiments on sinusoidal surfaces with other cell types like fibroblasts that form strong adhesive bonds through focal adhesion and that contain stress fibers. At last, it is interesting to add an external stimulus to the experiments in order to probe the strength of contact guidance in comparison to other well-known stimuli like cAMP gradients (or pulses).

5.3 Single Cell Force Spectroscopy

As described in the previous section, cellular migration can be influenced by surface topography. Song *et al.* found out that the efficiency of contact guidance increases with

the strength of adhesion [30]. Similarly, Ray *et al.* identified focal adhesion as the source of contact guidance in mesenchymal-like cells as the spatial confinement due to surface topography leads to anisotropic force generation resulting in an orientational alignment of the cells and directed motility [68]. Both findings could be similar for *D.d.* cells but they lack integrins which might change their cell-substrate adhesion compared to cell-substrate adhesion of T cells.

Besides, Tarantola *et al.* pointed out the crucial role of the actin cortex for cell-substrate adhesion in *D.d.* cells (Ax3) as it decreased after treatment with latrunculin 100 fold [13]. Latrunculin inhibits the binding of monomeric actin to ATP and, therefore, disrupts the actin polymerization in total. In this work, we investigated the role of the dense cortical actin network in cell-substrate adhesion which interacts with the cell morphology and, consequently, cell membrane curvature and (cortical) tension [69]. Notably, Emmert *et al.* claimed in [29] that surface curvature stabilizes pseudopodia that get their shape, especially by the actin network. As reported by Pietuch *et al.* in [70], the cell tension decreases while a cell spreads and adheres to a substrate. Therefore, we performed SCFS with different concentrations of the Arp2/3 inhibitor CK666 to probe the effect of inhibiting the Arp2/3 complex on cell-substrate adhesion on curved surfaces. Importantly, also the myosinII-mediated contractile forces of the cell are directly related to the actin network formed by the Arp2/3 complex. If the actin filaments are monomeric, myosinII cannot induce contractility, i.e. contribute to cortical tension.

In this work, *D.d.* cells were exposed to uncoated PDMS surfaces with a convex curvature. Additionally, since *D.d.* cells were in the vegetative stage, they did not produce extracellular matrix which is why SadA and SibA could not bind to specific ligands. That is why the cell-substrate adhesion relied on van der Waals interactions of the membrane glycoproteins and the PDMS as well as on hydrophobic and electrostatic interactions [15, 71]. Ligand-receptor interactions could, consequently, be excluded. Therefore, the maximal force of adhesion F_{ad}^{max} as a measure for the total strength of adhesion sums up the van der Waals forces. The results suggested that curvature stabilizes cell-substrate adhesion. There was no significant difference between the three data sets of different inhibitor concentrations on curved surfaces whereas F_{ad}^{max} dramatically reduced for [CK666]$= 100\,\mu$M for *D.d.* cells on planar surfaces. The sample distributions for this parameter as well as for the others with exception of the lifetime τ were well represented by a log-normal distribution. Mathematically, a log-normally distributed random variable originates from a multiplicative product of several positive random variables. In the context of this work, this suggests that several mechanisms underlie the behavior of *D.d.* cells.

Taking into consideration the work of de-adhesion W_{ad}, this parameter accounts for the energy stored in the cell due to adaptation to the surface topography during cell-substrate

adhesion. According to Young's law, the adhesion energy depends linearly on cell (surface) tension whereby both the tension and bending energy determine the cell membrane shape at the underside of adherent cells [72]. Thereby, the tension is a function of Young's modulus E. In this work, the analysis of SCFS data showed that more energy is needed to detach a cell for high [CK666] if it is separated from a curved surface than from a planar one (section 4.4). This can possibly explain the behavior of F_{ad}^{max} pointing out that curvature stabilizes cell-substrate adhesion.

Considering both parameters simultaneously, we plot the work of (de-)adhesion W_{ad} as a function of the maximal force of adhesion F_{ad}^{max} for both experiments on curved and planar surfaces for each concentration of the Arp2/3 inhibitor CK666. In Fig. 5.3a, W_{ad} increases with F_{ad}^{max} which is why more energy is stored in cells if they exhibit higher F_{ad}^{max}. Remarkably, the correlation coefficient r of sample without inhibition by CK666 is higher than the others (Tab. 5.2a). In Fig. 5.3b, the behavior is different on planar surfaces. The data points of the sample with [CK666]= 5 µM do not show any clear trend whereas the other two samples of W_{ad} slightly decrease with F_{ad}^{max}.

Additionally, the higher the cellular tension and the higher F_{ad}^{max} at the same time, the more energy is stored in the cell which increases the work of de-adhesion. Inhibiting the Arp2/3 complex probably lowers the cortical tension of the cell. On planar surfaces, treatment with CK666 leads to decrease of F_{ad}^{max}. Simultaneously, Arp2/3 inhibition reduces the cortical tension leading to lower work of de-adhesion W_{ad}. The correlation coefficients around 0 (Tab. 5.2b) rejecting a correlation of both quantities for *D.d.* on planar surfaces are due to the small sample.

If cells are in contact with convexly curved surfaces, we expect a high correlation coefficient $r_c\,(F_{ad}^{max}, W_{ad})$ suggesting that more energy is stored in cells that exhibit higher F_{ad}^{max}. Furthermore, the higher W_{ad}, the larger the area of contact where a higher area of contact implicates a higher total cell surface. Notably, A. Pietuch *et al.* assumed that a deformation of the cell shape causes a restoring force due to a constant isotropic tension T. Both the overall and cortical tension T_0 as well as area dilatation of the membrane contribute to T. The overall and cortical tension T_0 comprises not only the cortical tension T_{act} related to the myosin-induced contractility of the actin cortex but also the membrane tension γ_m and the tension γ_{ad} originating in deformations of both the cortex and membrane due to adhesion sites. Thus,

$$T = T_0 + \kappa_A \frac{\Delta A}{A_0} = \gamma_m + \gamma_{ad} + T_{act} + \kappa_A \frac{\Delta A}{A_0}\,, \tag{5.1}$$

where κ_A is the area compressibility modulus, A_0 the initial and ΔA the change in surface area due to deformation of the cell shape [73]. Thus, an increase in contact area leads to higher cortical tension on curved surfaces as cell had to deform to adopt

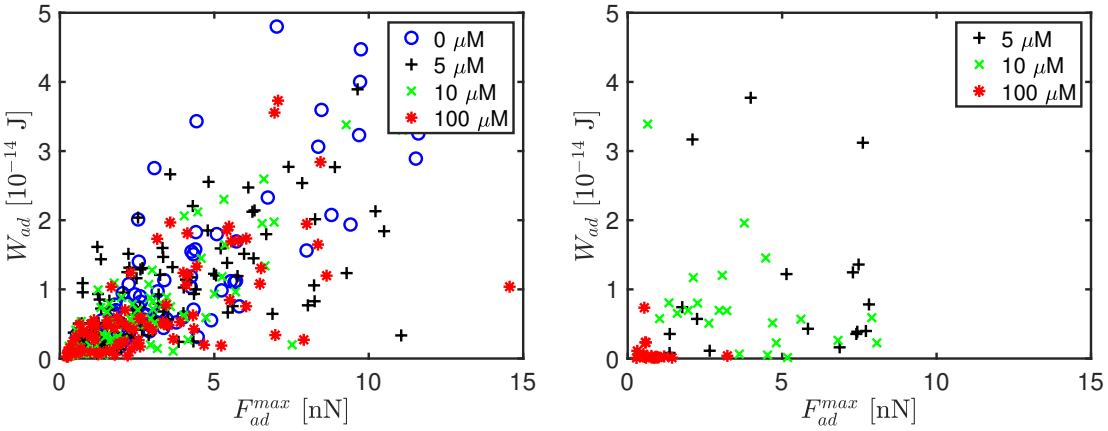

(a) Curved substrate.

(b) Planar substrate.

Figure 5.3: The work of (de-)adhesion W_{ad} as a function of the maximal force of adhesion F_{ad}^{max} for both experiments on **(a)** curved and **(b)** planar surfaces for each concentration of the Arp2/3 inhibitor CK666. The linear fits in **(a)** show entirely an increase in W_{ad} with F_{ad}^{max} whereas in **(b)** W_{ad} decays with F_{ad}^{max} for [CK666]= 10 µM and 100 µM. This indicates an increase in contact area for higher F_{ad}^{max} suggesting a decrease in cortical tension.

to the substrate topography. Adequately, the higher the concentration of CK666, the lower the cortical tension resulting in a minor correlation coefficient in Tab. 5.2a. The correlation of the data with [CK666]= 100 µM reveals a higher r compared to the data with [CK666]= 5 µM and 10 µM (Tab. 5.2a) but this could also be the consequence of some outliers that represent the data poorly.

The number of steps N_{st} represents the number of adhesion sites at the ventral side of the cell. The results in section 4.4 showed that the adhesion site dynamics were conserved in the experiments on both substrates. Since the formation of an adhesion site affects a deformation of the membrane shape as reported by Sunnick *et al.* in [74], we expect that the number of steps increases with the work of de-adhesion measuring the energy that is stored in the system of the adhered cell being confirmed in Fig. 5.4a for curved substrates. In Fig. 5.4b and Tab. 5.2b, the presumption is only correct for the sample with [CK666] = 10 µM on planar substrates. This could be owed to the low number of data points for the other concentrations of CK666 (5 µM and 100 µM). Additionally, Fig. 5.4c depicts N_{st} as a function of F_{ad}^{max} and confirms the expectation for the *D.d.* cell behavior on convex curved surfaces. We observe that F_{ad}^{max} growth with N_{st} (Tab. 5.2a) if cells are in contact with convex surfaces. This is associated with the trend in F_{ad}^{max} increasing with W_{ad} and W_{ad} correlating with N_{st}. Likewise, F_{ad}^{max} decreases with N_{st} if cells are in contact with planar surfaces for each inhibitor concentration. Possibly, this behavior

[CK666] [µM]	$r_c\,(F_{ad}^{max}, W_{ad})$	$r_c\,(W_{ad}, N_{st})$	$r_c\,(F_{ad}^{max}, N_{st})$
0	0.9166	0.5610	0.6135
5	0.6513	0.6706	0.3831
10	0.7650	0.5639	0.3685
100	0.7397	0.4928	0.3112

(a) Curved substrate

[CK666] [µM]	$r_p\,(F_{ad}^{max}, W_{ad})$	$r_p\,(W_{ad}, N_{st})$	$r_p\,(F_{ad}^{max}, N_{st})$
5	0.0063	-0.0326	-0.3201
10	-0.1536	0.1721	-0.0892
100	-0.1935	-0.1655	-0.1856

(b) Planar substrate

Table 5.2: Correlation coefficient $r(X, Y)$ between two different parameters obtained from SCFS retraction curves on both **(a)** curved and **(b)** planar surfaces. $r(X, Y)$ calculated with Maltab® function `corr2` using Pearson's definition with $-1 \leq r \leq 1$. If $r > (<)\,0$, the correlation of two variables is positive (negative) meaning that an increase (decrease) in one variable leads two an increase in the other one. If $r \approx 0$, the two variables are uncorrelated.

on planar surfaces is mediated by the competition between surface minimization due to cellular tension and maximizing the strength of adhesion. Another possible explanation is that the adhesion sites aggregate over time [74] minimizing the energy and stabilizing the system simultaneously.

This model has to be proven by analyzing the extend curve and by evaluating Young's modulus for each surface and concentration of CK666. Assuming the validity of this model, this could also explain why *D.d.* cells prefer to migrate along concave surfaces with a radius of maximal curvature that is below a typical cell size.

The h_{ls} provides information about which type of membrane proteins anchors the last membrane tether to the substrate. There might be an impact of curvature on the assembly of adhesion proteins at the membrane. Furthermore, values of $h_{ls} \gtrsim 200\,\mathrm{pN}$ indicate that the membrane tethers failed depending on membrane stiffness and membrane tension [12]. Additionally, τ reveals the same kinetics of biological bonds on curved and planar surfaces and lifetime decreases as a function of [CK666]. As both parameters rely especially on the biochemical properties of the membrane as well as the substrate, this behavior is expected since we only want to investigate mechanical stimuli due to substrate topography. Besides, the membrane and cortical tension impact the assembly of membrane proteins at the cell membrane, too. This can lead to tether rupture during retraction.

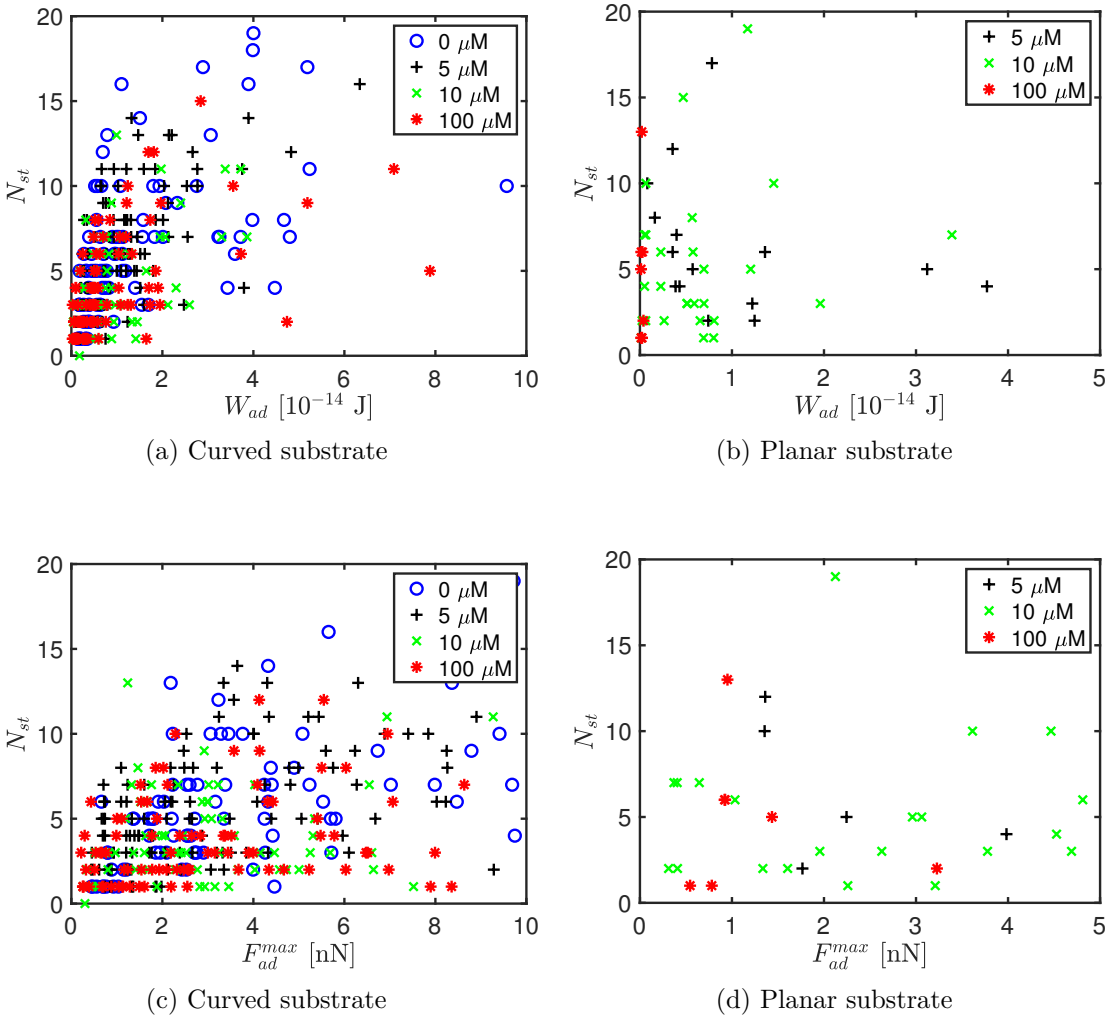

(a) Curved substrate

(b) Planar substrate

(c) Curved substrate

(d) Planar substrate

Figure 5.4: The number of steps N_{st} as a function of **(a)**, **(b)** W_{ad} and **(c)**, **(d)** for each concentration and experiments performed on planar as well as curved surfaces. In **(a)** and **(b)**, N_{st} is proportional to W_{ad} and F_{ad}^{max}. In **(d)**, N_{st} decays with F_{ad}^{max}. Altogether, the presumptions and expectations can be regarded as fulfilled.

For getting a more detailed perspective of how changes in contact area impact cell-substrate adhesion on curved surfaces, it is desirable to combine the SCFS experiments with optics, e.g. RICM or TIRFM. Both methods require well defined refractive indices so that an excitation beam can be totally reflected at the interface between the substrate and the biological cell. In this regard, Gutierrez *et al.* describe an appropriate method for substrate preparation in [75]. From optical data, we are able to calculate the contact area and to correlate this parameter, for example, with the work of de-adhesion as well as Young's modulus. It could be also reasonable to repeat the experiments on concave surfaces.

The answer to the question why curvature might stabilize cell-substrate adhesion could be given by enhanced tension of the actin cortex and the cell membrane. After Houk *et al.*, membrane tension is a long-range inhibitor of actin polymerization [69]. Since membrane tension is directly coupled to membrane curvature being confined to the substrate topography at least at the underside of the cell, we have to analyze the influence of complex geometries on the membrane and cortical tension. For approaching these parameters of a cell on sinusoidal surfaces, SCFS provides a convenient experimental mean. To calculate the tension from fits of the indentation curves, S. Sen *et al.* describe an isotropic model in [76] where a conical AFM tip indents the cell membrane.

The calculations mainly assume a rotational symmetry in geometry as well as cellular tension. At least, the experimental system in this work is not rotationally symmetric which is why another model is needed to fit the trace curve in the region of initial contact. The system can rather be modeled by a sphere being externally in contact with a cylinder. An adequate model is suggested and derived by M. J. Puttock *et al.* in [77]. They assume a smooth contact surface, linearly elastic, homogeneous as well as isotropic materials and vanishing friction whereby the deformations remain small enough so that they are still in the elastic regime of the material. Furthermore, the force exerted in the contact region is constant and the surface of the bodies are of second order, i.e.

$$ax^2 + by^2 + cz^2 + 2fyz + 2gzx + 2hxy + 2ux + 2vy + 2wz + d = 0\ . \qquad (5.2)$$

Importantly, the coordinate axes of both bodies is transformed to a single system with one common z-axis. In the following, the force is only acting in z-direction, $w_i(x, y)$ denotes the displacement of the body i at the point (x, y) parallel to z and z_i the surface of the two bodies. In the configuration of a sphere (z_1) on a cylinder (z_2), the bodies are

described by

$$z_1 = \frac{x^2}{D_1} + \frac{y^2}{D_1} \,, \tag{5.3}$$

$$z_2 = 0 + \frac{y^2}{D_2} \,, \tag{5.4}$$

where D_i are the diameters of the two bodies. Adding both equations yields

$$z_1 + z_2 = \underbrace{\frac{1}{D_1}}_{A} x^2 + \underbrace{\left(\frac{1}{D_1} + \frac{1}{D_2}\right)}_{B} y^2 \,. \tag{5.5}$$

For two bodies in contact with the total applied force P, the pressure distribution of the elliptical contact area $1 = \frac{x^2}{a^2} + \frac{y^2}{b^2}$ can be written as

$$p(x,y) = \left(\frac{3P}{2\pi ab}\right)\sqrt{1 - \frac{x^2}{a^2} - \frac{y^2}{b^2}} \,. \tag{5.6}$$

Puttock *et al.* showed that eq. (5.7) determines the expression for the compression α as well as the area of contact [77].

$$\alpha - Ax^2 - By^2 = \frac{3}{4}P(V_1 + V_2)\int_0^\infty \left(1 - \frac{x^2}{a^2+\Psi} - \frac{y^2}{b^2+\Psi}\right)\cdot \frac{\mathrm{d}\Psi}{\sqrt{\Psi(a^2+\Psi)(b^2+\Psi)}} \,, \tag{5.7}$$

where Ψ is the greatest root of

$$1 - \frac{x^2}{a^2+\Psi} - \frac{y^2}{b^2+\Psi} = 0 \,. \tag{5.8}$$

Furthermore, $V_i = (1-\nu_i^2)/(\pi E_i)$, where E_i are Young's moduli of the body i and ν_i the relates Poisson ratios. Since eq. (5.7) is valid for every point (x, y) inside the contact ellipse, the equation holds for every coefficient.

Generally, also buckling should be considered when a *D.d.* cell is pressed on a surface by the cantilever. In this regard, Knoche *et al.* [78] examined the effect of pressure exerted on soft spherical capsules and found out that the capsules buckle upon a critical pressure. This parameter is defined by

$$p_{cb} = -4\sqrt{\frac{EH_0E_B}{R_0^4}} \,, \tag{5.9}$$

where E_B is the bending modulus, H_0 the thickness of the capsule, R_0 the radius of the capsule, and E represents Young's modulus. For *D.d.* cells (Ax2), the bending modulus is $E_B \approx 390 k_B T$ [72] and the thickness of the actin cortex $H_0 \approx 200\,\text{nm}$ [1]. The Young modulus E can be estimated with the Poisson ratio $\nu \approx 0.5$ for biological materials to

$$E = \frac{12(1-\nu^2)E_B}{H_0^3} \approx 1817\,\text{Pa} \tag{5.10}$$

for a temperature of $T \approx 300\,\text{K}$. With a typical radius of $R_0 \approx 5\,\mu\text{m}$ of *D.d.* cells, the critical buckling pressure in eq. (5.9) amounts to $p_{cb} \approx 4\,\text{Pa}$. Assuming a circular contact area with a radius of $R \approx 5\,\mu\text{m}$, the critical buckling force $F_{cb} = p_{cb} \cdot \pi R^2 \approx 3 \times 10^{-10}\,\text{N} < 0.5\,\text{nN}$. As the set point during the SCFS experiments is larger than the estimated critical buckling force, the model that is used to analyze the extend curve should take buckling instabilities into account. Thus, Hertzian theory is only suited for the very initial contact before buckling in the extend curve might occur. A model that also accounts for buckling in 2D is provided by Udo Seifert in [79] and could be extended to a third dimension. Desirably, this model is not limited to the regime of initial contact.

To test the influence of substrate curvature on the overall cell tension, the analysis of the extend curve obtained by SCFS experiments provides relevant information. Combined with blebbistatin treatment, the role of myosinII could be extracted.

6 Summary

To investigate the influence of geometrically complex surface topography on *D.d.* cell migration, we produced sinusoidal wave structures using 3D printing including the design of the negatives as well as the technical printing. We applied Taubin smoothing to the designs in order to receive smooth surfaces with a root mean square roughness $\lesssim 100\,\mathrm{nm}$. As the polymerized photoresist showed high autofluorescence for the applied excitation wavelengths $\lambda_{ex} = 488\,\mathrm{nm}$ and $561\,\mathrm{nm}$, we used the 3D printed wavy surfaces as negatives for PDMS coating. Hence, we observed *D.d.* cell migration on PDMS sinusoidal surfaces (half wavelength $\lambda/2 = 16.67\,\mu\mathrm{m} - 40\,\mu\mathrm{m}$) with a sdCLSM and recorded 3D stacks over time.

The cellular migration of the social amoeba *D.d.* is quantified by the step size of the center of homogeneous mass (COHM) of *D.d.* cells, the migration angle, the curvotactic index and the equatorial radius of a prolate ellipsoid. We used the step size to threshold the data because steps of COHM due to cell shape changes are negligible. From the analysis of the PDF of step size samples, we learned that the mean step size corresponds to a typical length scale of one D.d. cell. There is only a small difference in step size and mean velocity on sinusoidal wavy surfaces compared to planar ones. Moreover, *D.d.* cells felt confined on substrates with smaller wavelengths $\lambda/2 = 16.67\,\mu\mathrm{m}$ and $20\,\mu\mathrm{m}$ whereby they exhibited a preference for concave regions. Regarding the cell shape, the PDF of equatorial radii showed two peaks that were identified to represent motile and inactive cells. Motile cells appeared elongated and were represented by the smaller equatorial radius of the prolate ellipsoid.

Addressing the influence of surface topography on *D.d.* cell migration to cell-substrate adhesion, we investigated the maximal force of adhesion, the work of de-adhesion, the lifetime of adhesion sites, the number of steps as well as the height of last step on curved surfaces by analyzing retraction curves. They were obtained by SCFS on convexly curved surfaces. We found out that surface curvature stabilizes cell-substrate adhesion. Furthermore, significantly more energy is needed to detach a cell for high [CK666] if it was separated from a curved surface than from a planar one. Importantly, these differences were not caused by different biochemical surface properties as the kinetics of adhesion sites on curved and planar surfaces did not differ significantly. Additionally, the lifetime decreased as a function of [CK666] and the adhesion site dynamics were

conserved in the experiments on both substrates.

The tension analysis in dependence on inhibitor concentration still remains open. We expect that the cortical tension provides an explanation for the differences in cell-substrate adhesion and cellular migration on distinct surface topographies.

In general, we could show that *D.d.* cell migration is confined by sinusoidal wave structures if the radii of maximal curvature are small enough. Accordingly, cell-substrate adhesion under the influence of Arp2/3 is biased by surface topography.

Appendix

Statistical Parameters of Experimental Data

Sinusoidal Wave Surface Scan

A [µm]	N_{wm}	a_1 [µm]	a_2 [1/µm]	a_3 [µm]
5	5	$5,5$	$\pi/512$	0
5	6	$5,5$	$\pi/512$	0
5	7	$5,5$	$\pi/512$	0
5	8	$5,5$	$\pi/512$	0
5	10	$5,5$	$\pi/512$	200
5	12	$5,5$	$\pi/512$	200
10	5	7	$\pi/512$	200
10	6	7	$\pi/512$	200
10	7	$5,5$	$\pi/512$	0
10	8	$5,5$	$\pi/512$	0
10	10	$5,5$	$\pi/256$	200
10	12	$5,5$	$\pi/256$	200

Table 6.1: Initial guesses for fit parameters that stem from eqs. (4.11) and (4.12).

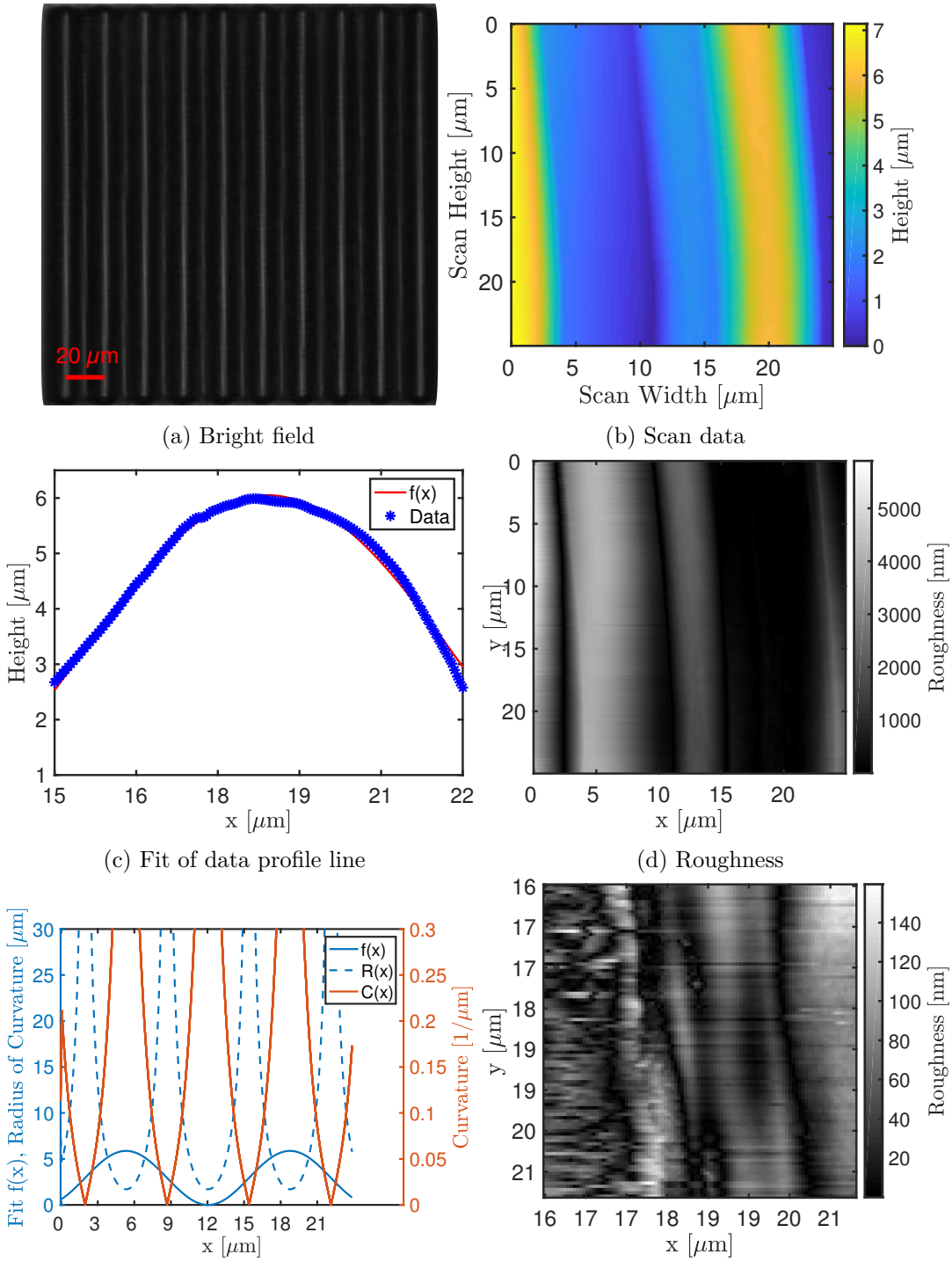

(a) Bright field (b) Scan data

(c) Fit of data profile line (d) Roughness

(e) Curvature, radius of curvature and fit (f) Roughness zoom

Figure 6.1: Scan of sinusoidal surface with Taubin smoothing ($A = 20\,\mu\text{m}$, $N_{wm} = 10$, $\lambda/2 = 20.00\,\mu\text{m}$). **(a)** Bright field image of structure. **(b)** Topography data acquired via surface scanning in contact mode with AFM. **(c)** Fit of height profile across the wave according to eq. (4.11). **(d)**, **(f)** Roughness of the structure (eq. (4.13)). **(e)** Curvature and radius of curvature (eq. (4.20) and eq. (4.21)). The radius diverges at the zeros of curvature.

R [µm]	μ [µm]	σ^2 [µm^2]	s	k
1/0	3.9010 ± 1.4479	2.0963	-8.0441	16.1178
16.18	5.2045 ± 6.8700	47.1968	-0.2292	0.1403
11.24	5.7858 ± 11.7749	138.6492	-0.0671	0.0273
8.29	6.6885 ± 5.9775	35.7310	-0.8618	0.8202
6.33	5.0893 ± 5.5737	31.0662	-0.3949	0.2898
4.05	4.6262 ± 4.0928	16.7512	-0.6955	0.6162
2.82	3.7869 ± 4.9671	24.6722	-0.1766	0.0991

(a) $\mathrm{d}r_3$

R	μ [$\frac{\mu m}{min}$]	σ^2 [$(\frac{\mu m}{min})^2$]	s	k
1/0	7.8020 ± 2.8957	8.3851	-12.9615	30.4466
16.18	10.4090 ± 13.7400	188.7874	-0.3211	0.2199
11.24	11.5715 ± 23.5499	554.5966	-0.0905	0.0406
8.29	13.3770 ± 11.9551	142.9241	-1.1097	1.1488
6.33	10.1786 ± 11.1474	124.2646	-0.5582	0.4596
4.05	9.2523 ± 8.1856	67.0048	-1.0246	1.0330
2.82	7.5738 ± 9.9342	98.6887	-0.2898	0.1918

(b) v_3

R [µm]	μ [°]	σ^2 [°^{2}]	s	k
1/0	45.1957 ± 26.6931	712.5207	-4.5388	7.5149
16.18	45.3851 ± 27.0736	732.9809	-4.4063	7.2238
11.24	44.9729 ± 27.9583	781.6686	-3.8907	6.1192
8.29	45.4751 ± 27.6382	763.8709	-4.1670	6.7054
6.33	47.2014 ± 26.9001	723.6179	-5.0664	8.7017
4.05	44.8812 ± 28.4382	808.7329	-3.6739	5.6690
2.82	50.3939 ± 27.1474	736.9814	-6.0233	10.9592

(c) β

R [µm]	μ	σ^2	s	k
1/0	0.4989 ± 0.3602	0.1297	2.6924	3.7456
16.18	0.4931 ± 0.3670	0.1347	2.6349	3.6393
11.24	0.5012 ± 0.3723	0.1386	2.4047	3.2216
8.29	0.4927 ± 0.3689	0.1361	2.6014	3.5777
6.33	0.4694 ± 0.3656	0.1337	3.0555	4.4339
4.05	0.4993 ± 0.3767	0.1419	2.3497	3.1238
2.82	0.4292 ± 0.3639	0.1325	3.8584	6.0517

(d) CI

R [µm]	μ	σ^2	s	k
1/0	0.3765 ± 0.3175	0.1008	7.5728	14.8710
16.18	0.4030 ± 0.3321	0.1103	5.8093	10.4432
11.24	0.3845 ± 0.3323	0.1104	6.3537	11.7680
8.29	0.4100 ± 0.3325	0.1106	5.5862	9.9119
6.33	0.3819 ± 0.3269	0.1069	6.7582	12.7774
4.05	0.3950 ± 0.3355	0.1126	5.8628	10.5716
2.82	0.3190 ± 0.3088	0.0954	10.7223	23.6438

(e) CI_3

R [µm]	μ [µm]	σ^2 [µm^2]	s	k
1/0	2.5942 ± 2.0930	4.3806	-0.4419	0.3366
16.18	3.8566 ± 2.5793	6.6527	-1.3585	1.5046
11.24	3.2685 ± 2.2257	4.9537	-1.0588	1.0792
8.29	3.1953 ± 2.3894	5.7090	-0.7756	0.7126
6.33	3.6879 ± 2.7712	7.6793	-0.9126	0.8851
4.05	3.5363 ± 2.1876	4.7854	-1.5586	1.8070
2.82	3.1818 ± 2.2502	5.0635	-0.9115	0.8837

(f) a

Table 6.2: Characteristics of parameter distributions obtained from **data** of 3D tracking over time on curved surfaces ($\boldsymbol{A = 5\,\mu m}$) with radius of maximal curvature 2.82 µm, 4.05 µm, 6.33 µm, 8.29 µm, 11.24 µm and 16.18 µm as well as $\infty\,\mu$m for the control measurement on a planar surface. μ represents the mean value, σ^2 the variance, s the skewness and k the kurtosis. The data are thresholded by the dynamical method described in section 4.3.1.

R [µm]	μ [µm]	σ^2 [µm^2]	s	k
1/0	3.9010 ± 1.4479	2.0963	-8.0441	16.1178
8.09	3.7954 ± 5.2050	27.0920	-0.1549	0.0832
5.62	4.0014 ± 4.8308	23.3369	-0.2398	0.1490
4.13	4.3067 ± 6.0779	36.9409	-0.1610	0.0876
3.16	3.7933 ± 3.5375	12.5138	-0.4923	0.3888
2.03	3.4308 ± 4.6853	21.9518	-0.1396	0.0725
1.41	3.3401 ± 3.9589	15.6729	-0.2065	0.1221

(a) dr_3

R [µm]	μ [$\frac{\mu m}{min}$]	σ^2 [$(\frac{\mu m}{min})^2$]	s	k
1/0	7.8020 ± 2.8957	8.3851	-12.9615	30.4466
8.09	7.5909 ± 10.4100	108.3679	-0.2538	0.1607
5.62	8.0027 ± 9.6617	93.3476	-0.3808	0.2760
4.13	8.6133 ± 12.1558	147.7637	-0.2457	0.1539
3.16	7.5866 ± 7.0750	50.0551	-0.8069	0.7512
2.03	6.8616 ± 9.3705	87.8071	-0.2448	0.1531
1.41	6.6802 ± 7.9178	62.6916	-0.3692	0.2649

(b) v_3

R [µm]	μ [°]	σ^2 [°^{2}]	s	k
1/0	45.1957 ± 26.6931	712.5207	-4.5388	7.5149
8.09	44.9201 ± 27.4100	751.3091	-4.1140	6.5920
5.62	47.6604 ± 26.7702	716.6430	-5.2953	9.2297
4.13	47.2450 ± 26.5729	706.1205	-5.2708	9.1728
3.16	48.0054 ± 26.0751	679.9116	-5.8582	10.5605
2.03	53.2916 ± 26.7231	714.1253	-7.4926	14.6615
1.41	54.7334 ± 27.8982	778.3077	-7.1451	13.7618

(c) β

R [µm]	μ	σ^2	s	k
1/0	0.4989 ± 0.3602	0.1297	2.6924	3.7456
8.09	0.5016 ± 0.3681	0.1355	2.4823	3.3610
5.62	0.4653 ± 0.3618	0.1309	3.2293	4.7732
4.13	0.4701 ± 0.3568	0.1273	3.2759	4.8653
3.16	0.4574 ± 0.3523	0.1241	3.6532	5.6263
2.03	0.3930 ± 0.3573	0.1277	4.9033	8.3300
1.41	0.3762 ± 0.3667	0.1345	4.9219	8.3724

(d) CI

R [µm]	μ	σ^2	s	k
1/0	0.3765 ± 0.3175	0.1008	7.5728	14.8710
8.09	0.3694 ± 0.3146	0.0990	8.0531	16.1418
5.62	0.3331 ± 0.3001	0.0901	10.9773	24.3964
4.13	0.3296 ± 0.2948	0.0869	11.7631	26.7524
3.16	0.3325 ± 0.3018	0.0911	10.8237	23.9425
2.03	0.2638 ± 0.2852	0.0813	17.2028	44.4086
1.41	0.2579 ± 0.2920	0.0853	16.4131	41.7113

(e) CI_3

R [µm]	μ [µm]	σ^2 [µm^2]	s	k
1/0	2.5942 ± 2.0930	4.3806	-0.4419	0.3366
8.09	2.5143 ± 2.0396	4.1599	-0.4093	0.3039
5.62	2.9867 ± 2.3615	5.5768	-0.5954	0.5009
4.13	2.4110 ± 1.9413	3.7686	-0.3840	0.2791
3.16	2.7861 ± 2.2328	4.9853	-0.5119	0.4095
2.03	3.7451 ± 2.3720	5.6262	-1.5500	1.7938
1.41	3.1105 ± 2.2625	5.1189	-0.8117	0.7572

(f) a

Table 6.3: Characteristics of parameter distributions obtained from **data** of 3D tracking over time on curved surfaces ($\boldsymbol{A = 10\,\mu m}$) with radius of maximal curvature $R = 2.82\,\mu m$, $4.05\,\mu m$, $6.33\,\mu m$, $8.29\,\mu m$, $11.24\,\mu m$ and $16.18\,\mu m$ as well as $\infty\,\mu m$ for the control measurement on a planar surface. μ represents the mean value, σ^2 the variance, s the skewness and k the kurtosis. The data are thresholded by the dynamical method described in section 4.3.1.

R [µm]	μ [µm]	σ^2 [µm^2]	s	k
1/0	3.6875 ± 1.9275	3.7154	0.6311	3.2451
16.18	7.6341 ± 3.9905	15.9242	0.6311	3.2451
11.24	11.6194 ± 6.0737	36.8899	0.6311	3.2451
8.29	7.9475 ± 4.1543	17.2584	0.6311	3.2451
6.33	6.6860 ± 3.4949	12.2145	0.6311	3.2451
4.05	5.4719 ± 2.8603	8.1814	0.6311	3.2451
2.82	5.5333 ± 2.8924	8.3659	0.6311	3.2451

(a) $\mathrm{d}r_3$

R	μ [$\frac{\text{µm}}{\text{min}}$]	σ^2 [$(\frac{\text{µm}}{\text{min}})^2$]	s	k
1/0	7.3750 ± 3.8551	14.8616	0.6311	3.2451
16.18	15.2682 ± 7.9810	63.6969	0.6311	3.2451
11.24	23.2387 ± 12.1474	147.5598	0.6311	3.2451
8.29	15.8949 ± 8.3087	69.0337	0.6311	3.2451
6.33	13.3720 ± 6.9899	48.8581	0.6311	3.2451
4.05	10.9439 ± 5.7206	32.7255	0.6311	3.2451
2.82	11.0666 ± 5.7848	33.4635	0.6311	3.2451

(b) v_3

R [µm]	μ	σ^2	s	k
1/0	0.4942 ± 0.3583	0.1284	0.0221	1.4805
16.18	0.5003 ± 0.3624	0.1313	-0.0012	1.4630
11.24	0.4972 ± 0.3674	0.1350	0.0106	1.4423
8.29	0.4931 ± 0.3682	0.1356	0.0265	1.4396
6.33	0.4777 ± 0.3567	0.1272	0.0845	1.4934
4.05	0.5075 ± 0.3751	0.1407	-0.0288	1.4121
2.82	0.4375 ± 0.3588	0.1288	0.2392	1.5298

(c) CI

R [µm]	μ	σ^2	s	k
1/0	0.3736 ± 0.3192	0.1019	0.4804	1.8694
16.18	0.3942 ± 0.3258	0.1062	0.3995	1.7713
11.24	0.3794 ± 0.3293	0.1085	0.4621	1.8048
8.29	0.3969 ± 0.3331	0.1110	0.3920	1.7317
6.33	0.3800 ± 0.3194	0.1020	0.4542	1.8455
4.05	0.3806 ± 0.3317	0.1100	0.4583	1.7906
2.82	0.3232 ± 0.3075	0.0945	0.6941	2.1643

(d) CI_3

Table 6.4: Characteristics of parameter distributions obtained from **PDF fits to the thresholded data**. The data were acquired by 3D tracking over time on curved surfaces ($\boldsymbol{A = 5\,\mu m}$) with radius of maximal curvature 2.82 µm, 4.05 µm, 6.33 µm, 8.29 µm, 11.24 µm and 16.18 µm as well as $\infty\,\mu$m for the control measurement on a planar surface. μ represents the mean value, σ^2 the variance, s the skewness and k the kurtosis.

R [µm]	μ [µm]	σ^2 [µm^2]	s	k
1/0	3.6875 ± 1.9275	3.7154	0.6311	3.2451
8.09	5.7072 ± 2.9833	8.9000	0.6311	3.2451
5.62	5.5582 ± 2.9054	8.4415	0.6311	3.2451
4.13	6.6002 ± 3.4501	11.9029	0.6311	3.2451
3.16	4.5960 ± 2.4024	5.7718	0.6311	3.2451
2.03	5.1437 ± 2.6887	7.2292	0.6311	3.2451
1.41	4.5880 ± 2.3983	5.7517	0.6311	3.2451

(a) $\mathrm{d}r_3$

R [µm]	μ [$\frac{\mu m}{min}$]	σ^2 [$(\frac{\mu m}{min})^2$]	s	k
1/0	7.3750 ± 3.8551	14.8616	0.6311	3.2451
8.09	11.4144 ± 5.9666	35.5999	0.6311	3.2451
5.62	11.1165 ± 5.8108	33.7659	0.6311	3.2451
4.13	13.2003 ± 6.9001	47.6115	0.6311	3.2451
3.16	9.1921 ± 4.8049	23.0871	0.6311	3.2451
2.03	10.2874 ± 5.3775	28.9170	0.6311	3.2451
1.41	9.1761 ± 4.7966	23.0070	0.6311	3.2451

(b) v_3

R [µm]	μ	σ^2	s	k
1/0	0.4942 ± 0.3583	0.1284	0.0221	1.4805
8.09	0.4986 ± 0.3635	0.1321	0.0053	1.4585
5.62	0.4707 ± 0.3582	0.1283	0.1114	1.4918
4.13	0.4763 ± 0.3603	0.1298	0.0900	1.4791
3.16	0.4715 ± 0.3568	0.1273	0.1080	1.4971
2.03	0.4033 ± 0.3528	0.1244	0.3737	1.6310
1.41	0.3965 ± 0.3653	0.1335	0.4057	1.5998

(c) CI

R [µm]	μ	σ^2	s	k
1/0	0.3736 ± 0.3192	0.1019	0.4804	1.8694
8.09	0.3623 ± 0.3135	0.0983	0.5243	1.9386
5.62	0.3320 ± 0.3003	0.0902	0.6470	2.1417
4.13	0.3273 ± 0.2987	0.0893	0.6670	2.1748
3.16	0.3368 ± 0.3018	0.0911	0.6264	2.1090
2.03	0.2669 ± 0.2785	0.0776	0.9502	2.7281
1.41	0.2653 ± 0.2890	0.0835	0.9747	2.7114

(d) CI_3

Table 6.5: Characteristics of parameter distributions obtained from **PDF fits to the thresholded data**. The data were acquired by 3D tracking over time on curved surfaces ($\boldsymbol{A = 10\,\mu m}$) with radius of maximal curvature R = 2.82 µm, 4.05 µm, 6.33 µm, 8.29 µm, 11.24 µm and 16.18 µm as well as $\infty\,\mu$m for the control measurement on a planar surface. μ represents the mean value, σ^2 the variance, s the skewness and k the kurtosis.

Probability density functions of the Data Samples

The SCFS data are read with the analysis software JPK SPM Data Processing provided by JPK Instruments in order to extract the above-mentioned parameters from the FDC after baseline correction. To decide whether two samples with different inhibitor concentration ([CK666]) or from two different substrates are significantly different, the same strategy as explained in section 4.3 is applied. The related mean values μ, variances σ^2, skewness s and kurtosis k are determined from the probability density functions (PDF) of the data set and shown in Tab. 6.6 for each parameter and concentration of CK666.

The above mentioned parameters are calculated with the Matlab® functions `mean()` and `var()` based on eq. (4.9) and eq. (4.10) as well as the skewness and kurtosis defined by eq. (4.7) and eq. (4.8), respectively. The statistic error of the mean value of a distribution with sample size n is assumed to be given by the standard deviation σ.

Table 6.6 shows statistical characteristics derived from the first to the forth moments of the parameter distributions of F_{ad}^{max}, W_{ad}, τ, h_{ls} and N_{st}. Those base on force-distance data that are obtained from SCFS experiments on curved surfaces. Notably, the data sets of all parameters are positive. The skewness in Tab. 6.6 is always positive for measurements on curved surfaces and it indicates an elongated tail on the right side. The standard deviation of the skewness s for normally distributed samples with $N = 94$, 118, 82 and 89 amounts to $\sigma_n^s = 0.3995$, 0.3565, 0.4277 and 0.4105. Only the lifetime τ for [CK666] = 0 µM and 5 µM in Tab. 6.6d and the number of steps N_{st} at [CK666] = 5 µM in Tab. 6.6e reveal a skewness close to 0 that might indicate a symmetric distribution, such as a normal distribution. More precisely, the absolute values of s are in the same order of magnitude as the standard deviation of skewness of a normal distribution. Furthermore, the kurtosis values are positive for each parameter and concentration. They exceed the standard deviation of the kurtosis of a normally distributed and equally sized sample ($\sigma_n^k = 1.0106$, 0.9020, 1.0820 and 1.0386) by its multiple except for τ.

On this account, we fit the data first with a log-normal distribution [80]

$$f(x) = \frac{1}{x\hat{\sigma}\sqrt{2\pi}} \exp\left(-\frac{(\ln x - \hat{\mu})^2}{2\hat{\sigma}^2}\right) , \tag{6.1}$$

that is defined for $x > 0$ with $\hat{\mu} \in \mathbb{R}$ and $\hat{\sigma} > 0$. The mean value μ, variance σ, skewness

s and kurtosis k are given by

$$\mu = \exp\left(\hat{\mu} + \frac{\hat{\sigma}^2}{2}\right) , \tag{6.2}$$

$$\sigma = \exp\left(2\hat{\mu} + \hat{\sigma}^2\right)\left(\exp\left(\hat{\sigma}^2\right) - 1\right) , \tag{6.3}$$

$$s = \left(\exp\left(\hat{\sigma}^2\right) + 2\right)\sqrt{\exp\left(\hat{\sigma}^2\right) - 1} , \tag{6.4}$$

$$k = \exp\left(4\hat{\sigma}^2\right) + 2\exp\left(3\hat{\sigma}^2\right) + 3\exp\left(2\hat{\sigma}^2\right) - 3 . \tag{6.5}$$

Notably, $s \geq 0$ and $k \geq 0$ so that the normal distribution and the PDFs of the experimental data share the above mentioned important properties. The results of the fit are presented in Tab. 6.8. For F_{ad}^{max}, the mean values of the fit and the data of each concentration show an overlap of the confidence intervals (Tab. 6.6a and Tab. 6.8a). Moreover, the values for the skewness s from both the data and the PDF fit resemble each other in absolute numbers and exceed entirely the standard deviation of the skewness of a normal distribution of corresponding sample size. Both the kurtosis and variance of the data as well as from the PDF fit show reasonable accordance in absolute values. Therefore, the log-normal distribution is assumed to represent the PDF of F_{ad}^{max} reasonably well.

Similar to F_{ad}^{max}, the mean values of W_{ad} reveal an overlap of the confidence intervals and the development of σ^2 is roughly similar for both the data and the PDF fit. Furthermore, the absolute values of s are in the same order of magnitude whereby the skewness of the fit is higher than of the data itself. The kurtosis k of the data set is much smaller than k obtained from the fit. Again, both the skewness and kurtosis are much higher than the standard deviation of the skewness of a normal distribution of corresponding sample size. Therefore, a normal distribution seems not to be suitable to describe the overall behavior of the parameter W_{ad}. Similar to the previous parameter F_{ad}^{max}, the log-normal distribution is a decent representation of the experimental data.

The mean value of the sample of the lifetime τ can only be poorly reproduced by the log-normal fit. Although the confidence intervals of both the data and the PDF fit overlap for each concentration of Arp2/3 inhibitor CK666, the variance of the data is roughly one order of magnitude smaller than the variance of the PDF fit. Furthermore, the skewness s of τ for [CK666] = 0 µM and 5 µM is close to 0 and in the same order of magnitude as the standard deviation of a normally distributed sample of equal size. The same behavior holds for the kurtosis k of the data, especially for [CK666] = 0 µM and 5 µM. In addition, related values of the PDF fit are one order of magnitude higher. Thereupon, the distribution for τ is fitted by a normal distribution. This improves the accordance of the mean values dramatically as the mean values and variance (and standard deviation) are similar. With $s = 0 \pm \sigma_n^s$ and $k = 3 \pm \sigma_n^k$ for the normal fit, a comparison to the absolute values for s and k of the data PDF reveals consistency.

A closer examination of h_{ls} yields a high overlap of the confidence intervals of μ for each concentration where σ^2 and s of the data and the log-normal fit reveal consistency. The development of k resembles for both the data and log-normal fit but for [CK666] = 100 µM. Additionally, the values for both s and k exceed the corresponding standard deviations from a normally distributed and equally sized sample. Hence, the data can be described reasonably well with a log-normal distribution.

In the case of N_{st}, the confidence intervals of the mean values for all concentrations of CK666 of both the data and the fit are in accordance. Except for s(5 µM) and k(5 µM and 10 µM), the absolute values of s and k exceed $s = 0 \pm \sigma_n^s$ and $k = 3 \pm \sigma_n^k$ of a related normal distribution. Therefore, we consider the log-normal distribution as a reasonable description for the PDF of N_{st}.

Furthermore, Tab. 6.7 shows the statistics of the data from F_{ad}^{max}, W_{ad}, τ, h_{ls} and N_{st} that are acquired on planar surfaces (Internship, Tab. 4.4b). Since the number of experiments and examined cells is low compared to those from experiments on curved surfaces, they provide an orientation. To guarantee consistency when the two experiments are compared, the data acquired on planar surfaces are fitted with the same PDF as the corresponding data acquired on curved surfaces (Tab. 6.10). In the following section, the results will be analyzed in more detail.

[CK6666]	μ [nN]	σ^2 [nN^2]	s	k
0 µM	4.7837 ± 4.4540	19.8382	1.8415	6.8432
5 µM	3.8424 ± 3.6319	13.1904	1.8429	6.6285
10 µM	4.0561 ± 6.1809	38.2029	3.9712	20.2376
100 µM	3.8279 ± 3.9114	15.2987	2.0730	7.8241

(a) F_{ad}^{max}

[CK6666]	μ [10^{-14} J]	σ^2 [$(10^{-14}\,\mathrm{J})^2$]	s	k
0 µM	1.4900 ± 1.6358	2.6758	2.0139	8.2068
5 µM	1.0177 ± 1.0170	1.0344	2.2394	9.7793
10 µM	0.8189 ± 0.8666	0.7510	1.8165	5.9334
100 µM	0.9468 ± 1.3792	1.9021	3.0545	13.3854

(b) W_{ad}

[CK666]	μ [s]	σ^2 [s^2]	s	k
0 µM	9.7278 ± 5.3403	28.5183	0.1388	1.8093
5 µM	10.1066 ± 7.0153	49.2144	0.3552	2.0831
10 µM	6.5112 ± 5.4839	30.0728	0.9297	3.3427
100 µM	7.8209 ± 5.5338	30.6227	0.8879	2.9818

(c) τ

[CK666]	μ [pN]	σ^2 [pN^2]	s	k
0 µM	148.1422 ± 78.1605	6109.0573	1.6876	6.6279
5 µM	128.9656 ± 69.1869	4786.8338	1.2392	6.0432
10 µM	101.9002 ± 51.8213	2685.4509	2.8697	16.8983
100 µM	158.0910 ± 135.6547	18402.2090	1.6525	5.1519

(d) h_{ls}

[CK666]	μ	σ^2	s	k
0 µM	6.5275 ± 4.5664	20.8520	1.2456	4.4853
5 µM	5.6281 ± 3.5288	12.4522	0.7148	2.6937
10 µM	3.9634 ± 2.7507	7.5665	1.1064	3.8180
100 µM	4.0000 ± 3.0295	9.1778	1.2924	4.2956

(e) N_{st}

Table 6.6: Characteristics of **data distributions** of F_{ad}^{max}, W_{ad}, τ, h_{ls} and N_{st} obtained from SCFS experiments on **curved** surfaces. μ represents the mean value, σ^2 the variance, s the skewness and k the kurtosis. Only $\tau(0\,\mu\mathrm{M})$, $\tau(5\,\mu\mathrm{M})$ and $N_{st}(5\,\mu\mathrm{M})$ reveal a skewness close to 0 that might indicate a symmetric distribution.

[CK6666]	μ [nN]	σ^2 [nN^2]	s	k
5 µM	5.0613 ± 2.6080	6.8016	-0.1891	0.7893
10 µM	3.2214 ± 2.2836	5.2150	0.5152	2.2828
100 µM	0.8713 ± 0.6389	0.4082	1.8710	7.1981

(a) F_{ad}^{max}

[CK6666]	μ [10^{-14} J]	σ^2 [$(10^{-14}\,\mathrm{J})^2$]	s	k
5 µM	1.0232 ± 1.0859	1.1792	0.9597	2.5039
10 µM	0.6227 ± 0.7111	0.5057	2.1839	8.5605
100 µM	0.0875 ± 0.1711	0.0293	1.8814	7.1256

(b) W_{ad}

[CK666]	μ [s]	σ^2 [s^2]	s	k
5 µM	7.8653 ± 4.1667	17.3613	0.1659	0.9224
10 µM	10.4692 ± 4.4756	20.0306	-0.0963	1.7843
100 µM	6.3650 ± 3.0740	9.4493	0.0898	0.2522

(c) τ

[CK666]	μ [pN]	σ^2 [pN^2]	s	k
5 µM	81.6294 ± 29.2471	855.3910	0.1526	1.1441
10 µM	125.6556 ± 49.7453	2474.5949	1.1443	4.3988
100 µM	71.1429 ± 30.5419	932.8095	0.0459	0.2907

(d) h_{ls}

[CK666]	μ	σ^2	s	k
5 µM	8.2353 ± 6.6005	43.5662	0.7447	1.9404
10 µM	5.2222 ± 4.3086	18.5641	1.5540	5.1506
100 µM	4.8571 ± 4.2201	17.8095	0.1995	0.5733

(e) N_{st}

Table 6.7: Characteristics of **data distributions** of F_{ad}^{max}, W_{ad}, τ, h_{ls} and N_{st} obtained from SCFS experiments on **planar** surfaces. μ represents the mean value, σ^2 the variance, s the skewness and k the kurtosis. $\tau(10\,\mu\mathrm{M})$, $\tau(100\,\mu\mathrm{M})$ and $h_{ls}(100\,\mu\mathrm{M})$ reveal a skewness close to 0 that might indicate a symmetric distribution.

[CK6666]	μ [nN]	σ^2 [nN^2]	s	k
0 µM	4.9080 ± 5.4988	30.2367	1.4197	3.7119
5 µM	3.8849 ± 4.2678	18.2142	1.7796	4.9900
10 µM	3.8845 ± 5.1473	26.4942	2.0725	6.4365
100 µM	4.1226 ± 5.8509	34.2328	2.0852	6.5557

(a) F_{ad}^{max}

[CK6666]	μ [10^{-14} J]	σ^2 [$(10^{-14}\,\mathrm{J})^2$]	s	k
0 µM	1.5134 ± 2.0858	4.3507	6.7525	135.6486
5 µM	1.0696 ± 1.3918	1.9370	6.1064	104.4147
10 µM	0.8971 ± 1.4179	2.0105	8.6905	263.1022
100 µM	0.9826 ± 1.8337	3.3625	12.0977	635.1844

(b) W_{ad}

[CK666]	μ [s]	σ^2 [s^2]	s	k
0 µM	11.2793 ± 12.2531	150.1395	4.5411	48.5745
5 µM	12.6451 ± 20.1824	407.3307	8.8540	276.3973
10 µM	8.7197 ± 18.2691	333.7599	15.4824	1235.0708
100 µM	8.6702 ± 9.8049	96.1365	4.8389	57.2202

(c) τ

[CK666]	μ [pN]	σ^2 [pN^2]	s	k
0 µM	148.1041 ± 76.4270	5841.0926	1.6855	2.4427
5 µM	130.2733 ± 78.1205	6102.8090	2.0146	4.9890
10 µM	102.0425 ± 48.7052	2372.2010	1.5406	1.4973
100 µM	157.1276 ± 140.2969	19683.2111	3.3905	22.7342

(d) h_{ls}

[CK666]	μ	σ^2	s	k
0 µM	6.8102 ± 6.2064	38.5194	3.4909	24.5487
5 µM	5.8193 ± 4.7878	22.9226	3.0251	16.7742
10 µM	4.0816 ± 3.2618	10.6395	2.9078	15.0656
100 µM	4.0520 ± 3.5548	12.6365	3.3071	21.2858

(e) N_{st}

Table 6.8: Characteristics of **log-normal fit** to data obtained from SCFS experiments on **curved** surfaces for of F_{ad}^{max}, W_{ad}, τ, h_{ls} and N_{st}. μ represents the mean value, σ^2 the variance, s the skewness and k the kurtosis. Except for F_{ad}^{max} and τ, the log-normal distribution describes the underlying PDF reasonably well.

[CK666]	μ [s]	σ^2 [s^2]	s	k
0 µM	9.7278 ± 5.3403	28.5183	0.0000	3.0000
5 µM	10.1066 ± 7.0153	49.2144	0.0000	3.0000
10 µM	6.5112 ± 5.4839	30.0728	0.0000	3.0000
100 µM	7.8209 ± 5.5338	30.6227	0.0000	3.0000

(a) τ

Table 6.9: Characteristics of PDF fit. The data PDF of τ is fitted with a **normal distribution** as s is close to 0 and $k \sim 1$ for [CK666] = 0 µM and 5 µM. μ represents the mean value, σ^2 the variance, s the skewness and k the kurtosis.

[CK6666]	μ [nN]	σ^2 [nN^2]	s	k
5 µM	5.3024 ± 0.3987	15.8932	1.0259	1.9218
10 µM	3.6786 ± 0.4740	22.4637	1.0259	1.6368
100 µM	0.8601 ± 0.0504	0.2545	1.0259	2.5226

(a) F_{ad}^{max}

[CK6666]	μ [10^{-14} J]	σ^2 [$\left(10^{-14}\,\mathrm{J}\right)^2$]	s	k
5 µM	1.1006 ± 1.6427	2.6984	7.8018	197.9875
10 µM	0.8077 ± 1.9201	3.6867	20.5635	2668.3931
100 µM	0.0725 ± 0.1353	0.0183	12.0878	633.7897

(b) W_{ad}

[CK666]	μ [s]	σ^2 [s^2]	s	k
5 µM	7.8653 ± 4.1667	17.3613	0.0000	3.0000
10 µM	10.4692 ± 4.4756	20.0306	0.0000	3.0000
100 µM	6.3650 ± 3.0740	9.4493	0.0000	3.0000

(c) τ

[CK666]	μ [pN]	σ^2 [pN^2]	s	k
5 µM	81.6294 ± 5.4081	29.2471	0.0000	3.0000
10 µM	125.6556 ± 7.0530	49.7453	0.0000	3.0000
100 µM	71.1429 ± 5.5265	30.5419	0.0000	3.0000

(d) h_{ls}

[CK666]	μ	σ^2	s	k
5 µM	8.2353 ± 6.6005	43.5662	0.7447	1.9404
10 µM	5.2222 ± 4.3086	18.5641	1.5540	5.1506
100 µM	4.8571 ± 4.2201	17.8095	0.1995	0.5733

(e) N_{st}

Table 6.10: Characteristics of **fits** to data of SCFS experiments on **planar** surfaces for F_{ad}^{max}, W_{ad}, τ, h_{ls} and N_{st}. μ represents the mean value, σ^2 the variance, s the skewness and k the kurtosis. The fits stem from the same type of distribution as from the corresponding parameter on curved surfaces due to consistency.

Bibliography

[1] T. Bretschneider, H. G. Othmer, and C. J. Weijer, "Progress and perspectives in signal transduction, actin dynamics, and movement at the cell and tissue level: lessons from dictyostelium," *Interface Focus*, vol. 6, no. 5, p. 20160047, 2016.

[2] C. A. Parent and P. N. Devreotes, "Molecular genetics of signal transduction in dictyostelium," *Annual review of biochemistry*, vol. 65, no. 1, pp. 411–440, 1996.

[3] R. L. Chisholm and R. A. Firtel, "Insights into morphogenesis from a simple developmental system," *Nature reviews Molecular cell biology*, vol. 5, no. 7, pp. 531–542, 2004.

[4] H.-F. Hsu, *Oscillatory instabilities of intracellular fiber networks.* PhD thesis, Georg-August-Universität Göttingen, 2015.

[5] T. D. Pollard, "Regulation of actin filament assembly by arp2/3 complex and formins," *Annu. Rev. Biophys. Biomol. Struct.*, vol. 36, pp. 451–477, 2007.

[6] T. D. Pollard and J. A. Cooper, "Actin, a central player in cell shape and movement," *Science*, vol. 326, no. 5957, pp. 1208–1212, 2009.

[7] T. D. Pollard and W. C. Earnshaw, "Cell biology," 2004.

[8] B. Hetrick, M. S. Han, L. A. Helgeson, and B. J. Nolen, "Small molecules ck-666 and ck-869 inhibit actin-related protein 2/3 complex by blocking an activating conformational change," *Chemistry & biology*, vol. 20, no. 5, pp. 701–712, 2013.

[9] V. I. Risca, E. B. Wang, O. Chaudhuri, J. J. Chia, P. L. Geissler, and D. A. Fletcher, "Actin filament curvature biases branching direction," *Proceedings of the National Academy of Sciences*, vol. 109, no. 8, pp. 2913–2918, 2012.

[10] C. Blum, C. Schich, M. Tarantola, and E. Bodenschatz, "Pseudopod dynamics in dictyostelium discoideum," *in preperation*, 2016.

[11] I. Hecht, M. L. Skoge, P. G. Charest, E. Ben-Jacob, R. A. Firtel, W. F. Loomis, H. Levine, and W.-J. Rappel, "Activated membrane patches guide chemotactic cell motility," *PLoS Comput Biol*, vol. 7, no. 6, p. e1002044, 2011.

[12] M. Benoit and C. Selhuber-Unkel, "Measuring cell adhesion forces: theory and principles," *Atomic Force Microscopy in Biomedical Research: Methods and Protocols*, pp. 355–377, 2011.

[13] M. Tarantola, A. Bae, D. Fuller, E. Bodenschatz, W.-J. Rappel, and W. F. Loomis, "Cell substratum adhesion during early development of dictyostelium discoideum," *PloS one*, vol. 9, no. 9, p. e106574, 2014.

[14] U. S. Schwarz and S. A. Safran, "Physics of adherent cells," *Reviews of Modern Physics*, vol. 85, no. 3, p. 1327, 2013.

[15] W. F. Loomis, D. Fuller, E. Gutierrez, A. Groisman, and W.-J. Rappel, "Innate non-specific cell substratum adhesion," *PloS one*, vol. 7, no. 8, p. e42033, 2012.

[16] P. Fey, S. Stephens, M. A. Titus, and R. L. Chisholm, "Sada, a novel adhesion receptor in dictyostelium," *The Journal of cell biology*, vol. 159, no. 6, pp. 1109–1119, 2002.

[17] C. Brunner, *Origin and Spatial Distribtion of Forces in Motile Cells*. PhD thesis, Universität Leipzig, 2011.

[18] H. Elliott, R. S. Fischer, K. A. Myers, R. A. Desai, L. Gao, C. S. Chen, R. S. Adelstein, C. M. Waterman, and G. Danuser, "Myosin ii controls cellular branching morphogenesis and migration in three dimensions by minimizing cell-surface curvature," *Nature cell biology*, vol. 17, no. 2, pp. 137–147, 2015.

[19] R. Ananthakrishnan and A. Ehrlicher, "The forces behind cell movement," *International journal of biological sciences*, vol. 3, no. 5, p. 303, 2007.

[20] R. A. Tyson, E. Zatulovskiy, R. R. Kay, and T. Bretschneider, "How blebs and pseudopods cooperate during chemotaxis," *Proceedings of the National Academy of Sciences*, vol. 111, no. 32, pp. 11703–11708, 2014.

[21] C. H. Stuelten, C. A. Parent, and D. J. Montell, "Cell motility in cancer invasion and metastasis: insights from simple model organisms," *Nature Reviews Cancer*, 2018.

[22] P. Weiss and B. Garber, "Shape and movement of mesenchyme cells as functions of the physical structure of the medium contributions to a quantitative morphology," *Proceedings of the National Academy of Sciences*, vol. 38, no. 3, pp. 264–280, 1952.

[23] G. Dunn and J. Heath, "A new hypothesis of contact guidance in tissue cells," *Experimental cell research*, vol. 101, no. 1, pp. 1–14, 1976.

[24] X. Sun, M. K. Driscoll, C. Guven, S. Das, C. A. Parent, J. T. Fourkas, and W. Losert, "Asymmetric nanotopography biases cytoskeletal dynamics and promotes unidirectional cell guidance," *Proceedings of the National Academy of Sciences*, vol. 112, no. 41, pp. 12557–12562, 2015.

[25] O. Nagel, C. Guven, M. Theves, M. Driscoll, W. Losert, and C. Beta, "Geometry-driven polarity in motile amoeboid cells," *PloS one*, vol. 9, no. 12, p. e113382, 2014.

[26] M. K. Driscoll, X. Sun, C. Guven, J. T. Fourkas, and W. Losert, "Cellular contact guidance through dynamic sensing of nanotopography," *ACS nano*, vol. 8, no. 4, pp. 3546–3555, 2014.

[27] S. Suetsugu, "The proposed functions of membrane curvatures mediated by the bar domain superfamily proteins," *The journal of biochemistry*, vol. 148, no. 1, pp. 1–12, 2010.

[28] Y. Rao and V. Haucke, "Membrane shaping by the bin/amphiphysin/rvs (bar) domain protein superfamily," *Cellular and Molecular Life Sciences*, vol. 68, no. 24, pp. 3983–3993, 2011.

[29] M. Emmert, P. Witzel, M. Rothenburger-Glaubitt, and D. Heinrich, "Nanostructured surfaces of biodegradable silica fibers enhance directed amoeboid cell migration in a microtubule-dependent process," *RSC Advances*, vol. 7, no. 10, pp. 5708–5714, 2017.

[30] K. H. Song, S. J. Park, D. S. Kim, and J. Doh, "Sinusoidal wavy surfaces for curvature-guided migration of t lymphocytes," *Biomaterials*, vol. 51, pp. 151–160, 2015.

[31] Y. Biton and S. Safran, "The cellular response to curvature-induced stress," *Physical biology*, vol. 6, no. 4, p. 046010, 2009.

[32] J. A. Sanz-Herrera, P. Moreo, J. M. García-Aznar, and M. Doblaré, "On the effect of substrate curvature on cell mechanics," *Biomaterials*, vol. 30, no. 34, pp. 6674–6686, 2009.

[33] C. Blum, *Curvotaxis and Pattern Formation in the Actin Cortex of Motile Cells*. PhD thesis, Georg-August-Universität Göttingen, 2015.

[34] P. Fey, A. S. Kowal, P. Gaudet, K. E. Pilcher, and R. L. Chisholm, "Protocols for growth and development of dictyostelium discoideum," *Nature protocols*, vol. 2, no. 6, pp. 1307–1316, 2007.

[35] M. Fischer, I. Haase, E. Simmeth, G. Gerisch, and A. Müller-Taubenberger, "A brilliant monomeric red fluorescent protein to visualize cytoskeleton dynamics in dictyostelium," *FEBS letters*, vol. 577, no. 1-2, pp. 227–232, 2004.

[36] P. J. van Haastert, I. Keizer-Gunnink, and A. Kortholt, "Essential role of pi3-kinase and phospholipase a2 in dictyostelium discoideum chemotaxis," *J Cell Biol*, vol. 177, no. 5, pp. 809–816, 2007.

[37] A. J. Davidson, C. Amato, P. A. Thomason, and R. H. Insall, "Wasp family proteins and formins compete in pseudopod-and bleb-based migration," *J Cell Biol*, vol. 217, no. 2, pp. 701–714, 2018.

[38] Asylum Research Oxford Instruments company, 6310 Hollister Ave, Santa Barbara, CA 93117, *Installation and Operation Manual*, April 2008.

[39] H.-J. Butt and M. Jaschke, "Calculation of thermal noise in atomic force microscopy," *Nanotechnology*, vol. 6, no. 1, p. 1, 1995.

[40] B. Cappella and G. Dietler, "Force-distance curves by atomic force microscopy," *Surface science reports*, vol. 34, no. 1-3, pp. 1–104, 1999.

[41] "Bruker afm probes mlct." modified from `https://www.brukerafmprobes.com/p-3444-mlct.aspx`. Accessed: 2018-03-19,.

[42] "Spinning disk confocal - a technical overview." `http://www.andor.com/learning-academy/spinning-disk-confocal-a-technical-overview`. Accessed: 2018-03-19.

[43] R. Gräf, J. Rietdorf, and T. Zimmermann, "Live cell spinning disk microscopy," in *Microscopy techniques*, pp. 57–75, Springer, 2005.

[44] A. Nakano, "Spinning-disk confocal microscopy—a cutting-edge tool for imaging of membrane traffic," *Cell structure and function*, vol. 27, no. 5, pp. 349–355, 2002.

[45] K. H. Song, J. Lee, H.-R. Jung, H. Park, and J. Doh, "Turning behaviors of t cells climbing up ramp-like structures are regulated by myosin light chain kinase activity and lamellipodia formation," *Scientific reports*, vol. 7, no. 1, p. 11533, 2017.

[46] P. Cignoni, M. Callieri, M. Corsini, M. Dellepiane, F. Ganovelli, and G. Ranzuglia, "MeshLab: an Open-Source Mesh Processing Tool," in *Eurographics Italian Chapter Conference* (V. Scarano, R. D. Chiara, and U. Erra, eds.), The Eurographics Association, 2008.

[47] Nanoscribe GmbH, Hermann-von-Helmholtz-Platz 1, 76344 Eggenstein-Leopoldshafen, Germany, *Photonic Professional (GT) - User Manual*, July 2015.

[48] A. Ostendorf and B. N. Chichkov, "Two-photon polymerization: a new approach to micromachining," *Photonics Spectra*, vol. 40, no. 10, p. 72, 2006.

[49] B. H. Cumpston, S. P. Ananthavel, S. Barlow, D. L. Dyer, *et al.*, "Two-photon polymerization initiators for three-dimensional optical data storage and microfabrication," *Nature*, vol. 398, no. 6722, p. 51, 1999.

[50] C. B. Lang and N. Pucker, *Mathematische Methoden in der Physik*, vol. 2. Springer, 2005.

[51] W. Press, B. Flannery, S. Teukolsky, and W. Vetterling, "Moments of a distribution: Mean, variance, skewness, and so forth," *Numerical Recipes*, pp. 604–609, 1992.

[52] D. Nečas and P. Klapetek, "Gwyddion: an open-source software for SPM data analysis," *Central European Journal of Physics*, vol. 10, pp. 181–188, 2012.

[53] G. Taubin, "A signal processing approach to fair surface design," in *Proceedings of the 22nd annual conference on Computer graphics and interactive techniques*, pp. 351–358, ACM, 1995.

[54] G. Taubin, "Curve and surface smoothing without shrinkage," in *Computer Vision, 1995. Proceedings., Fifth International Conference on*, pp. 852–857, IEEE, 1995.

[55] M. Desbrun, M. Meyer, P. Schröder, and A. H. Barr, "Implicit fairing of irregular meshes using diffusion and curvature flow," in *Proceedings of the 26th annual conference on Computer graphics and interactive techniques*, pp. 317–324, ACM Press/Addison-Wesley Publishing Co., 1999.

[56] T. F. Coleman and Y. Li, "An interior trust region approach for nonlinear minimization subject to bounds," *SIAM Journal on optimization*, vol. 6, no. 2, pp. 418–445, 1996.

[57] T. S. Newman and H. Yi, "A survey of the marching cubes algorithm," *Computers & Graphics*, vol. 30, no. 5, pp. 854–879, 2006.

[58] J. D. Gibbons and S. Chakraborti, "Nonparametric statistical inference," in *International encyclopedia of statistical science*, pp. 977–979, Springer, 2011.

[59] M. Siddiqui, "Some problems connected with rayleigh distributions," *Journal of Research of the National Bureau of Standards*, vol. 66, no. 2, pp. 167–174, 1962.

[60] "Rayleigh distribution." `http://mathworld.wolfram.com/RayleighDistribution.html`. Accessed: 2018-05-28.

[61] A. W. Bowman and A. Azzalini, *Applied smoothing techniques for data analysis: the kernel approach with S-Plus illustrations*, vol. 18. OUP Oxford, 1997.

[62] N. Johnson, S. Kotz, and N. Balakrishnan, "Chapter 21: Beta distributions, vol. 2," 1995.

[63] "Rayleigh distribution." `http://mathworld.wolfram.com/BetaDistribution.html`. Accessed: 2018-05-28.

[64] G. Ramirez-San Juan, P. Oakes, and M. Gardel, "Contact guidance requires spatial control of leading-edge protrusion," *Molecular biology of the cell*, vol. 28, no. 8, pp. 1043–1053, 2017.

[65] J. Linkner, G. Witte, H. Zhao, A. Junemann, B. Nordholz, P. Runge-Wollmann, P. Lappalainen, and J. Faix, "The inverse bar domain protein ibara drives membrane remodeling to control osmoregulation, phagocytosis and cytokinesis," *J Cell Sci*, vol. 127, no. 6, pp. 1279–1292, 2014.

[66] H. T. McMahon and J. L. Gallop, "Membrane curvature and mechanisms of dynamic cell membrane remodelling," *Nature*, vol. 438, no. 7068, p. 590, 2005.

[67] P. J. van Haastert, I. Keizer-Gunnink, and A. Kortholt, "Coupled excitable ras and f-actin activation mediate spontaneous pseudopod formation and directed cell movement," *Molecular Biology of the Cell*, pp. mbc–E16, 2017.

[68] A. Ray, O. Lee, Z. Win, R. M. Edwards, P. W. Alford, D.-H. Kim, and P. P. Provenzano, "Anisotropic forces from spatially constrained focal adhesions mediate contact guidance directed cell migration," *Nature Communications*, vol. 8, 2017.

[69] A. R. Houk, A. Jilkine, C. O. Mejean, R. Boltyanskiy, E. R. Dufresne, S. B. Angenent, S. J. Altschuler, L. F. Wu, and O. D. Weiner, "Membrane tension maintains cell polarity by confining signals to the leading edge during neutrophil migration," *Cell*, vol. 148, no. 1-2, pp. 175–188, 2012.

[70] A. Pietuch and A. Janshoff, "Mechanics of spreading cells probed by atomic force microscopy," *Open biology*, vol. 3, no. 7, p. 130084, 2013.

[71] N. Kamprad, F. Savic, C. Kreis, O. Bäumichen, B. Geil, A. Janshoff, and M. Tarantola, "Adhesion of dictyostelium discoideum under the influence of van der waals forces," *Biophysical Journal (in preperation)*, 2018.

[72] R. Simson, E. Wallraff, J. Faix, J. Niewöhner, G. Gerisch, and E. Sackmann, "Membrane bending modulus and adhesion energy of wild-type and mutant cells of dictyostelium lacking talin or cortexillins," *Biophysical journal*, vol. 74, no. 1, pp. 514–522, 1998.

[73] A. Pietuch, B. R. Brückner, T. Fine, I. Mey, and A. Janshoff, "Elastic properties of cells in the context of confluent cell monolayers: impact of tension and surface area regulation," *Soft Matter*, vol. 9, no. 48, pp. 11490–11502, 2013.

[74] E. Sunnick, A. Janshoff, and B. Geil, "Energetics of adhesion cluster formation in the context of biological membranes," *Physical Review E*, vol. 86, no. 5, p. 051913, 2012.

[75] E. Gutierrez, E. Tkachenko, A. Besser, P. Sundd, K. Ley, G. Danuser, M. H. Ginsberg, and A. Groisman, "High refractive index silicone gels for simultaneous total internal reflection fluorescence and traction force microscopy of adherent cells," *PLoS One*, vol. 6, no. 9, p. e23807, 2011.

[76] S. Sen, S. Subramanian, and D. E. Discher, "Indentation and adhesive probing of a cell membrane with afm: theoretical model and experiments," *Biophysical journal*, vol. 89, no. 5, pp. 3203–3213, 2005.

[77] M. Puttock and E. Thwaite, *Elastic compression of spheres and cylinders at point and line contact*. Commonwealth Scientific and Industrial Research Organization Melbourne, Australia, 1969.

[78] S. Knoche and J. Kierfeld, "Buckling of spherical capsules," *Physical Review E*, vol. 84, no. 4, p. 046608, 2011.

[79] U. Seifert, "Adhesion of vesicles in two dimensions," *Physical Review A*, vol. 43, no. 12, p. 6803, 1991.

[80] A. Mood, F. Graybill, and D. Boes, "Introduction to the theory of statistics. 3rd mcgraw-hill," 1974.

Acknowledgements

At the end of my Master thesis, I would like to thank several people who supported me during this period. First, I want to thank Prof. Dr. Dr. hc. Eberhard Bodenschatz and Dr. Marco Tarantola for giving me the possibility to write my Master thesis in the Laboratory for Fluid Physics, Pattern Formation and Biocomplexity at the Max Planck Institute for Dynamics and Self-Organization, and Prof. Dr. Stefan Klumpp from the Institute for Nonlinear Dynamics, University of Göttingen for being the second advisor of my Master thesis. Especially, I want to thank Dr. Marco Tarantola for the opportunity to perform a very interesting project in biophysics related research and for his advice. He strongly supported me in handling *D.d.* cells and introduced me to optical microscopy as well as atomic force microscopy. Thanks to him, I deepened my knowledge in a lot of different fields of biophysics, such as pattern formation within the cell, cell mechanics, and cell-substrate adhesion. Furthermore, I greatly appreciate that he confided in me to plan autonomously an interdisciplinary project that gave me various perspectives on research in biophysics and for the enriching discussions about the projects we had during my Master thesis. I am also thankful for the student assistant job that was financially supported by the DFG SFB 937 - "Collective behavior of soft and biological matter" (A8 and A11) and for the opportunity to participate at the International Dictyostelium Conference 2017 in Geneva. At the conference, I especially received numerous impressions regarding other fields of research related to *D.d.* cells. I appreciate Dr. Marco Tarantola not only as a skilled scientist but also as an excellent advisor.

Moreover, I want to thank Maren Stella Müller, Sarah Romanowski and Katharina Schneider who always prepared the *D.d.* cells for my experiments. Without their great job, it would not have been possible to acquire such good data both with the sdCLSM and AFM. Furthermore, I want to thank Francesca Cavallini, Jule Marie Johannsen , Nadine Kamprad and Florian Spreckelsen for proofreading my Master thesis. Francesca Cavallini was my office mate for eight months and discussed appropriate methods for analyzing the experimental data with me. Nadine Kamprad additionally introduced me to several setups and always gave me helpful advice regards to *D.d.* cells. I am also thankful for Johannes Güttler's initial help with the 3D printer in the clean room and thank Antonio Ibanez who showed me how to use the 3D laser scanning microscope for testifying the quality of the 3D prints. During the Master thesis, I also benefited

greatly from suggestions by Dr. Isabella Guido, Dr. Azam Gholami, Dr. Laura Turco, Dr. Christian Westendorf and Albert Bae.

Furthermore, I want to the thank the entire Laboratory for Fluid Dynamics, Pattern Formation and Biocomplexity as it was a very nice and friendly environment to graduate. I want to thank the whole staff, including Andreas Kopp, Artur Kubitzek, Angela Meister, Gerhard Nolte, Andreas Renner and Olaf Trümper.

I also want to thank Prof. Dr. Andreas Janshoff from the Biophysical Chemistry of the Georg August University of Göttingen for his generosity. They provide the Cellhesion 200 in the laboratories for the SCFS.

Additionally, I want to thank the "Konrad-Adenauer-Stiftung" not only for their financial support during my studies but also for all the enriching seminars and the non-material support I received during all the diverse and interdisciplinary events and discussions with other scholars and tutors.

Finally, I would like to thank my family and my friends for supporting me not only during the period of my Master Thesis but for the entity of my studies.

Erklärung Ich versichere hiermit, dass ich die vorliegende Arbeit ohne fremde Hilfe selbstständig verfasst und nur die von mir angegebenen Quellen und Hilfsmittel verwendet habe. Wörtlich oder sinngemäß aus anderen Werken entnommene Stellen habe ich unter Angabe der Quellen kenntlich gemacht. Die Richtlinien zur Sicherung der guten wissenschaftlichen Praxis an der Universität Göttingen wurden von mir beachtet. Eine gegebenenfalls eingereichte digitale Version stimmt mit der schriftlichen Fassung überein. Mir ist bewusst, dass bei Verstoß gegen diese Grundsätze die Prüfung mit nicht bestanden bewertet wird.

Göttingen, 22. Juni 2018

(Marcel Schröder)